The Influence of Aeration and Deadrise Angle on Impact

An experimental and numerical study of the influence of deadrise angle and aeration on maximum impact pressure.

TU Delft

T. van der Zee

The Influence of Aeration and Deadrise Angle on Impact

An experimental and numerical study of the influence of deadrise angle and aeration on maximum impact pressure.

by

T. van der Zee

to obtain the degree of Msc in Marine Technology in the specialisation of Hydrodynamics

at the Delft University of Technology.

to be defended publicly on Friday April 8, 2022 at 15:00.

Student number:	4356853	
Project duration:	March, 2021 – April, 2022	
Thesis number:	MT.21/22.024.M.	
Thesis committee:	Dr. Ir. P.R. Wellens,	TU Delft, supervisor
	Ir. M. van der Eijk,	TU Delft
	Dr. Ir. M.B. Duinkerken,	TU Delft

Cover image: Royal Navy Type 42 destroyer HMS Nottingham (D91) buries her bow. [34]

TU Delft

Abstract

When sailing in heavy seas, it happens that the water washes over the bow. This shipping of water is generally divided into two types. The term white water is used when the water is more of a spray and is generally harmless. Green water is more violent and can pose a danger to the crew and structures on board.

Research on green water has mainly focused on the arrival of green water on deck and the different types. Impacts are generally considered as result of green water wave and tested by a dam-break problem. The impact of green water has not been studied as solely the impact of water on a structure. Drop test experiments are conducted in different ways for different shapes in the past. However, there have not been tests before with green water using drop tests. Drop tests are deemed suitable to test shapes with different deadrise angles and create aerated water.

The aim of this work is to investigate the effects of green water on deck structures by studying the maximum impact pressure when considering the deadrise angle and the aeration.

In this thesis the influence of shape and aeration on the maximum pressure at impact is investigated. To investigate the effect of aeration and shape, the impact tests are conducted using a drop tower experiment. For this experiment different increasing deadrise angles are chosen from 0° or a flat plate up to 30°. In addition test with aerated water are done up to 4% which is in range of real green water waves. The aeration and the shapes are chosen in such a way that non-compressible, linear compressible and non-linear compressible effects take place. It can be seen that with a flat plate, the impact increases almost instantaneously and produces a high peak. Adding aeration reduces this peak considerably. From examining the impact of the wedges, it can be concluded that the pressure rises more slowly at a higher deadrise angle. The almost instantaneous drop in pressure seen with a flat plate changes to a smoother rise at a high deadrise angle.

In addition to the experiment, numerical simulations are carried out to verify the solution. The numerical simulations also give a better insight into the pressure across the width of the object. Upon examining the numerical simulations, it is concluded that the results for deadrise angles of 15° and 30° are equivalent to the results of the results of the experiment. However, the simulations for a flat plate result in an high pressure which is probably due to a low number of data points which capture the peak.

It can be concluded that the shape of the structure and aeration have a significant influence on the maximum pressure. However, the decrease due to a higher deadrise angle is more significant than the effect of additional aeration. With higher aeration, the maximum pressures are closer together and the difference in deadrise angle has less effect. When examining the impact pressures the effect of both deadrise angle and aeration can be seen. The maximum impact for a non aerated flat plate impact measured is 9.93$[bar]$ and is decreased by 8.8$[bar]$ for a wedge impact with a deadrise angle of 30° which drops in water that is 4% aerated. The influence of both shape and aeration can be reviewed independently which leads to an reduction of impact pressure for a flat plate of 59 percent when 4% air is added to the system. When only changing the deadrise angle to 30° a reduction of 86% is found.

Preface

When my parents asked me what I wanted to do with my life after high-school the answer was clear. Coming from a maritime family, I wanted to nothing to do with boats.

Now nearly ten years later I am on the verge of becoming an engineer specialised in hydrodynamics.

This thesis will take you through the process of creating, building conducting and reviewing an experiment and numerical simulations. Which all try to estimate the maximum impact pressure of a green water wave and determine the influence of deadrise angle and aeration.

Of course I could not have done this without a great deal of help from a lot of people. First of all, I would like to thank Peter Wellens who, despite having a very busy schedule, was willing to be my supervisor. Conduction an experiment was a educational and exiting new process for me. Which I had never done before on this scale. Thank you for the opportunity. Furthermore, I would like to thank Martin van der Eijk. Thank you Martin for always asking the questions I had just not thought of and keeping me on my toes. Additionally, I would like to thank Jasper den Ouden, Peter Poot, Pascal Chabot, Andre van den Bosch and Sebastian Schreier for all their help with the experiment and supporting equipment. Furthermore I would like to thank my independent committee member Mark Duinkerken.

I finally would like to thank my family, girlfriend, friends, former and current housemates and board members for all their support during this thesis and before.

T. van der Zee
Delft, April 3, 2022

Contents

List of Figures

List of Tables

Glossary

2D Two Dimensional. 1, 2, 5, 6, 8, 9, 13, 14, 48, 69, 77

3D Three Dimensional. 2, 5, 6, 9, 13, 22, 48, 74

CFD Computational Fluid Dynamics. 1

CFL Courant-Friedrichs-Lewy. 48

DAQ Data Acquisition. xiv, 21, 25, 26, 32, 33, 81

DB Dam-Break. 1, 2, 6–8, 10, 11, 69

FPSO Floating Production Storage and Offloading. 1, 6

GW Green Water. 1–3, 5–11, 13, 17, 21, 48, 69, 70

HF Hammer Fist. 1, 2, 6, 69

LGB Light Gate Bottom. 32, 36

LGT Light Gate Top. 32, 36

LNG Liquefied Natural Gas. 5

M Mach number. 10, 11

PDB Plunging Dam-Break. 1, 2, 6, 11, 69

PRF Pressure Reduction Factor. 17

SPH Smooth Particle Hydrodynamics. 2, 5

WW White Water. 1, 2

Nomenclature

α	Deadrise angle	$[deg]$
β	Volume fraction	$[-]$
ϵ	Maximum pass band gain	$[dB]$
ω	Frequency	$[Hz]$
ω_c	Cut-off frequency	$[Hz]$
ρ	Density	$[kg/m^3]$
c	Speed of sound	$[m/s]$
E_{kin}	Kinetic energy	$[J]$
F	Force	$[N]$
g	Gravitational constant	$9.81[m/s^2]$
h_0	Initial wave height	$[m]$
h_{drop}	Drop height	$[m]$
K_s	Bulkmodulus stiffness	$[Gpa]$
m	Mass	$[kg]$
n	Order	$[-]$
s	Distance	$[m]$
v	Velocity	$[m/s]$
v_e	Edge velocity	$[m/s]$
v_i	Impact velocity	$[m/s]$
W	Work	$[J]$

1 Introduction

When sailing in heavy seas, there is a possibility of water reaching the deck via the bulwark. Shipping of water is split up by the less dangerous White Water (WW), which is used for spray, and Green Water (GW), which is a more violent impact. Green Water can have an impact on the deck itself and the structures on deck and pose a safety risk to crew and equipment. Due to the unpredictability and complexity of green water on deck, much research has been done on the problem of green water. Buchner is one of the first to have studied green water in depth, examining the entire problem of green water on Floating Production Storage and Offloading (FPSO) units [4, 5]. GW is a problem for a wide range of vessels and can occur under a variety of conditions.

This chapter identifies the current state of knowledge about GW by explaining the research that has been carried out to date. This results in a knowledge gap, which is discussed in section 1.2. This gap forms the basis for the problem and the structure of the thesis.

1.1 Overview of green water research

In order to establish the current development in Green Water research, the current state of knowledge should be determined. By examining the most important research in relation to. GW, a good basis for research can be found. At the end of this section, the knowledge gap can be identified.

The research conducted by Buchner eventually led to a comprehensive work on the problem of green water [6]. The work examines the various aspects of Green Water research, including: the arrival of green water, the flow on deck and the effects on deck and structures. In this work, Buchner states that the arrival of a wave on deck is well represented by a Dam-Break (DB) problem. However, not all waves arriving on deck can be estimated in the same way, as Greco [14, 15] shows. Greco has studied the different types of GW waves and distinguished them. According to Greco's work, a distinction is made between a Dam-Break (DB) event, a plunging wave, a Plunging Dam-Break (PDB) event and a Hammer Fist (HF) event. Numerical simulations and 2D experiments on a floating body are used to find the conditions for the generation of a typical event. It is found that PDB and HF events occur at a high wave steepness with a high and low vertical velocity, respectively. At a lower slope, the green water wave generally consists of a DB event. The simplification of green water to a DB problem is enforced by Pham [31]. Pham used CFD on a high-speed container ship and concluded that the DB assumption is valid when an initial speed is considered.

Due to the complexity and volume of research on GW, most studies focus on one element of the problem. It can be noted that research on Green Water (GW) is focused on one of three parts: the arrival on deck and type of the wave, the flow on deck and the influence of the bow shape, and the effects of a wave on the deck and/or structures on deck.

Greco [14, 15] wave types are studied in depth for a better understanding of the different types of waves. In 2017, Hernandes-Fontes began DB experiments to simulate green water [17, 18, 20]. While Greco tried to

identify the different types of Green Water (GW) events and qualify them by steepness and velocity, Hernandes-Fontes continued this by generating singular events of the different GW waves.

Hernandes-Fontes [20] used 2D experiments with a barge to create single green water waves of the types Dam-Break (DB), Plunging Dam-Break (PDB) and Hammer Fist (HF). This is combined with the properties of the waves after they arrive on deck. The type of impact can be determined from the wave properties. If the type of impact is known, the velocities on deck can be determined. The shape and nature of the cavity when a PDB or HF green water occurs can also be determined. This work is a continuation of the work of Hernandes-Fontes [13], which aims to determine the development of green water in a particular type of impact, as well as the freeboard excess and the resulting volume on deck. It is shown that a HF type of impact exceeds the freeboard the most. A PDB event will result in the greatest volume of water on deck. An DB event will cause a more horizontal impact, while an HF event will cause a more vertical impact. A PDB event creates both a horizontal and a vertical impact.

The impacts discussed by Hernandes-Fontes and Greco [13–15, 17, 18, 20] all focus on unbroken waves. However, in an earlier experiment, Hernandez-Fontes [19] found that a broken wave has a different impact on the deck. In particular, a broken flow has a violent, aerated influence on the deck.

In all experiments, however, Hernandes-Fontes [13, 17–20] used only a floating or fixed barge with a vertical bow. This is done to create the most 2D wave possible and tries to eliminate unpredictable and unstable 3D effects. The advantage of a 2D approach is that it can be easily compared to a 2D numerical estimate. Moreover, Hernandez has used an DB problem to generate a wave that simulates an Green Water (GW) wave on deck. This gives an insight into the different types of green water, but neglects scale effects or can extract the only green water wave on deck.

This study shows that the steepness and velocity of the wave are decisive for the type of green water. However, the dimensions of the ship and especially the shape of the bow also have an influence on the occurrence of green water.

In the work of Buchner [6] the possibility of using numerical simulations is briefly mentioned. More recent work has attempted to solve the green water problem using Smooth Particle Hydrodynamics (SPH). [1, 3, 22, 26]. Kawamura [22] uses the SPH Method to determine the green water on a fishing vessel. Due to the low freeboard on a fishing vessel, the green water on the whole vessel is studied and compared with other experiments. Bašić finds a solution for violent fluid-structure interactions including free surface fragmentation [3]. Mintu [26] shows that a SPH method can also work for heavily disturbed free surfaces due to ship-wave interactions and even WW.

1.2 Knowledge Gap

When GW occurs as DB, PDB or HF type of impact occurs, a mass of water flows over the deck. This flow will inevitably interact with the structures on deck. The highest impact is expected at the first contact with the wave front and the structure. This impact can cause damage to the structures if the impact is significant.

To improve the current knowledge of GW, a better estimation of the impact on vertical structures is needed. The magnitude of the impact is strongly influenced by the angle between the wave front and the structure. The term deadrise angle is used in this thesis to refer to this angle. There is no clear research on the effects of a GW wave travelling at an angle.

Besides the angle of incidence, a second important factor for GW is the presence of air in the water. It is expected that GW will arrive on board already aerated. GW occurs when the wave height is higher than the freeboard of a vessel. This is generally the case in rougher seas. In rough seas, wave-wave interactions and breaking waves lead to entrapment of air. It can be assumed that the water arriving on deck is aerated. Research does not consider the effect of aerated water, while seawater can be aerated up to 3%.

The combination between the deadrise angle and the degree of aeration on the effect on impact has not yet been studied. A systematic study of impact under the influence of deadrise angle and ventilation may lead to better design conditions for safe foredecks on ships or to optimised deck structures.

1.2.1. Relevance

GW may result in impact with structures on deck. Two types of problems can occur: When waves hit a structure repeatedly, damage can occur due to fatigue of the structure. The opposite of fatigue is an impact that directly damages the structure. Such an impact exceeds the maximum tensile strength of the structure. A better understanding of the maximum impact pressure will help to better manage these types of damage to marine structures.

Ultimately, this may lead to more targeted strengthening of ship structures as high impact loads are expected. On the other hand, this can also lead to places that are less reinforced. If weight can be saved through optimised design, fuel can also be saved. The ship also becomes safer because it is less susceptible to damage.

Research into the effects of air aerated impact on structures can also be applied to other areas. For example, the effects on the foundations of wind turbines or on coastal protection structures such as quays.

1.3 Problem Definition

Increasing the deadrise angle and aeration can be expected to influence the impact. However, the magnitude of the impact needs to be put into perspective. Combining the effects of aeration and deadrise angle may lead to a better understanding of the effects on deck structures. Since an experiment and numerical simulation are preferred to study the effects, similar experiments in the literature should also be considered. More research should be done on general GW impact and on impacts in general. This theoretical background forms the basis for the experiment and simulation.

With the knowledge of impact and green water in general, an experiment with different deadrise angles and ventilation levels will provide insights into the magnitude of the impact pressure. The experiment needs to be redesigned and set up. The experiment is more a means to deliver results. A well-designed and constructed experiment will help provide meaningful results.

To complete the results, numerical simulation is helpful. It is expected that by conducting numerical simulations, gaps in the experiment can be filled. By combining experiments and simulations, a better understanding of the impact pressure should be achieved.

All these steps can be translated into objectives leading to the goal of this thesis. The goal of this work is described below:

> Investigate the effects of green water on deck structures by studying the maximum impact pressure, taking into account the deadrise angle and the aeration of the impact.

The following objectives have been set:

- The properties of a GW wave should be studied and if they are not variable for research, they should be estimated.
- A choice should be what type of experiment should be conducted.
- Drop impacts should be examined to achieve a first estimation of the GW impact.
- Construct an experiment which recreates the GW impact as close as possible.
- Conduct experiments with systematically changing deadrise angles and levels of aeration.
- Conduct numerical simulations which are comparable with the experiment
- Compare the experiments and simulations in such a way that an estimation can be made about the maximum impact pressure

- Provide results of the maximum pressure for impacts for different angles and levels of aeration.

The structure of this thesis follows the objectives broadly. In the next section the structure is discussed.

1.3.1. Structure

The structure of the work is strongly oriented towards the objectives. In addition, the structure is also divided into parts. This division is easy to make because three different types of research are carried out. The experiment and the simulations are conducted side by side and interact only after the results are available. Before either of them can be carried out, a literature review is conducted, which precedes the experiment or simulation.

In Figure 1.1 a visual overview of the thesis is given. The three squares represent the main parts of the thesis, each housed in a different chapter. Each chapter consists of sections and subsections. The main ones are also shown in the Figure 1.1. At the end, the experiments and simulations are compared and the results are given. These should be in line with the aim of this thesis.

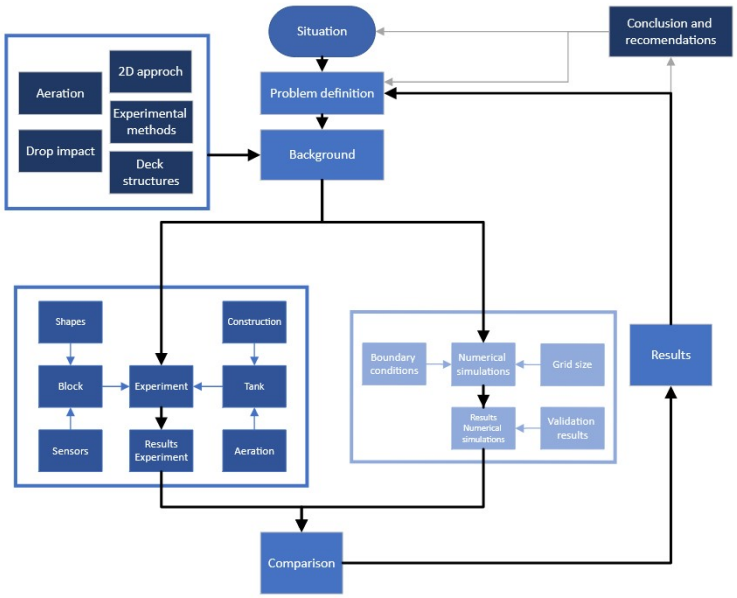

Figure 1.1: Structure of the thesis divided in main problem, experiment, numerical simulations and relation between the different topics.

This is the end of chapter 1.1, which is the introduction to this work. In chapter 2 the background of the problem is explained. This is mainly about the literature that is used to investigate the problem. After chapter 2, chapters 3 and 4 focus on the experiments and numerical simulations. The results found in both chapters 3 and 4 are summarised in chapter 5, after which the concluding remarks on this thesis are given in chapter 6.

2

Background

This chapter will focus on the literature that has been used to gain a better insight into the implications of GW impact. In addition to GW research, the focus is also on the drop effect. After this chapter, the properties of a GW wave are known. All properties can be transferred to an experiment in such a way that a reliable experiment can be constructed.

First, the 2D representation of the problem is given and the 2D approach is justified. This is followed by the theoretical speed that can be achieved. Secondly, the choice of experimental method and numerical simulation is explained. The aim of this research is to understand the effects of a deadrise angle and aeration on impact. Therefor the research done on both aerated impact and the impact with wedges will be studied. This will lead to a first estimate of the expected impact pressures. At the end of this chapter all the information on how the experiment is set up and how the simulations are carried out.

2.1 Two Dimensional Approach

Impacts are unpredictable and complex in nature due to 3D effects occur. However, part of the aim of this work is to determine the effects of the deadrise angle on impact. Other effects that do not contribute to this effect should be omitted as much as possible. Therefore, a 2D impact is advantageous. By creating a 2D impact, 3D effects are eliminated as much as possible. By creating the 2D space across the cross-section of the wedge, the effects found are only due to the deadrise angle.

A numerical model can easily be restricted to 2D space. This can lead to valuable results about the influence over the width. The effects of a 2D effect can be studied quite easily without additional 3D effects.

The difference between 2D and 3D effects is studied by Sang-Yeob Kim and Yonghwan Kim in relation to sloshing in Liquefied Natural Gas (LNG) tanks [23]. 3D and 2D experiments were conducted using a model-scale tank and a model-scale disc. It was found that although the critical excitation frequency was similar, the 3D test had larger pressure peaks. However, it is said that this may be an effect due to swirling, which is typical of tank sloshing and less common in Green Water (GW) impacts. The tank used to study 2D effects has a width of $760mm$ and a depth of $110mm$, resulting in a width-to-length ratio of about 14.4%.

An experiment will always have 3D effects in some way. However, these can be omitted as much as possible. One way is to restrict the flow in the third dimension as much as possible. This can be done by using a thin third dimension and keeping the edges in the third dimension as small as possible. Using a thin third dimension should not cause unwanted boundary effects.

For a numerical experiment, a 2D or a 3D model can be used. A 3D simulation should be more accurate, but also takes more time to compute and is more complex. From previous research, SPH methods are preferred for GW impacts. The advantage of an SPH method is that it can be easily used for 3D and highly

perturbed flows. However, if the experiment of a wedge is studied, a meshed numerical 2D simulation is sufficient. A 2D meshed numerical simulation is simpler and therefore less time consuming, while providing reliable results.

2.1.1. Theoretical Velocity

One of the most important contributors to maximum pressure is velocity at impact. Velocity is also a variable present in a GW wave. Therefore, the GW impact is highly dependent on the velocity of the wave front.

The 2D approach is first mentioned and supported by Buchner [5]. Later, Barcellona et al. [2] with 3D experiments that the velocity of the wavefront is not particularly affected by the bow shape on the centreline. These 2D Dam-Break approach, however, is only valid if the bow shape is blunt and without flare. Furthermore, the experiments focus on anchored Floating Production Storage and Offloading (FPSO) units. For these stationary vessels, an impact without forward motion is sufficient. Most experiments focus on a 100-year wave impact.

A DB experiment thus applies to a blunt bow without flair under stationary conditions. However, most ships and especially naval ships do not comply with this. A simple DB experiment would therefore not suffice. It is to be expected that an DB experiment would not be suitable to measure the effects when used as a basis for the experiment. In an DB problem, the maximum velocity depends on the height of the water behind the dam h_0 and the gravitational constant g (equation 2.1).

$$u_f = 2\sqrt{g \cdot h_0} \tag{2.1}$$

The velocity given in equation 2.1 is the supercritical flow velocity [9]. This is the velocity of the tip of the surge when the dam is removed. The supercritical flow is the maximum flow that the wave front can reach when the fluid is initially at rest. In Figure 2.1 the representation is given.

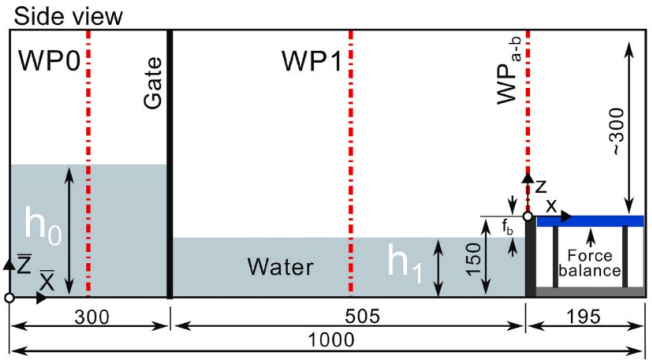

Figure 2.1: A dam break experiment as done by Hernandez-Fontes [20]. When the gate is removed the water flows to the structure creating a single GW wave.

Besides a DB event, there are other types of GW events such as PDB and HF events. These types of events are expected to lead to a stronger vertical impact on the deck. The horizontal component will be much smaller than the vertical component of an DB event. This means that if the velocity of the wave when it hits the deck is zero, the maximum velocity of the wave will not exceed the equation 2.1. Pham [31] improves the DB experiment by adding an initial velocity. Pham examines only the vertical impact and finds that the DB experiment underestimates the vertical pressures on the deck.

However, a clear numerical simulation showing the velocities on the deck is given by Chen et al. [8]. For these numerical simulations, a Wigley hull and open-source code is used to predict the GWloading on the deck. Chen finds the effects on heave and pitch for various wavelengths including GW. The Figure 2.2 also shows that the speed of the wave on deck is higher than the ship's speed.

Figure 2.2 shows the flow for a Wigley hull through waves. The Figure shows the flow development on

deck, where a wave can be seen above the centre line, which is about 1.5 times higher than the ship's speed. Next to it, the development of the GW flow can be seen. The broken flow and the high-speed surge can be seen at the wave front.

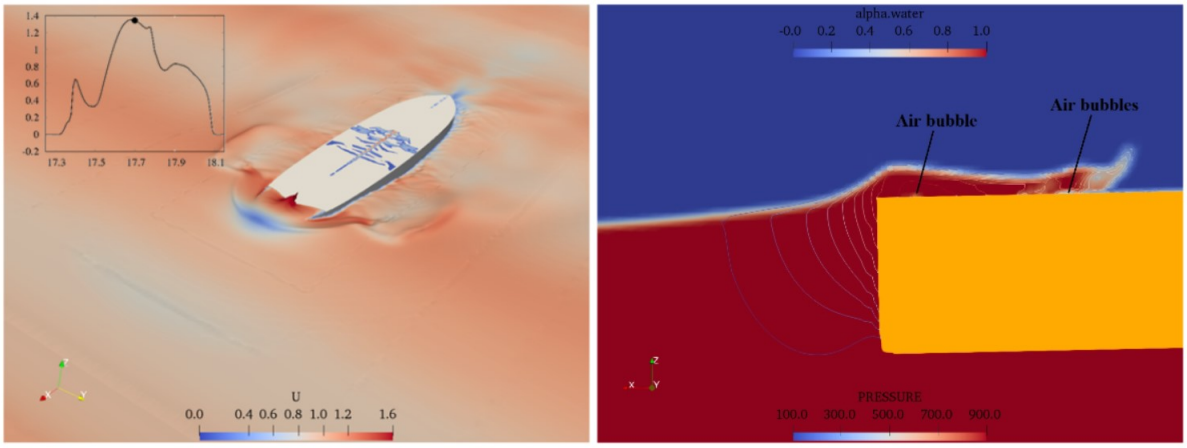

Figure 2.2: The flow on deck for a Wigley hull moving with a ship speed of $1 m/s$. On the left Figure, the flow on deck exceeding around $1.6 m/s$. This can be identified by a narrow dark point over the center line. On the right is the flow over the center line given in more detail. Due to the ship-wave interactions air bubbles are created in the GW [8].

Finally, due to the interest in structures on deck, the influence of deck length and roughness in relation to speed on the deck is investigated. Rodríguez-Ocampo et al. investigated the influence of deck length and deck roughness using numerical simulations and a wet DB experiment[35]. Twelve cases were studied for six different deck roughness and lengths. The results are shown in Figures 2.3A and 2.3B for roughness and in Figures 2.4A and 2.4B for deck length.

In the Figures 2.3 and 2.4 it can be seen how the vertical (vv) and horizontal velocity (vh) evolve for different deck roughness and length. The roughness leads to a slight decrease in the horizontal and vertical velocities. The effect is more pronounced for deck length. A longer deck leads to higher velocities, both vertically and horizontally. The impact moment on the structure also depends strongly on the deck length.

Looking at the 2.3 and 2.4 Figures, it is clear that the deck has an influence on the speed of the ship's structure due to the location of the structure and the characteristics of the ship. In addition, the bore velocity of a Green Water wave on deck is also strongly influenced by the ship's speed and the shape of the bow. The bore velocity on the structure depends on a large number of independent variables. Determining the experimental velocity can lead to a fixed value that cannot be explained.

It can be stated that the velocity on deck is highly dependent on two characteristics. The first is the wave height when the water arrives on deck. This is an interaction between the wave height and the local freeboard. In addition to the wave height, the difference between the velocities of the wave and the ship can contribute to the speed of the GW wave. The velocity on deck is therefore highly dependent on the characteristics of the vessel and the current sea state.

2.2 Experimental Methods

Various methods of studying the effects of GW have been considered. This section explains the requirements for a valid experiment and then justifies the choice. The most common method for studying the effects of GW is a DB experiment. A DB approach is used for both the arrival of GW, the ovetopping of the bow and the flow of GW entering the deck.

It is clear that a conclusive simplification of the Green Water on deck is not as easy to find as a DB event. For the effects on a structure, a different experiment is proposed. There are a few main reasons that justify a different approach:

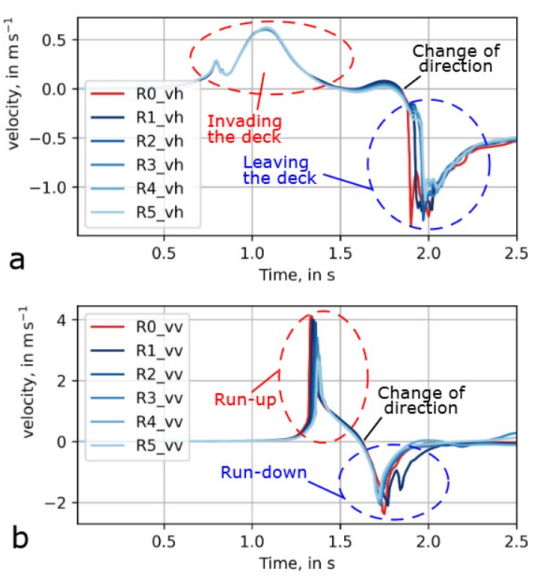

Figure 2.3:
A: Horizontal flow on the deck with different deck roughness. The roughness has no influence on the velocities on the deck. However, it does influence the return flow velocities. When the roughness increases (R05), the velocities decrease slightly.
B: The vertical flow on the deck with different deck roughness. The deck roughness decreases the vertical velocities. At R05, the velocity decreases by 35% compared to a decrease of 5% at R01[35].

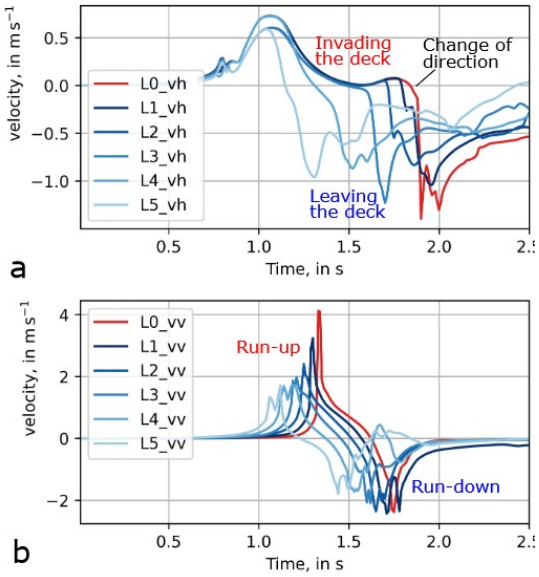

Figure 2.4:
A: Horizontal flow for different deck lengths. When the deck length increases (L01) the maximum velocities will increase. An increased deck length leads to more acceleration.
B: Vertical flow for different deck lengths. The increase in deck length is related to the maximum run-up and run-down [35].

- The impact on a structure result from the characteristics of the ship and the waves. However, these vary according to the sea state and the ship. There is no clear connection with the bore velocity and the waves.

- The shape of the structure in width will affect the effect on the impact. With a 2D DB approach across the centre line, the effect of the shape is not visible. Therefore, the GW wave will only be confined perpendicular to a structure. An experiment across the width will give a better insight into the influence of the different shapes.

- The aim is to find an estimate for impact, taking into account shape and aeration into account. Therefore the maximum impact is needed. Deck effects that slow down the impact and waves that create a more turbulent flow can reduce the magnitude of the impact.

By dropping a sample on a body of water, the impact on the body can be measured. This type of experiment can be designed to meet the requirements of the Green Water experiment. The experiment in which a sample is dropped onto a water surface in this case is called a drop tower experiment. In addition to a drop tower experiment, a suitable numerical simulation can reinforce and support the findings from a drop tower experiment.

Experiments and numerical simulations both have their own advantages and limitations. These are listed in the table 2.1.

2.2.1. Drop Tower Experiment

Drop tower experiments can be used in many different ways. The main goal of a drop tower is to accelerate an object or to reach a certain velocity. In aerospace engineering, drop towers are used to create moments of microgravity [12]. However, in materials science or fluid dynamics, the impact between a structure and

Table 2.1: The advantages and disadvantages for both experiments and numerical simulations. Most of the advantages for a simulation are a disadvantage for the experiment and vice versa. When comparing the advantages from both it can be seen that they complement each other.

Experiment	**Numerical Simulation**
Advantages	**Advantages**
Quick run-time	Purely 2D effects
No false effects due to coding	Easily scalable
Mistake can still lead to usefull results	Changing variables is quick
	Continuous Results
Disadvantages	**Disadvantages**
(Unwanted) 3D effects	Long run-time
Changing variables laborious	Coding can result in false effects
Discrete results	Error gives no results
New scale requires a new experiment	

another structure or fluid is used. In summary, a drop tower provides a simple way to create and study an impact.

When using a drop tower experiment, there are some points that should be considered before setting up the experiment. The experiment should simulate the intended Green Water wave in 2D across the width, so the experiment should be designed to minimise 3D effects. Furthermore, the velocity of the impact should be within the range of possible wave velocities.

In addition to the speed of the impact, the shape can also be changed. By changing the shape, different impact angles can be considered. A drop tower can result in a valid 2D impact of a wave on an inclined structure.

2.2.2. Numerical Simulation

A numerical simulation can be used to support the experiment. Some of the advantages of a numerical simulation are exactly the opposite of those of an experiment. By using a numerical solution alongside an experiment, gaps in the data caused by discrete measurement locations can be filled. It is important that the numerical simulation is similar to the experiment.

Changing the variables for a numerical simulation is relatively easy. This means that the width, height, scale or other features can be changed easily. With an experiment, this is not so easy. Every time a characteristic is changed, the experiment must also be changed. However, the values of the experiment cannot contain errors due to coding. If a numerical simulation is validated with an experiment for the same dimensions, the error of the simulation can be better estimated. If the error in the simulation is known, the properties can be changed so that the reliability of the results can be better estimated.

This is because the input variables for a numerical simulation can be easily changed. This property can be easily used to test the simulations. For example, the deadrise angle can be easily changed to investigate the effects when the angle in the experiment is slightly different. The simulations can also be used to scale the experiment to the desired size.

2.3 Deck Structures

When a drop tower is used as an experiment, the translation should be made between a wedge and deck structures. This is done in two ways. First, the wave front velocity should be converted into a drop velocity and an impact velocity. Secondly, the angle should be taken into account. The effect of aeration is strongly dependent on the deadrise angle, in addition to the air content in the water.

Green Water waves for most ships will arrive on deck perpendicular to the structure, as assumed in most DB experiments. And even if this is the case, not all structures are perpendicular to the wave front. Therefore, the shape of the structure will influence the impact.

$$E = E_{kin} + E_{pot} = \frac{1}{2}mv^2 + mgh \tag{2.2}$$

$$W = F_{avg}s \tag{2.3}$$

$$F_avg = \frac{m \cdot v^2}{2s} \tag{2.4}$$

Looking at the equations 2.2 and 2.3, which are the general equations for energy and work, we find that in an impact where energy is converted into work, the average force in equation 2.4 [37]. In a wave impact, the energy is mainly kinetic energy. However, in a drop tower experiment, the energy in the system is mainly potential energy (2.2). This force depends on the mass, the deformation zone and the velocity. If the type of structures and the wave impact are identical, the only variable is the velocity. For the impact, the velocity perpendicular to the shape should be taken. In equation 2.5 the difference between the frontal velocity and the impact velocity is given. On impact, the velocity component can be resolved into the velocities perpendicular and parallel. In general, this means that the total impact is lower when the impact is oblique.

$$v_i = v_e \cdot tan(\alpha) \tag{2.5}$$

When only examining the velocity the effect depends exclusively on the velocity and the angle. However, other aspects should also be examined. When a wave front hits a flat plate directly, air is trapped between the wave front and the plate. This trapped air dampens the impact on the structure [21, 28]. It is expected that such an air cushion effect will result in a lower pressure on impact. The air cushion effect actually occurs with a flat panel.

Compressible fluids may also experience a reduction in pressure. The reduction in pressure depends on the Mach number (M). The Mach number used is the edge Mach number introduced by Skalak and Feit. [36]. In equation 2.6, the edge Mach number is given as the edge velocity (v_e) and the speed of sound through the medium (c) and as a function of the edge velocity as the impact velocity as given in equation 2.5.

$$Ma = \frac{v_i}{c \cdot tan(\alpha)} = \frac{v_e}{c} \tag{2.6}$$

In 2017, Elhimer conducted experiments on the influence of air during wedge impacts [11]. He found that when the Mach number is greater than 0.3, compressible effects occur and the impact is related to the initial void fraction and the Mach number. When the Mach number exceeds 0.3, highly non-linear effects occur.

Since there is air in the water, several wedges should be tested to compare the effects. With two wedges and a flat plate, the change in pressure should be comparable as the deadrise angle increases. In the next section, the effect of aeration is used to determine the final deadrise angle of the wedge.

It is expected that by systematically changing the deadrise angle, the impact can be determined as a function of the angle. The impact is expected to depend on both the degree of aeration and the deadrise angle.

2.4 Aeration

GW is expected to have some kind of aeration However, this can range from non-aerated water to 3% [7]. By conducting experiments with different degrees of aeration, the influence effect of aeration on the impact can be determined.

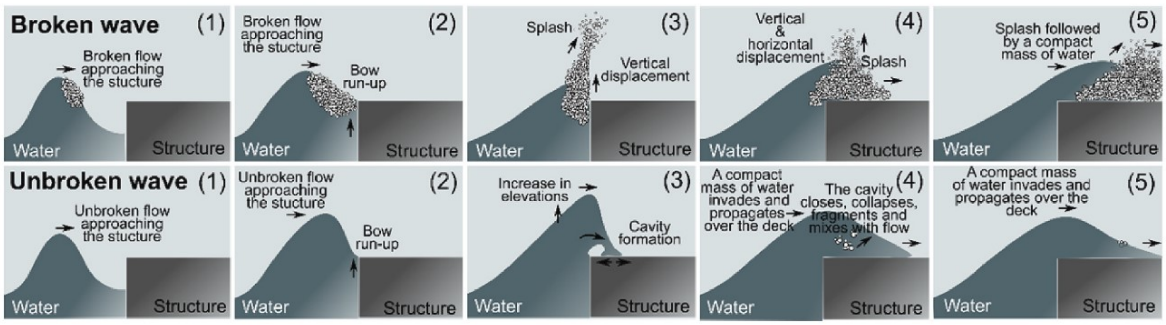

Figure 2.5: A typical broken and unbroken flow on deck. For a broken and unbroken flow the development of the arrival on deck is given. It can be seen that a broken flow will result in an aerated flow on deck. For an unbroken flow it can be seen that there is some air in the wave. However, it is possible that it dissipates in the flow itself [19].

Air is introduced into the water in different ways. At first the sea state in which GW will ocur introduces air into the water. In addition, air can also enter the water through the overturning of the bow. An aerated impact is different to a pure water impact. Because of the air in the system, the water can possibly behave like a compressible liquid. Elhimer's work [11] examines impacts, focusing on the relationship between wedge entry and magnitude of the impact. It is found that the fluid behaves incompressibly when the impact has a Mach number less than 0.05. When the Mach number is above 0.05 to 0.3, the effects of compression are not significant. When the Mach number reaches 0.3, this cannot be accounted for only by the void fraction and the sound velocity of the mixture due to the non-linearity effects in the equation of state of the aerated water and the decrease in the air volume fraction due to the pressure generated by the impact. The aeration used should be such that compressibility effects occur in some experiments.

After examining the individual waves and types of Green Water, Hernández-Fontes [19] examined the combined, broken and partially broken waves. Both types of waves are expected when Green Water occurs [16, 18, 33]. These experiments are conducted to find the flow of more violent waves. In the snapshots, it can be seen that a Green Water flow will generally consists of more air due to the broken waves arriving on deck. In Figure 2.5, the typical broken and unbroken flows as aDB and PDB are given.

As given in the equation 2.6, the Mach number depends on the impact velocity, the deadrise angle and the speed of sound through the volume. The impact velocity is a variable that depends on the experiment. The deadrise angle is a shape variable. The only variable that is affected by aeration is the speed of sound through the volume. The speed of sound through the water is assumed to be a result of the stiffness of the mixture (k_s) and the density (ρ), as given in equation 2.7.

$$c = \sqrt{\frac{K_s}{\rho}} \tag{2.7}$$

The degree of aeration in the mixture is the volume fraction (β). The volume fraction indicates the percentage of air in the mixture. To determine the effect on density, the equation 2.8 is used. The density of the mixture is a combination of the density of air (ρ_a) and water (ρ_w) in relation to the volume fraction.

$$\rho_{mix} = \beta \cdot \rho_a + (1-\beta)\rho_w \tag{2.8}$$

The stiffness of the mixture can be determined from the ratio between the stiffness of water and air in relation to the volume fraction. In the equation 2.9 the relations between water and air and the mixture are given in the appendix A.

$$\frac{1}{\rho_{mix} \cdot c_{mix}} = \frac{\beta}{\rho_a \cdot c_a^2} + \frac{1-\beta}{\rho_w \cdot c_w^2} \tag{2.9}$$

In the Figures 2.6 and 2.7. the development of the speed of sound as a function of the volume fraction is shown. The speeds of sound through air and water are ($c_a = 343[m/s]$ and $c_w = 1480[m/s]$). The density for both is ($\rho_a = 1[kg/m^3]$ and $\rho_w = 1000[kg/m^3]$). When air is introduced into the mixture, the speed of sound decreases rapidly. It reaches a plateau before it reaches the speed of sound through air. Since there is no more than 8% of air in the system, Figure 2.7 shows the evolution over a smaller volume fraction. From Figure 2.7 it is clear that the difference between 4% and 8% for the speed of sound is not significant.

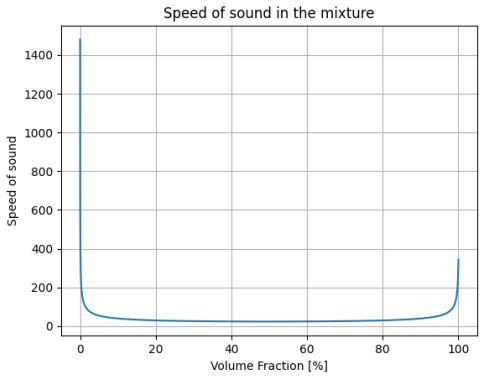

Figure 2.6: Speed of sound through a mixture of air and water. The When air is added in the water the speed of sound reduces rapidly. Speed of sound is used to determine the Mach number.

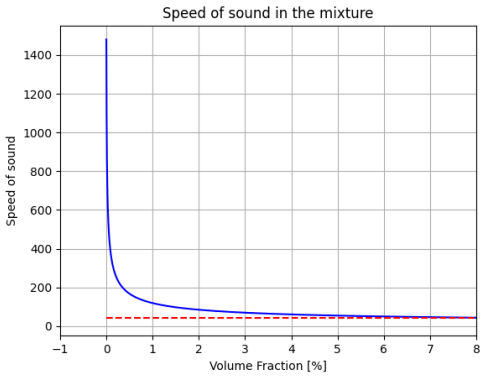

Figure 2.7: In Figure 2.6 the development of the speed of sound is given for the level of aeration. However, not more than 5% aeration is expected to be possible or required. Therefor the speed of sound is given here until 8% to give a better Figure of the development.

The significance of the difference between 4% and 8% becomes even clearer when we consider the Figure 2.8. This Figure shows the relationship between volume fraction and Mach number for different deadrise angles. The drop velocity is fixed at $7[m/s]$. It can be seen that no compressible effect occurs for wedges with a high deadrise angle dropped at this velocity. For wedges with very low dead rise angle ($\alpha < 1$), the compressible effect occurs even in pure water. The tipping point appears to be at about 15°. In a low-aeration impact, the wedge becomes non-compressible. However, if there is more than 2% of air in the mixture, the wedge becomes compressible.

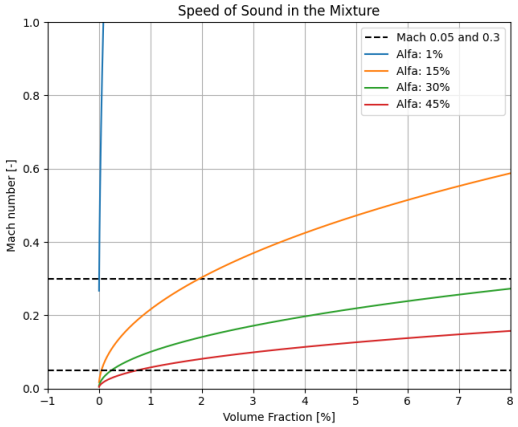

Figure 2.8: Compressible effects are present when the Mach number is higher than 0.05. When the Mach number increases above 0.3, strongly non-linear effects occur. The fall velocity is fixed at $7[m/s]$.

It can be seen that for reasonable achievable values of the drop velocity and aeration the wedge can be dropped with a 15° angle with both compressible and incompressible effects. Figure 2.9 supports this. Figure 2.9 shows the drop velocity and Mach number for a fixed aeration of 5%. It can be seen that the wedge with 15° also crosses the Mach 0.3 line almost halfway. The wedges with a higher deadrise angles experience compressible effects only at a much higher velocity and vice versa for the wedges with a low deadrise angles.

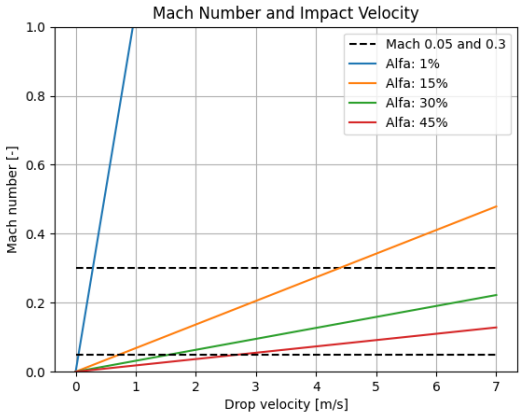

Figure 2.9: If the volume fraction is fixed at 5% the Mach number for the different drop velocities. Only in the case of a flat plate and a wedge with a small deadrise angle do strongly compressible effects occur (Mach greater than 0.3).

With a degree of aeration of 5% and the drop velocity is around $7[m/s]$, three different types of experiments can be carried out in relation to the aeration effects. At different deadrise angles, aeration can occur for aerated water and for non-aerated water. The three options considered are:

- A flat plate will be dropped with compressible effects independent of the aeration in the system.
- A wedge with 30° deadrise angle will not experience compressible effects even when air is added to the system.
- A wedge with 15° deadrise angle can be dropped in pure water and will not experience compressible effects. However, when air is added to the system compressibility plays a role.

By examining different types of compressible impact for different levels of aeration, an estimate of the impact on the impact can be made. The combination of shapes and aeration levels is chosen so that there are no compressible to strongly non-linear compressible effects. The results of this range of shapes and levels of aeration should lead to a full understanding of the effects of shape and aeration separate and combined.

2.5 Drop Impact

For the construction of the experiment it is advantageous that an initial estimate of the impact of GW is known. The estimated impact is used for the selection of the pressure sensors. The predicted impact pressure can also be used to estimate the forces on the wedges and flat plate to prevent them from breaking or deforming. Similar experiments are explained in this section.

By studying different drop impacts that are either 2D and 3D, the influences and predictions for a 2D drop tower impact can be determined. A first estimate of the range of possible impacts can be made.

It is assumed that for green water the impact is strongest at the moment when the water mass hits the structure [6]. This is also true for drop impact. Both the pressure and the force will increase rapidly on the structure. Aerated water is expected to dampen the impact somewhat due to the compressible properties of the air in the system. However, as can be seen in the section 2.4 this is highly dependent on the drop velocity, aeration and deadrise angle. Buchner's results for a typical pressure impact can be seen in Figure 2.10. Bucher does not take aeration into account. In this Figure, the impact pressure can be seen as the peak moment after the green water hits the structure. The peak impact in Bucher's work is further determined by the speed on deck (u), the density (ρ) and a constant (C) that depends on the shape of the structure, formula 2.10. It should be noted that the values for C determined by Buchner are empirical.

$$p = C\rho u^2 \tag{2.10}$$

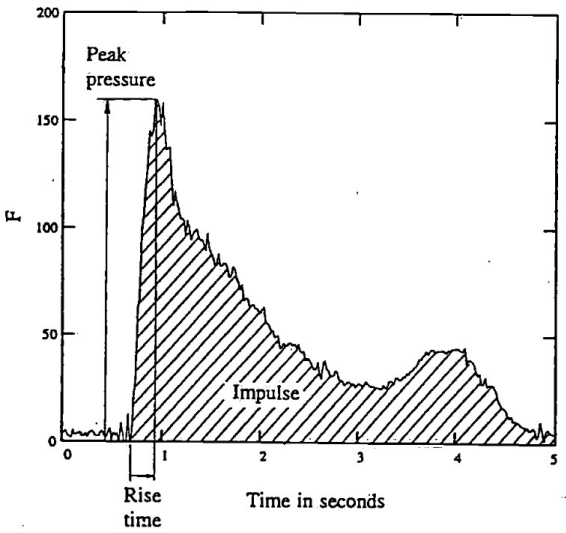

Figure 2.10: A typical effect of a green wave of water on a structure. Given by Buchner [6]. Three main features of pressure can be seen. Pressure rise, peak pressure and the evolution of pressure over time. At impact the pressure rise quickly after which it drops more gradually.

2.5.1. Investigation of Wedge Entry

An article by Nikfarjam et al. [27] gives an insight into the influence of different deadrise angles of a wedge. Nikfarjam uses three different wedges with deadrise angles of 15°, 20° and 30°. The weight and drop height are also varied. It is important to note that the experiments are conducted in such a way that 2D effects are predominant.

$$z^* = \frac{h_{drop}}{v_i \cdot t} \tag{2.11}$$

$$C_p = \frac{P_{impact}}{1/2 \cdot \rho \cdot v_i^2} \tag{2.12}$$

In conducting the experiments with different wedges, Nikfarjam [27] uses two non-dimensional coefficients. These are given in equation 2.11 and equation 2.12. In equation 2.11 the non-dimensional depth is given. This results from the height of the drop height divided by the impact velocity and the time. The pressure coefficient consists of the pressure divided by the dynamic pressure of the object moving at a velocity with density ρ.

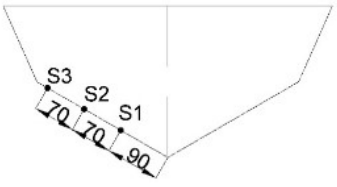

Figure 2.11: Positions of installed pressure sensors on the wedge from the tests of Nikfarjam. [27] The results of the data can be found in Figures 2.12 and 2.13.

In the experiments conducted by Nikfarjam, [27]sensors are placed on the wedge. The sensors are placed at equal distances. However, the first sensor is slightly further away from the tip. This can also be seen in the Figure 2.11.

The results for a particular wedge are shown in Figures 2.12 and 2.13. Both wedges are dropped from a similar height and have a similar weight. The only difference is the deadrise angle. The drop height is 100 centimetres. Because of the similar drop height and weight, the impact velocity for both wedges is identical at $4.43 m/s$.

There are a few things to note when comparing the two impacts. The pressure profile shown in the Figure 2.10 can be seen. The sharp peak with some secondary loads is more evident in the wedge with a deadrise angle of 15 degrees. The secondary loading due to buoyancy can be seen in both Figures 2.12 and 2.13. What can also be seen is the difference in maximum impact. The maximum impact for the deadrise angle of 15° is three times the impact for 30°. It is also obvious that the impact is more unstable for a wedge with a deadrise angle of 30°. This can be concluded from the differences between the pressure values of the sensors for both shapes.

In summary, the projected area decreases as the deadrise angle increases. This leads to a lower impact pressure.

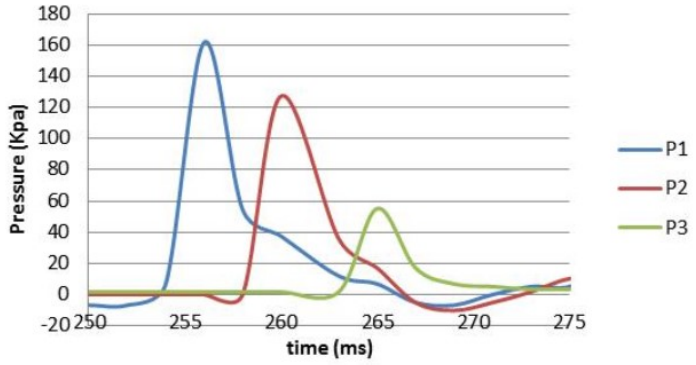

Figure 2.12: The results of a wedge dropped from 100 cm with an deadrise angle of 15°. The wedge achieves a velocity of $4.43[m/s]$. The locations of the sensors which registrate the pressure can be found in Figure 2.11

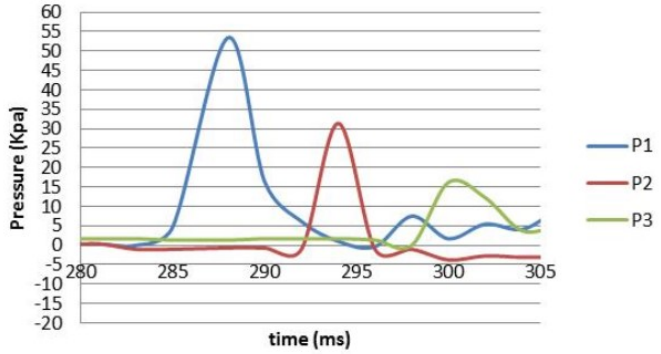

Figure 2.13: The results of a wedge dropped from 100 cm with an deadrise angle of 30° which can be seen in Figure 2.11. The wedge achieves a velocity of $4.43[m/s]$. The locations of the sensors which registrate the pressure can be found in Figure 2.11

Nikfarjam [27] also examines the importance of weight and drop height on outcomes. It is found that the height of fall has no direct influence on the impact. However, the drop height does influence the impact velocity. For the deadrise angle, the effect is significant.

2.5.2. Investigation of Flat Plate Impact

In addition to wedge impact, there is also research on flat plate impact. Ma Z et al. [24] studied the impact of a flat plate in water with and without aeration. Unlike Nikfarjam [27], Ma Z also investigates the three-dimensional effects. However, due to the complete symmetry of a flat plate, both can be compared. A square

plate of $0.25m$ is used for the experiments. Five pressure sensors are attached, which are shown in the Figure 2.14.

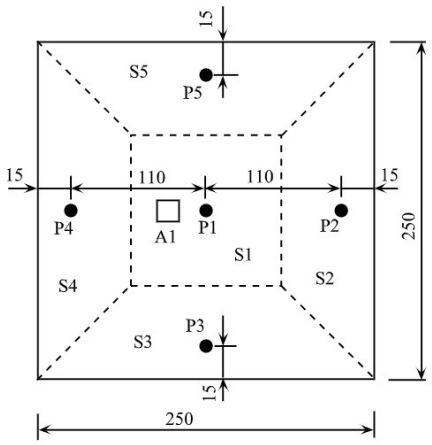

Figure 2.14: Layout of the plate including locations of the pressure sensors (P), influence areas (S) and the accelerometer (A1). (Units in mm) [24]

Ma Z [24] compares the results of two blocks with a different mass. The first block has a mass of $32[kg]$ and the second block has a mass of $52[kg]$. Ma Z also varies the velocities between 4 and $7[m/s]$. The results of Ma's pure water ingress are shown in Figure 2.15.

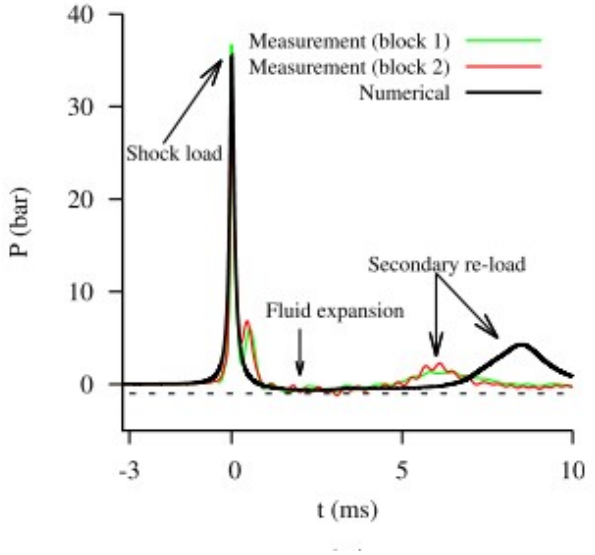

Figure 2.15: Impact pressure of a flat plate. The impact velocity is around $7[m/s]$. The blocks 1 and 2 have a different mass.

In Figure 2.15 it can be seen that the pressure is highest shortly after impact and decreases rapidly. This is comparable to the wedge impact in Figure 2.12. However, due to the difference in velocity, weight and shape, the peak for the wedge entry is lower and more widely distributed than for a flat plate entry. A small peak for the second block is seen immediately after the peak load. This peak is probably due to the pressure wave passing through the water and returning to the block. Secondary loading is also shown, indicating a difference at the moment of secondary loading. However, the secondary load is not in the area of interest.

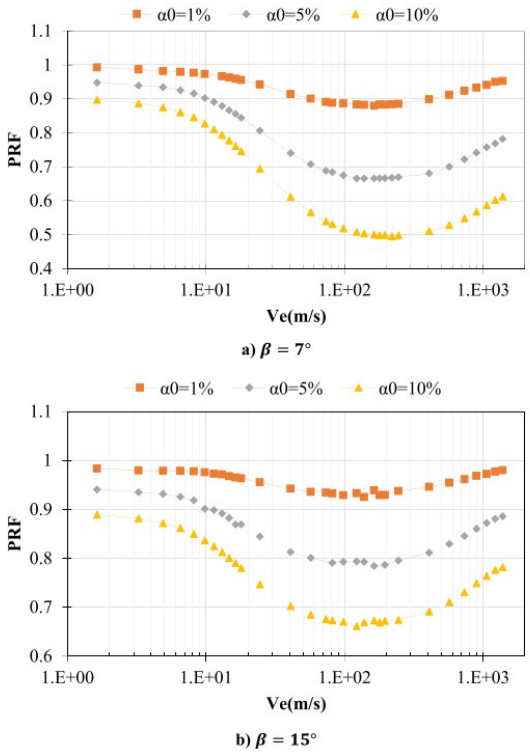

Figure 2.16: Average PRF from numerical simulations for different levels of aeration. The difference between the graphs is the deadrise angle β and the degree of aeration α. It can be seen that the pressure drops sharply at high speeds. A GW wave would be in the range of 0 to 10$[m/s]$.
A: Deadrise angle of 7°
B: Deadrise angle of 15°

2.5.3. Investigation of Aerated Impact

Aerated impact has been researched in various forms. This subsection looks at some of that research.

When air is added to the system, the maximum pressure is defined by the sound pressure. This is a result of research by Von Karman, who tried to find a theoretical formula for the impact of a flat plate on water. The formula found is called the acoustic pressure and is given in the equation 2.13.

$$P_{acoustic} = \frac{\rho v_i^2}{2} \cdot \frac{2c}{v_i} = \rho v_i c \tag{2.13}$$

The acoustic pressure is expected to be the highest pressure possible in the impact of a flat plate. It is also expected to be much greater than the pressure found by Buchner (2.10) for a structure because the speed of sound is added.

While Nikfarjam has done tests with wedges falling from height with different properties [27], Elhimer has done something similar with cones and different deadrise angles [11]. However, both did experiments for shapes with different deadrise angles, with Elhimer focusing on the effects of aeration in the water. This aeration can lead to non-linear effects due to the compressibility of aerated water. As shown in section 2.4, the results of this research are used to determine aeration and deadrise angles.

Elhimer shows that the pressure at low velocities depends on the density ratio of aerated and pure fluid. This means that the impact pressure depends only on the decrease in mass density due to the presence of air. At higher velocities, the Pressure Reduction Factor (PRF) depends on the edge velocity. It should be noted that the reduction in force is greater than the reduction in pressure. This is probably due to the effect of aeration on the surface. The PRF for a 7° and a 15° angle can be seen in Figure 2.16.

With a flat plate, the impact in the aerated water is somewhat different from that of a wedge. Ma Z has studied the impact of a flat plate on a body of water for non-aerated water and aerated water [24]. It can be seen that the impact of a flat plate decreases sharply when air is added. As can be seen in the Figure 2.9, the Mach number increases even at low velocities. This means that the effects depend on the edge velocity and the density ratio in the mixture. It is also to be expected that the surface area has an influence. The surface area of a flat plate increases rapidly, from no contact area to almost full area.

Secondly, from the comparison between numerical simulations and experiments by Ma [24], it appears that a flat plate does not fall uniformly. In the numerical simulations, the peak is in the same place for all pressure sensors. However, when comparing with the experiments, it can be seen that for some sensors a clear pressure peak is not clearly visible or is later than the moment of impact. This is also a consequence of the disturbed water surface due to aeration in the system. In a numerical simulation, the water surface will be undisturbed. In Figure 2.17 the impact on the pressure sensor $P1$ can be seen. In the appendix A.2 the impact on the pressure sensors $P2$ to $P5$ can be found. The locations of the pressure sensors can be seen in Figure 2.14.

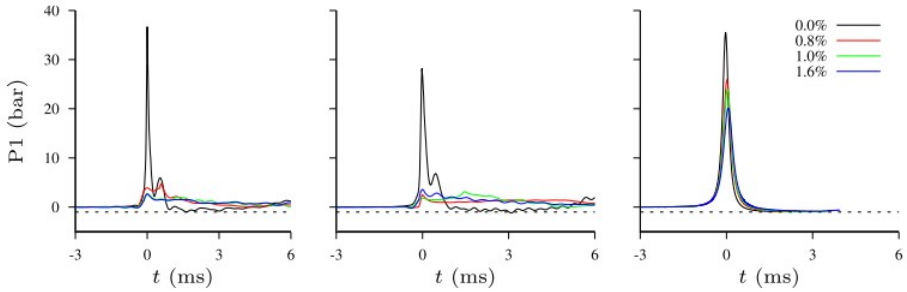

Figure 2.17: Development of the pressure for the different blocks. From left to right: 32$[kg]$, 52$[kg]$ and the numerical simulations. It can be seen that there are no secondary effects in the numerical simulations, whereas they certainly occurred in the experiment. Secondly, the decrease in maximum pressure is larger in the experiment than in the simulation [24].

In addition to a decrease in impact pressure, Yao Hong finds that the duration of impact is also longer. Hong conducts tests with a disc impact through a drop tower for pure and aerated water. He concludes that the aeration and the air cushion under the disc reinforce each other and reduce the impact even more than a pure aerated impact. A flat plate or disc also provides a more even distribution of pressure than a hyperbolic one when air is added.

From these studies, it can be concluded that air reduces impact. In the case of a wedge, the deadrise angle and the degree of aerateion determine whether the compressible effects influence the impact. When air is added to a flat plate, there is always a compressible effect. Besides the effect due to the aeration of a flat plate, there is also an effect due to the air cushion between the water and the plate. In the case of an impact on a flat plate, the aeration leads to an even stronger reduction of the impact because the aeration increases the air cushion effect.

The sound pressure can be determined from the equation 2.13. The acoustic pressure is the maximum possible pressure. If an impact velocity of 7$[m/s]$ is assumed. The pressure ranges from 103Bar for a non aerated impact to 4.08Bar for a 4% impact. The maximum pressure that could be found for the impact pressure is therefore 103Bar.

However, if one examines the pressures found in the literature, one can find a better estimate for the maximum pressure. However, the experiments do not always take place under similar conditions. When testing for maximum pressures only, the wedges are dropped with 15° and 30° angles at a velocity of 4.43$[m/s]$ [27]. The maximum impact pressure determined for these wedges is 1.8Bar and 0.55Bar. For the flat plate with a similar area and a comparable velocity of 7$[m/s]$. When examining the impact, the maximum impact for the flat plate is found to be below 38Bar. Looking at these results, it is expected that the maximum pressure is lower than expected.

Pressures cannot be compared if they come from different experiments. However, if the pressures are all

converted into pressure coefficients, the pressures can be compared. The dimensionless pressure coefficient is given in equation 2.12.

For the wedges falling at a speed of $4.43[m/s]$, the pressure coefficient C_P is 18.35 and 5.62 for the wedges of 15° and 30°. The pressure coefficient for a flat plate is 155.41. These pressure coefficients can be compared with the results of the experiment.

It can be assumed that the flat plate has the greatest influence. Therefore, the maximum pressure is expected not to exceed $38Bar$. The maximum pressure is used to determine the range of the pressure sensors.

3

Experimental Method

All parts of the experiment are covered in this chapter. The steps to set up an experiment that replicates a GW experiment are explained in this chapter. In addition to the set- up of the experiment, the post-processing and the results of the experiments are also given.

One of the aims is to create an experiment that replicates the effects of GW in a representative way. This chapter explains the steps taken to create an aerated impact comparable to a GW impact. This includes the dimensions of the experiment and the steps taken to eliminate unwanted effects. It also explains how to generate the required velocity and aeration.

In addition, this chapter discusses the preparatory steps to be taken into account before setting up the experiment. After the preparatory steps, the set-up of the experiment is discussed. In section 3.2 and section 3.3 the contents of the two parts of the experiment are explained in more detail. In section 3.4 the rationale for the experimental design is given. To better illustrate the experiment, the collected data is processed. In addition to using a filter to smooth the data, the sensitivity of the data is also taken into account. In section 3.6 the results of the experiment are given.

3.1 Preliminary Steps

Subsection 2.2.1 explains the idea of a drop tower and why it is implemented. The main components of a drop tower are the tank, the block and the tower. The tower directs the block towards the tank and ensures that the block hits the water. By dropping the block, the impact can be determined both visually and with special sensors.

In the drop tower experiment used, the block consists of two parts. The upper part of the block is fixed and is mainly used to create a platform to which different shapes can be attached. Most of the parts that are attached in each experiment are part of the upper block. Among other things, the bearing and the cables are part of the upper block. The lower block was created to make it easy to change the mould. The lower block can be changed to install the desired shape.

In Figure 3.1 the experiment is shown. In this rendering of the designs, the tank, the weight and the tower can be seen.

Each experiment consists of the same steps. First, the block is lifted and attached to the magnet at the top of the tower. A rope running through a pulley at the top of the tower facilitates the lifting process and helps to keep the block on top of the tower before the magnet is attached. The cables of the sensors should be arranged so that a sudden movement cannot tear a knot in the cables, which could cause damage. When the block is securely attached to the magnet and the line is released, the block can be safely released. The block is automatically released when the measuring Data Acquisition (DAQ) hardware starts the experiment.

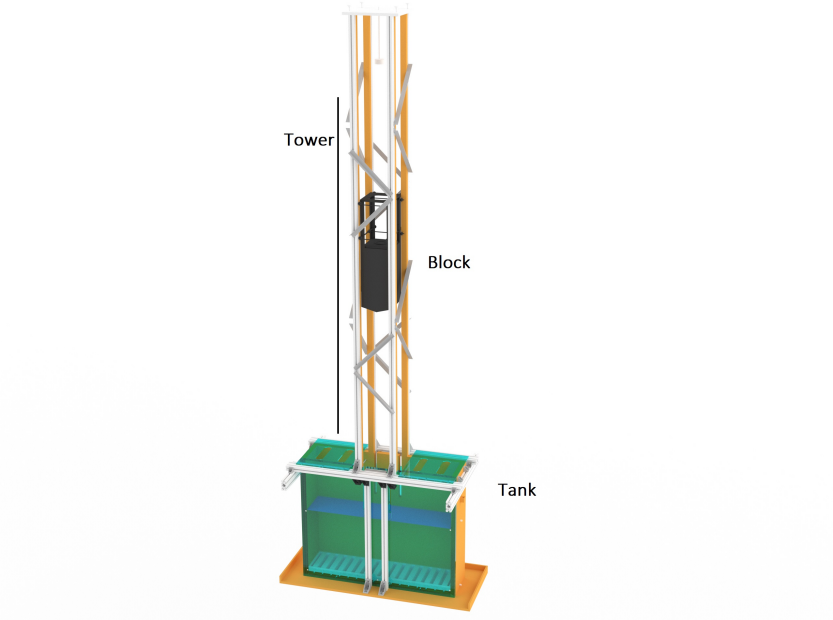

Figure 3.1: Render of the experiment where the block, tank and tower can be identified.

The experiment is a second iteration of an experiment constructed by van der Eijk and Vendeloo ([25, 38]). Based on the experiments they conducted, some improvements could be made, which have been incorporated into this work.

- The vibrations in the tank were visible in the results. Thicker side walls of the tank lead to a stiffer tank with a higher natural frequency. A higher natural frequency is less visible in the results and does not interfere with the frequencies in the water caused by the impact.
- In the first iteration, the bubbles were created by air blown under a perforated plate. A different method of bubble generation was chosen to improve the homogeneity of the mixture. It is expected that special air distributors will produce a more uniform flow of bubbles.
- In the first iteration, only one mould was used. Because of the way the original tower was constructed, changing the wedge was an intensive process. The improved version uses wedges that can be changed by loosening four screws. An additional advantage is that the pressure sensors in the wedge are easily accessible.
- The wave generated by the initial impact is reflected off the sides of the tank and flows into the centre. If the sides of the block are too short, the water can flow over the block and cause undesirable effects that are 3D in nature. By creating a higher freeboard on the block, this flow will not be possible and this result is expected to create fewer 3D effects.
- There are also a few small improvements. These are additions such as changing the position of the guide rails that were obstructing the view and valves at the waterline and bottom to improve the filling and emptying of the tank.

3.2 Block

The block consists of two parts that are screwed together. The upper part will consist mainly of parts that will not be changed and will support the impact. The lower part will be the form itself. In this section, all the parts that are connected to the block are discussed.

Figure 3.2 shows the upper block and the lower blocks or wedges and plate. The block has a width and length of 218$[mm]$ and 236$[mm]$. All dimensions can be seen in Figure 3.2.

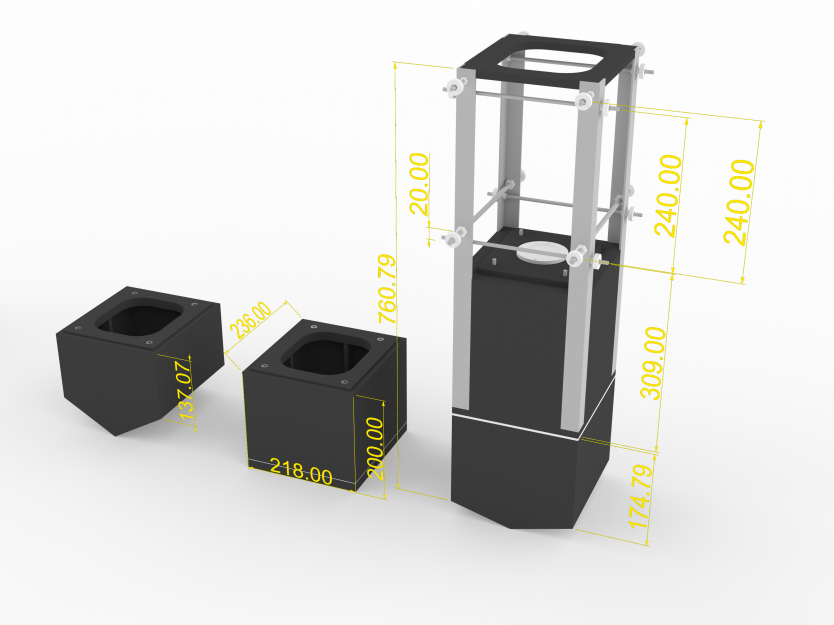

Figure 3.2: Render of the block with the different types of wedges. All measurements are given in millimetres. In this render the upper block is attached to the wedge with deadrise angle 15°. Both other shapes can easily be attached to the upper block. The main purpose of the upper block is to provide the guide wheels, and accelerometer. Pressure sensors are attached in the bottom shapes.

3.2.1. Top Block

The upper block is usually made of plywood and coated with epoxy. The connection between the upper and lower blocks is made as rigid as possible to reduce vibrations that could potentially cause false signals from the accelerometer. It is possible for the flat plate to deform under high impact pressures. To reduce deformation, the flat plate is reinforced with a layer of carbon fibre used on both sides of the plate. The reason for using carbon fibre instead of a thicker plate is to reduce the weight of the plate. For the full plate thickness and carbon fibre considerations, see the appendix C.

On the top of the block are eight ball bearings on metal strip profiles. These guide the block down with as little friction as possible. It is not intended that the block remains in constant contact with the tower. To create as little resistance as possible, some space is left between the bearings and the guide rails. The bearings limit the movement on the side to ensure that the block hits the water.

The magnet can be seen on the top of the block (grey circle in the illustration 3.2). The plate to which the magnet is attached can be removed to open the block. This allows easy access to the block to inspect the cables and sensors inside.

3.2.2. Wedges and Plate

In section 2.4 the justifications for the wedges and the flat plate are given. In addition to the preference of creating different effects the change in deadrise angle is used for comparison. The different shapes can be seen in section 3.2. Figure 2.9 shows the different compressible effects for the different levels of aeration and deadrise angle. The current setup of the experiment restricts a change in velocity. With three shapes, an optimum is created between the compressible effects and the number of shapes.

In addition to the 30° wedge, a wedge 15° wedge and a flat plate are chosen. It is expected that a trend for impact pressure can be identified for these three shapes, which can result into an estimate of impact pressures for other deadrise angles. The pressure sensors are located as close as possible to the centreline for the two sensors on the inside. The outer sensors are located as close to the edge as possible. The location is limited by the design of the wedge.

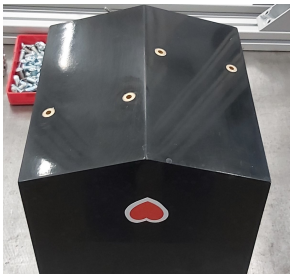

Figure 3.3: Wedge 15 with sensor locations, the installed sensors can be seen on both side of the wedge.

Figure 3.4: Wedge 30 with sensor locations, the installed sensors can be seen on both side of the wedge.

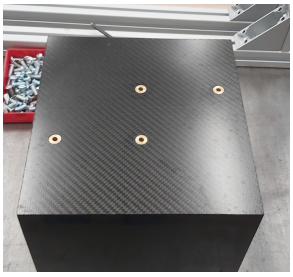

Figure 3.5: Flate plate with sensor locations, the installed sensors can be seen on both side of the wedge.

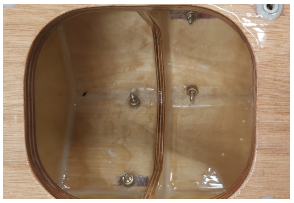

Figure 3.6: Inside construction of the wedge with 15° deadrise angle. The sensors can be seen inside.

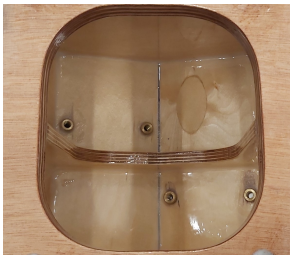

Figure 3.7: Inside construction of the wedge with 30° deadrise angle.

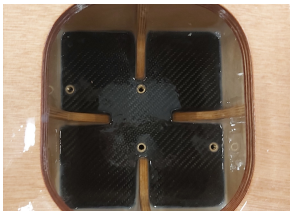

Figure 3.8: Inside construction of the flat plate. The carbon fiber layer can be seen on the inside.

In Figures 3.3, 3.4, and 3.5 the three wedges can be seen. At the bottom of the wedges the positions of the sensors can be seen. There are two sensors on each side. The distances between the sensors can be seen in Figure 3.10. In Figures 3.6, 3.7 and 3.8 the inside of the wedge is shown. Next to the sensors the reinforcement can be seen inside inside. The wedges are reinforced by a plate across the entire width. For the flat plate there are four small reinforcement plates and the carbon fibre can be seen inside.

Four pressure sensors are installed in each wedge and in the plate. In addition to the pressure sensors, an accelerometer is also installed in the upper block. The sensors are explained in more detail in the subsections 3.2.3 and 3.2.4.

3.2.3. Acceleration and Velocity

In each test, the block is dropped from a fixed height. The velocity of the block on impact depends on different aspects. The main contribution to the velocity is the potential energy in the system due to the height. However, other aspects such as friction in the guide rails or air resistance reduce the velocity. It is to be expected that the velocity is lower than the maximum speed. Therefore, an estimate is needed to determine the achieved velocity.

The maximum velocity that can be achieved is the free fall velocity. This velocity is given by equation 3.1. The velocity of fall is the velocity at the time of impact, subject to gravity ($v_i = t * g$), the time of impact is estimated by the height. Higher velocities than the theoretical fall velocity are not possible. At a fall height of 2.824$[m]$, the velocity can theoretically reach 7.44$[m/s]$.

$$v_i = \sqrt{2 \cdot h \cdot g} \tag{3.1}$$

To estimate the impact velocity achieved, an accelerometer is installed in the block. The accelerometers used are M353B18 piezoelectric sensors from PCB electronics. This accelerometer is used to predict the velocity in the block. The accelerometer which is used is shown in Figure 3.9. The sensor installed is a

piezoelectric sensor with a load capacity of up to $500g$. The advantage of using a piezoelectric sensor is that the sensor does not break when the measurement range of $500g$ is exceeded. The specifications of the accelerometer even state that an overload limit of $10,000g$ can be reached without the sensor breaking. The sensor can detect accelerations up to $500g$. The wedge with an angle of 15° exceeds $500g$ on impact. The accelerometer is therefore not suitable to measure the impact for both the wedge with an angle of 15° and the flat plate. Furthermore, the sensor can be used up to $10[kHz]$. The frequency range is lower than the signal of the DAQ system.

In addition to an acceleration sensor in the block, a second acceleration sensor is attached to the tank. The accelerations detected by the second sensor can be compared with the accelerations of the first and the pressure sensor. It is expected that this data can be used to identify natural frequencies in the system.

Figure 3.9: PCB piezoelectric Accelerometer installed in the upper block. The accelerometer is screwed into a plate fixed in the block.

There are two light gates installed on the tower. These are mounted on the side of the tower and register a signal when something happens between the sensor and the reflector plate on the other side. Two light gates can be used to estimate the average speed between them. By estimating the speed at one point, the resistance caused by air and friction can be quantified. By quantifying the resistance an estimation of the acceleration for the whole tower can be found. This acceleration can be used to determine the velocity.

3.2.4. Pressure sensors

As indicated in subsection 3.2.2, four pressure sensors are used. The locations of the sensors can be seen in Figure 3.10. The highest pressure is expected for the impact of a flat plate in a non aerated impact. When examining the typical impact of a flat plate, it is also expected that the pressure peak will be steep and short. From the results of Ma [24], it is expected that pressures above $20[bar]$ are not unusual. When examining the theoretical maximum pressure, which is given in equation 2.13 even higher pressures above $100[bar]$ are found. In addition to the capabilities of pressure sensors, there are also some limitations. The signal from the sensor must be extracted while the block is dropped. In practise, this means that the sensor sends the data via six-metre cables that are about twice as high as the tower. A second limitation is weight. The weight of the sensors should be as light as possible to keep the weight of the block low.

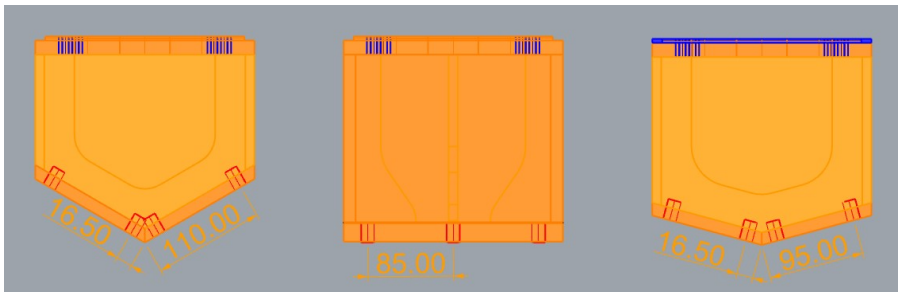

Figure 3.10: Locations of the pressure sensors on the different shapes. For the wedges the sensors are as close as possible to the nodge. For the flat plate the inside sensors are located in the middle of the plate. The outside sensors are placed as far as possible. The dimensions are given in $[mm]$.

As with accelerometers, piezoelectric pressure sensors are used. Piezoelectric sensors react quickly when

pressure peaks occur. Piezoelectric sensors measure the voltage difference due to the change in electrical potential when a material is mechanically loaded. Because of this property, piezoelectric sensors do not consist of moving or mechanical parts to register pressure. This offers the possibility of developing small sensors. The sensors used are 113B24 ICP pressure sensors from PCB Piezotronics.

These sensors are suitable for microsecond response to rapidly changing pressures. The sensors are also capable of transmitting data over long simple coaxial cables. The maximum range for a $5[volt]$ system is $68.95[bar]$. But even if the pressure exceeds the measuring range, the pressure sensors will not break until $1034.2[bar]$ is exceeded. If the pressure is below the measuring range, the sensor should operate with a sensitivity of $1.38 * 10^{-3}[bar]$. A high rise time is required to indicate the pressure peak, which can be almost instantaneous for a flat impact. The pressure rise time for the 113B24 pressure sensors is less than $1[\mu sec]$ [32].

Figure 3.11: Piezoelectric PCB pressure sensor including the clamp nut and seal ring used to install the sensors in the wedges.

Figure 3.12: Piezoelectric PCB Pressure sensor including the clamp nut and seal ring used to install the sensors in the wedges.

Figures 3.11 and 3.12 show images of the pressure sensors. The length of the sensor is $34.0[mm]$ with a diameter of $5.54[mm]$ for the tip. The sensors are installed flush on the wedge. The sensors have a noise response of approximately $0.005[volt]$ when connected to six metre cables. In addition, the sensors were supplied with a calibration certificate indicating the accuracy for each sensor.

The data provided by the sensor is processed through dedicated DAQmeasurement hardware. The National Instruments modular PXI system used receives and processes the data with the associated software. The DAQ system processes pressure data up to $100[kHz]$.

3.3 Tank

The second part of the experiment is the tank into which the block falls. The most remarkable thing about the tank is the system that allows the water in the tank to be aerated. This section explains the construction of the tank and the tower. It also describes how the aeration is generated. Finally, the aeration achieved is described and how it is measured.

3.3.1. Construction Tank and Tower

The tank and tower should allow an effect that is not hindered by undesirable effects. This is partly due to the design and partly due to the construction of the experiment.

Thick wooden panels are used for the tank. Two wooden panels of $18[mm]$ are used for the sides and the back wall, giving a total thickness of $36[mm]$. The plexiglass panel on the front of the box has a thickness of $15[mm]$. A frame made of item profiles is built around the box. These profiles are used to create a flat plate on which the tower is built. The tower consists of 4 guide rails on which the block can only move vertically. The wheels of the block are guided directly on the item profiles. Since the tower is built above the box, the profiles are too far apart, namely 36 and $25[mm]$, to guide the wheels on the sides of the block. To overcome the

difference in height, wooden strips are attached to the profiles. The tower is solid because the top is attached to the ceiling. At the top of the tower, some additional attachments are also made, e.g. an electromagnet for the release, a pulley with a line to lift the block and rings for the cables.

Besides the possibility to create aerated water, the tank has been extended with some small features. For example, two drains, one at the bottom and one at the waterline. The dimensions of the inner width, the length of the box and the height of the waterline are given in Figure 3.13. The tolerances between the front and back plates of the tank and the block that falls off are $2[mm]$. This is done to create some space so that the almost inevitable rotation of the block does not cause it to hit the wood or plexiglass. The distance between the front and rear panels is fixed by two tubes that connect the front and rear panels and restrict movement perpendicular to the panels.

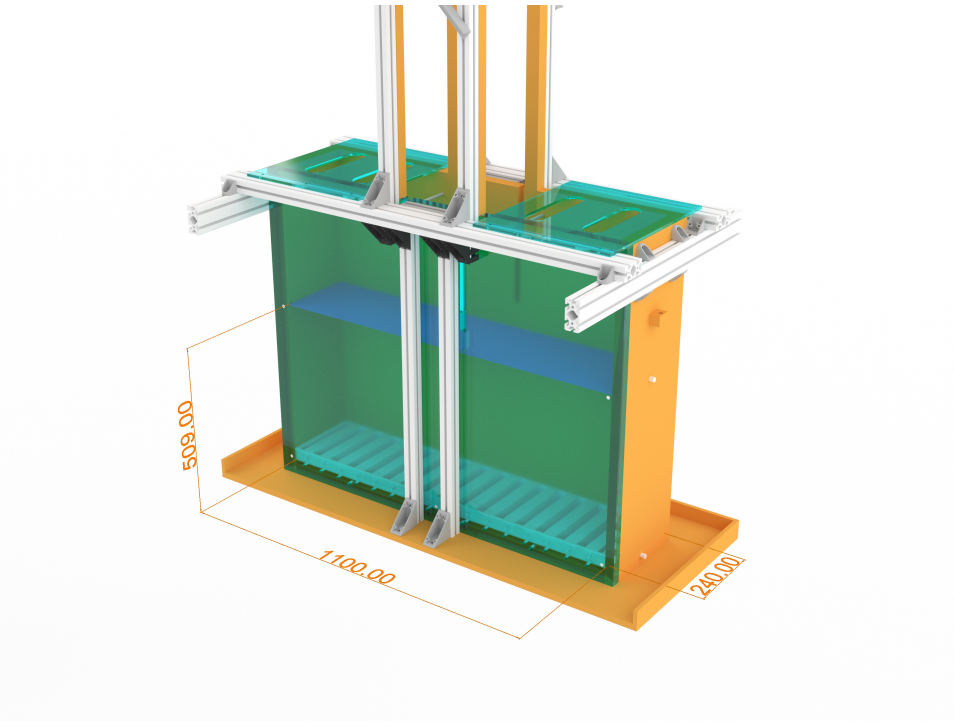

Figure 3.13: Rendering of the tank. The tank consists of three wooden panels on the sides and on the back. A plexiglass panel is attached to the front. On top of the tank next to the tower, two plexiglass panels ensure that the water does not overflow too much, but is still open for air. The tank is filled to the waterline at $50.9[cm]$. On the bottom of the tank the air diffusers are visible in white.

In Figure 3.14 there is a picture of the experiment. The block with the flat plate attached can be seen in the centre. The waterline is set at $50.9[cm]$ with the drain. Other noticeable features that are not rendered are the line attached to the side so it does not obstruct the view, the plate in front of the tank that intercepts some of the water flowing through the gaps in the top plate, and the cables hanging straight with no tension on the cables.

3.3.2. Creation of Aerated Water

The most remarkable feature of the tank is its ability to produce aerated water. This is done through the use of freshwater air diffusers, which can also be see in the illustration 3.13. The stones used are manufactured by Pentair with the model number AS23S. These bonded silica stones provide a steady flow of medium to fine air bubbles around 1 to $3[mm]$ [30].

The diffusers distribute the air evenly over the four sides. In addition to the sides, the air is also distributed over the top and a little over the bottom where the hose is attached. The aim is to create as even a layer of air as possible along the entire length. To achieve this, two measures are taken. First, the air stones are placed with some space between them. The distance between the stones results in a more uniform sheet and prevents air accumulation between or on the stones. Second, small aluminium plates are glued to the end of the stone

Figure 3.14: The set up of the experiment before the tests. (Enlarged picture can be found in appendix D)

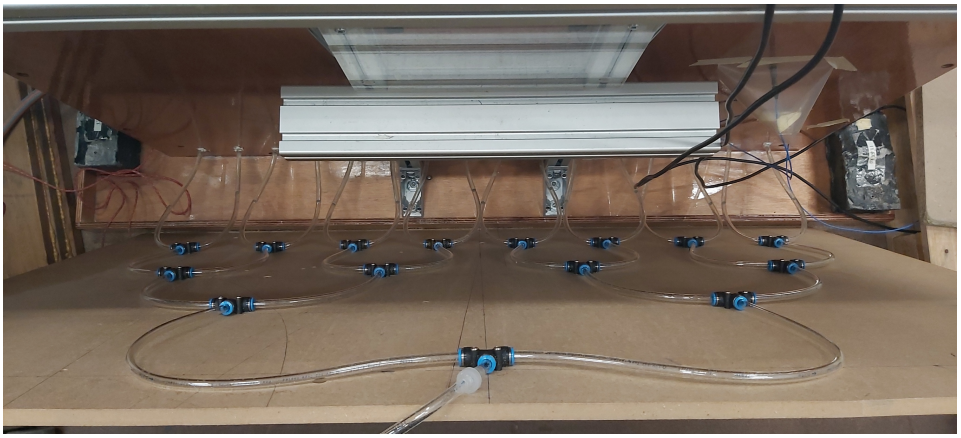

Figure 3.15: Air system behind the tank. The sixteen air diffusers are provided with a singular air source. By splitting the air at four levels, the air is divided in sixteen equivalent parts. The length of the tubes after each split is equal and the T-connectors are all placed in the same way.

and the stone itself is glued to an aluminium base plate. By gluing the stones at these points, air can no longer pass through. By restricting the air to the three sides, a more even layer is created, especially on the front and back plates of the tank.

Sixteen stones are installed on the bottom of the tank. The choice of sixteen stones is based on the fact that the stones can easily be installed with space in between. A second consideration is the fact that sixteen is to the power of two. When air is pumped into a system, the air will try to take the path of least resistance. Several considerations were made. First, the hoses between all T-connectors should be the same length. The inlet of a T-connector should always be perpendicular to the outlets so that no outlet has an advantage over the other. The air stones are connected so that the air splits into two equal directions for a few steps. By taking the power of two, a simple tree can be constructed where all paths are equal. This is also shown in Figure 3.15.

It is expected that the installation of the aeration system will create a uniform layer over the height of the tank. The maximum air flow through the system per stone is 21.24$[L/min]$, or 340.84$[L/min]$ for all sixteen stones.

3.3.3. Measuring Aeration

When air is added to the system, the diffusers blow air through the water, creating a constant stream of bubbles that provides aerated water. However, the degree of aeration cannot be determined directly from

the flow of air into the system. To measure the degree of aeration, a few methods are considered. If air is supplied to the system, it can be assumed that the aerated water is in a stable state. The amount of air entering the system is known, and since no air is created or destroyed in the system, the same amount of air leaves the system. The only unknown is the amount of air that is in the system at any given time. There are two methods of measuring aeration, both of which attempt to estimate the amount of volume in the system. For both methods, the measurement of aeration and the advantages or limitations are explained. The degree of aeration is estimated in order to have more confidence in the results obtained. In the experiment, both methods are used to measure aeration. First, a float is used to measure the aeration at the waterline. Next to the float, a tube is used to measure local aeration at three points in the water three times. Using two methods provides a higher degree of confidence in the actual aeration of the water.

Using a float

One way to measure aeration is to use a float. If air is added to the system, this volume can be added to the water volume. By determining the change in water level, the distribution between air and water volume can be estimated. The change in water level is based on the change in density given in 2.8. In equation 3.2 the conservation of mass is given. It is assumed that there is no leakage and that the change in volume due to the air over time is considered constant for a steady state. For equation 2.8 the densities of the water, air and mixture are given by ρ_w, ρ_a and ρ_{mix}. The fraction of air is given by β. The conservation of mass in equation 3.2 is denoted by the mass M, volume V and density ρ.

$$\rho_{mix} = \beta \cdot \rho_a + (1-\beta)\rho_w \tag{2.8}$$

$$\frac{dM}{dt} = \frac{d}{dt}\int \rho dV = 0 \tag{3.2}$$

In the equations 3.3 and 3.4, the mass of air added is related to a change in the waterline. It should be noted that the diffusers fill with water when no air is present. When air is added to the system, the stones first fill with air before releasing the air to the water. The volume of the air stones should be taken into account, as the volume of air does not contribute to the aeration of the water. This is taken into account in equation 3.4. In equation 3.4, the volume of a diffuser ($V_{diffuser}$) times the number of diffusers (n) is subtracted from the total volume.

$$Mass_{water} + Mass_{air} = Mass_{mixture} \tag{3.3}$$

$$\rho_{water} \cdot A \cdot h_{waterline} + \rho_{air}(A \cdot \Delta_{waterline} - n \cdot V_{diffuser}) = \rho_{mixture} \cdot A \cdot h_{mixture} \tag{3.4}$$

In Figure 3.16 the change in waterline due to the air is shown.

For the experiment, a float is used to show the rise of the water line. The float has an accuracy of $1[mm]$ due to small fluctuations that occur at higher aeration levels. To create an accurate float, a foam block is used that fits between the front and rear plates of the tank. The block is also held in place by two profiles that restrict lateral movement. By limiting the block in all horizontal directions at the waterline, only vertical movement is possible. A pointer on the block was used to read a ruler and determine the change in the waterline. In Figure 3.17 the floater can be seen. In Figure, the disturbance of the waterline due to bubbles or bubble clouds can be seen. The pointer and ruler can also be seen on top of the foam block. The red part of the pointer can be read on the ruler.

Although the float provides a simple indication of the water level after air has been added to the system, there are some drawbacks that should be addressed. First of all, not all volumes were taken into account. In retrospect, the volumes of the profiles that restrict the movement of the float and the volume of the float below the water level should be subtracted from the volume when calculating the air content. Secondly, the air diffusers are assumed to be filled with either water or air. There is no distinction between the empty

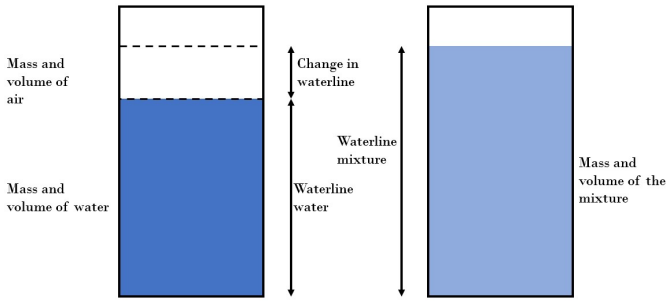

Figure 3.16: To explain the change in the water line, the left and right volumes are filled with the same amount of air and water. In the right volume, however, some of the air is mixed with the water. This results in a larger volume of mixture, while the same volume of air and water remains divided. The change in the water line is directly related to the amount of air contained in the water.

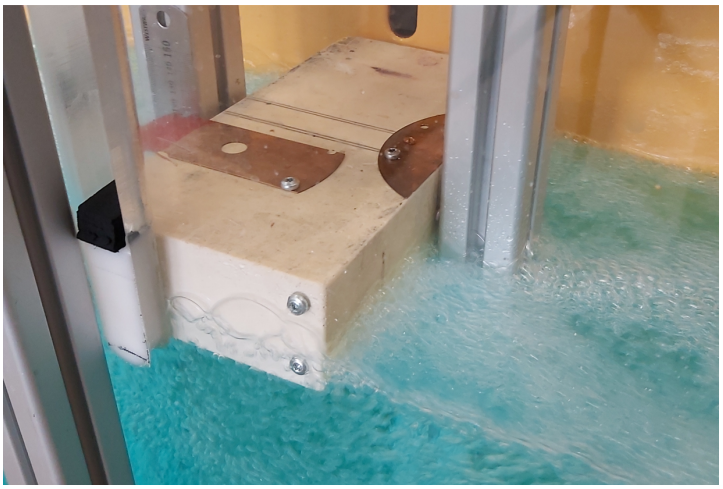

Figure 3.17: Float installed in the water. In order to clearly read the scale on the right side of the float, which can be seen in the picture behind the red indicator, the float must be restricted in its movement. If it is not confined, the float will move due to the circulation of the water. The movement is limited by the wooden back panel and the Plexiglas front panel as well as two Item profiles on the side. To allow upward and downward movement and to limit rotation, screws are attached to the foam block to guide it.

volume filling with air or water and the solid stone. For future experiments, the empty volume of the stone should be determined. Finally, the main focus in the development of the float was to create a stable surface that would not drift. To achieve this, a foam block was used across the entire width of the tank. Due to the size of the block, an upward force is to be expected from the bubbles escaping from the water, which would (slightly) influence the results.

Filling a volume

The second method used is based on the volume of the specific bubbles and the rise time. Using a known closed volume, the time needed to fill it completely with air is used to estimate the degree of aeration of the volume.

$$\beta = \frac{L_{cylinder}}{v_{bubble}} \cdot \frac{1}{t_{fill}} \cdot 100\% \tag{3.5}$$

The estimates of [29] give an insight into the velocity of a single bubble as opposed to its size. However, when there are more bubbles, the bubble-bubble interaction leads to a different velocity, for example, due to the merging of bubbles, which increases the size. In Figure 3.18, the velocities can be seen as a function of bubble diameter. It is said that the diffusers produce bubbles with diameters from 1 to 3$[mm]$. Considering

that the bubbles merge and grow, we can assume that the velocity is about 2.2$[m/s]$.

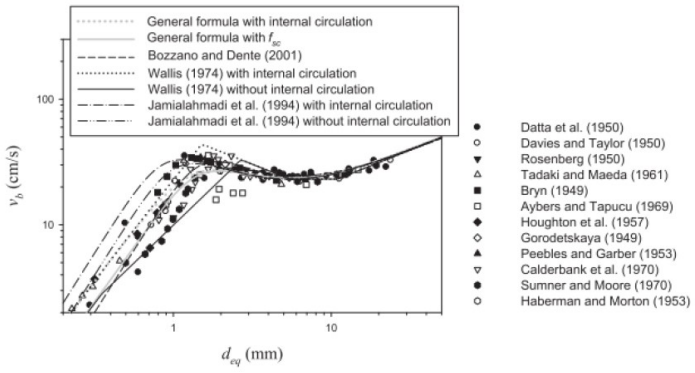

Figure 3.18: The singular bubble velocity depends on the diameter of the bubble. Various researchers have tried to estimate this relationship and the results are given here. It is found that the velocity increases when the bubble is smaller than 1.5 mm, after which it drops somewhat and stabilises. For bubbles larger than 10 mm, the velocity increases again. It is expected that the bubbles in the experiment are about 2 to 3 mm in size. [29]

To increase the accuracy of the aeration measurement, a few repetitions were made. The location of the measurement was also varied. Each time the amount of air was adjusted, three locations were tested three times. The results can be found in the table 3.1.

Table 3.1: For each form, the level of aeration is checked before the tests. This table shows the values found for each location and each test. Aeration is tested three times at three locations. The average for each location is given. Location 1 is on the right side of the tank. Locations 2 and 3 are on the right and left sides of the tower. It is expected that the measurement at location 1 lowers the average values due to boundary effects. Therefore, the average between location 2 and 3, right next to the tower, is also given to get a better estimate of the aeration.

	Flat plate			Wedge 15			Wedge 30		
	1%	2%	4%	1%	2%	4%	1%	2%	4%
Average Location 1	0.79	1.94	2.32	1.30	1.38	2.76	1.30	1.90	2.52
Average Location 2	0.82	1.87	4.12	1.46	1.93	3.81	1.30	2.05	4.05
Average Location 3	0.62	1.46	3.97	1.16	2.38	4.16	1.07	2.08	4.42
Average all Locations	0.73	1.73	3.24	1.29	1.80	3.47	1.22	2.01	3.45
Average Locations 2 and 3	0.72	1.67	4.05	1.31	2.15	3.98	1.19	2.07	4.24

The measured aeration is given in table 3.1. From table 3.1 it can be seen that the aeration values are not only different for the different locations, but also that the measured aeration varies for each deadrise angle. The table shows the average of all locations. Location 1 is the measurement location near the boundary, while locations 2 and 3 are directly adjacent to the location of the block impact. It is expected that the measurement of location 1 will be influenced by the boundary conditions, especially at higher aeration levels when the flow in the tank is greater. It is concluded that the average between positions 2 and 3 is the most reliable value for aeration. An estimate of the aeration level is used to determine the value of the results. It can be seen that the aeration is lower than the preferred aeration for the flat plate and wedge experiments with a deadrise angle of 15°. And higher for the experiment of the wedge with a deadrise angle of 30°.

3.4 Experimental Schedule

In order to carry out the experiment in an orderly manner, an experimental plan has been drawn up. The aeration levels are chosen so that the wedges and the flat plate experience different aeration effects in the different experiments. The aeration levels are chosen so that a range of aeration effects occur with the different wedges and flat plate. With a flat plate, non-linear effects occur due to the air cushion effect even with non-aerated water. For a wedge with a deadrise angle of 30°, small aeration effects occur at 0.25% due to compressibility. And for a wedge with a deadrise angle of 15°, small compressible effects of 0.058% to 2.00% occur. When the aeration increases above 2.00%, strongly non-linear effects occur.

For the wedge with a deadrise angle of 30°, the aeration level required for strong nonlinear effects is too high to be achieved with the aeration system. The flat plate will always have high non-linear effects. Therefore, the wedge with a deadrise angle of 15° is preferable when choosing aeration levels. Finally, 0%, 1%, 2% and 4% are used. Figure 2.8 shows the evolution of the Mach number for the aeration levels.

The experiments are performed five times. The experiments are repeated to ensure that the results are not a coincidence. Repeating the experiments also helps to avoid jumping to conclusions. It is expected that five repetition will lead to more confidence in the results while keeping a margin of error. This means 60 experiments are carried out.

3.5 Post Processing

Post-processing is about visualising the data in a way that shows the effects that are predominant for the experiment. Other effects such as noise should be eliminated. Post-processing the data helps to understand the data and highlight some effects. However, when processing the data after the experiment, care should be taken at each step to ensure that the visualised data is still valid.

The DAQ system has eight different channels and each channel is directly connected to a sensor. Table 3.2 shows the connected sensors and the output. For the experiment, a sampling frequency of 100$[kHz]$ was used for a duration of 10 seconds. This means that the measurement system DAQ wrote about 8 million data points for each experiment.

Table 3.2: System and sensors. Six channels have been provided for the pressure sensors and accelerometers. The light gate uses two channels, one for the Light Gate Top (LGT) and one for the Light Gate Bottom (LGB). All sensors were given about 5 volts for maximum input

Channel number	Channel name	Sensor type	Max Output	Max Output
1	Pres_1	Piezoelectric Pressure sensor	± 5 Volt	68.95 Bar
2	Pres_2	Piezoelectric Pressure sensor	± 5 Volt	68.95 Bar
3	Pres_3	Piezoelectric Pressure sensor	± 5 Volt	68.95 Bar
4	Pres_4	Piezoelectric Pressure sensor	± 5 Volt	68.95 Bar
5	Acc_1	Piezoelectric Accelerometer	± 5 Volt	500 g
6	Acc_2	Piezoelectric Accelerometer	± 5 Volt	500 g
7	LGT	Photoelectric sensor	5 Volt	on/off
8	LGB	Photoelectric sensor	5 Volt	on/off

The data retrieved from the DAQ system is examined in detail to extract the usable date. The first requirement for a successful experiment is that the dropped block passes the light sensors. Therefore, the moment when the top light barrier is triggered is stored. If the top sensor is not passed, the experiment is considered unsuccessful and the data is not used in the post-processing phase.

Figure 3.19 shows the response of the two photoelectric sensors. The lower diagram shows the combined signal together with the detection value. The moment when the wedge passes can be determined by the first signal drop of the upper sensor. When the block has passed, the signal rises again. After passing the block, the sensors register some disturbances. These are probably due to the upper gain of the block and the cables passing the sensor after the impact.

To determine whether a sensor has been passed, a detection value is used. The sensor sends a laser which is received by a reflective plate. When the sensor receives a laser, the output is about 5$[V]$. From the Figure 3.19 it can be seen that the sensor has some noise under both conditions. The detection voltage chosen is 3$[volts]$. However, any value between 4.0 and 0.1 should be sufficient.

Pressures

All data of the DAQ system are raw and consist of noise. As can be seen before, the noise in the

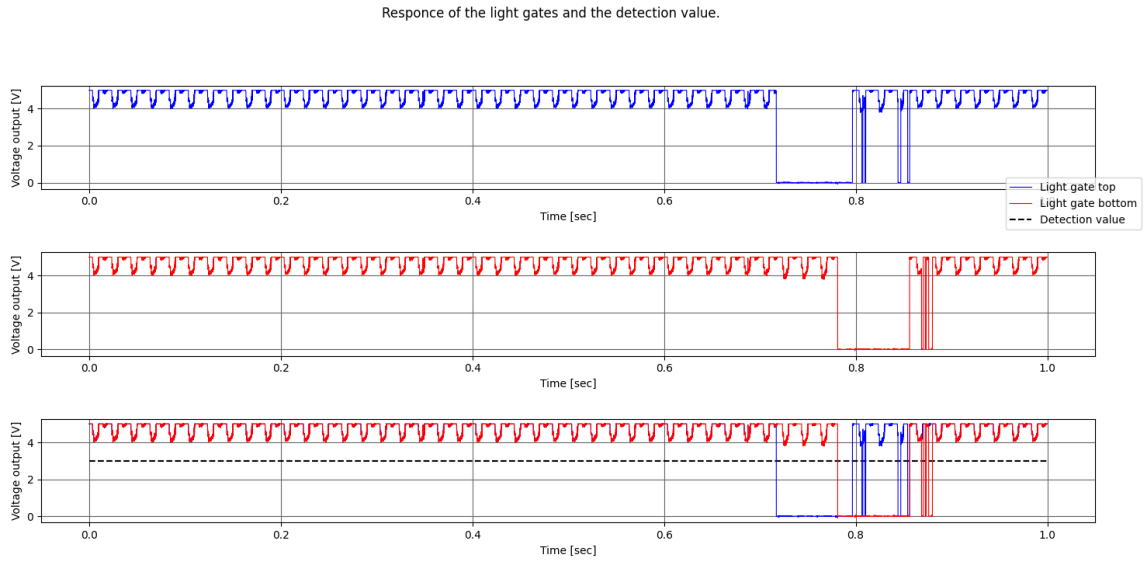

Figure 3.19: Typical photoelectric sensor response. The sensors responses when something passes if the voltage drops below 3 volt. The data shown is the first run of the flat plate impact with no aeration. The top two graphs give the upper and lower light gate. the bottom graph combines these graphs.

photoelectric sensors can easily be neglected. However, in the pressure values, the noise can affect the results. To reduce the noise, a filter is applied to the signal. A Butterworth Filter is a commonly used feature.

The butterworth filter used is a low-pass filter. By using a low-pass filter most pressure fluctuations can be eliminated. These high-frequency fluctuations can be easily detected in advance of the impact. It is assumed that the pressure change in the run-up to the impact is mainly due to the frequency of the signal. In Figure 3.22, the pressure change can be seen in the blue line.

A butterwordth filter tries to cut off all frequencies above the cut-off frequency as close to the cut-off frequency as possible, while preserving the amplitude response of the signal for the frequencies before the cut-off frequency. The decrease in frequency after the cut-off frequency depends on the order of the butterwordth filter. It should be noted that as the order increases, the complexity of the filter also increases.

$$H_{j\omega} = \frac{1}{\sqrt{1+\epsilon^2\left(\frac{\omega}{\omega_c}\right)^{2n}}} \tag{3.6}$$

Equation 3.6 shows the frequency response of a typical Butterwordt filter. ω and ω_c are the frequencies and cut-off frequency. In addition, the filter's characteristics are determined by the order (n) and the maximum passband gain (ϵ). Figure 3.6 shows the result of a butterwordth filter. Both the effect of increasing the order and the maximum passband gain can be seen. The results for a butterwordth filter of order 5^{th} can be seen in Figure 3.22 for the run before impact and in Figure 3.23 for the filtered signal after impact. The effect of a filter on the impact can also be seen in Figure 3.21. [10].

The butterwordth has one disadvantage in particular, which should be remedied. Due to its properties, a large part of the passband flatness is affected by the filter. For the filter used, this means that the cut-off frequency is greater than the maximum frequency expected in the response. This is done to reduce the influence of the filter on the magnitude of the results [10].

After a filter has been applied, the data is checked to see if it is usable at first glance. In the DAQ system there are several components and connections. In each part there may be an error that results in corrupted data and should be discarded. A simple filter to identify corrupted data is to examine the pressure rise before impact. It can be seen that for some data, the pressure rises and falls significantly before impact.

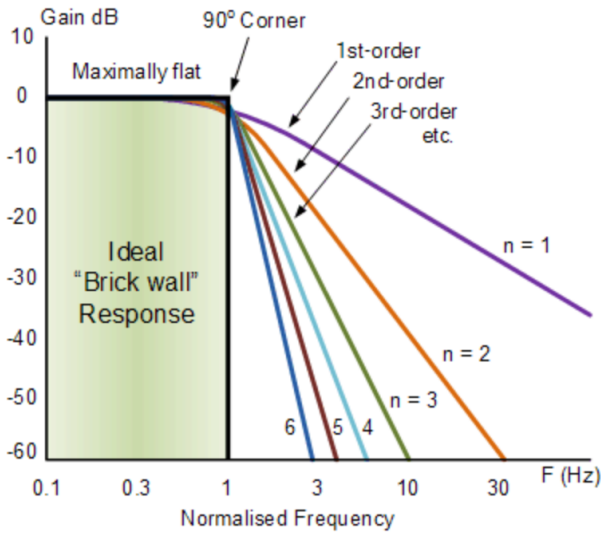

Figure 3.20: The frequency response of a Butterwordth filter together with the ideal response. Both the effect of increasing the order and the maximum pass band gain are given. Maximum pass band gain can be seen where the lines cross the cut off frequency. [10]

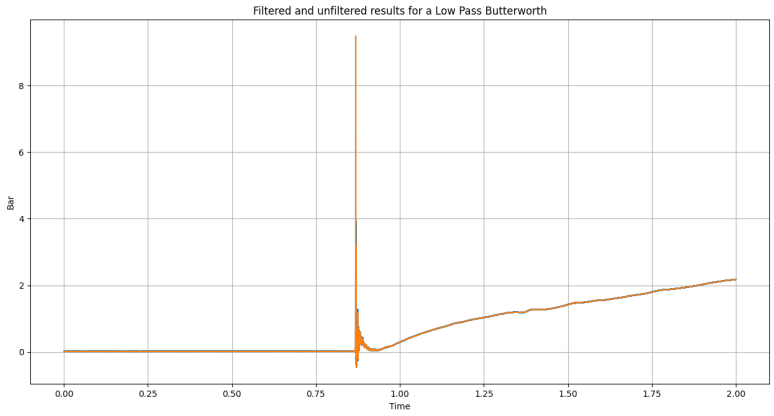

Figure 3.21: Butterwordth filter over the full experiment. Raw data in blue and filtered data in orange. The used impact is a flat plate experiment without aeration.

For all pressure sensors, the data is examined from the beginning of the experiment up to 0.8 seconds. The average pressure can be compared to the maximum and minimum pressure. If the pressure increases by more than $0.054[bar]$ in this time frame, the pressure for that specific sensor is discarded.

Unfortunately, some data is discarded because it is corrupted. However, five replicates are performed for each experiment. To improve the results, the sensors on both sides of the wedge or plate can be compared because they are at the same height. For each type of experiment, five repetitions with two sides give ten pressures for the inner and outer sensors.

When the data is checked and filtered, it can be seen that pressure sensor one resulted in biassed data in some cases. This is probably due to the fact that the sensors were not properly tightened, which led to unreliable results.

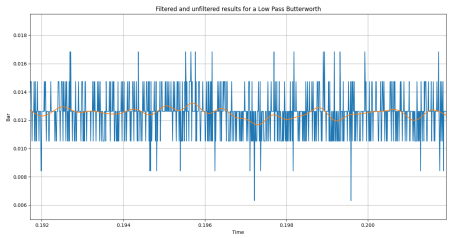

Figure 3.22: Pressure sensor data from 3.21 before impact. Raw data in blue and filtered data in orange.

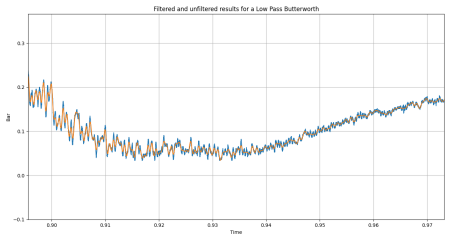

Figure 3.23: Pressure sensor data fromm 3.21 before impact. Raw data in blue and filtered data in orange.

3.5.1. Sensitivity Velocity

It is to be expected that there will be some differences in velocity between the experiments due to the inevitable friction in the tower. In addition to friction, the various wedges and the flat plate will also be subject to air resistance. Because of the shape, this will be different for each shape. It is expected that a wedge with a 30° will be the fastest. In this subsection, velocity is investigated in a number of ways. By using different methods to determine the velocity at different points, the impact velocity can be determined and verified.

Maximum Velocity

When examining an object falling from a height, the maximum velocity can be determined. If the conditions of free fall are assumed, the object is subject only to gravity. Other forces such as friction and air resistance are neglected in this case. The maximum velocity in free fall is the upper limit for the velocity. Friction and air resistance will always reduce the velocity a little.

The maximum velocity is determined by the height of fall and the gravitational constant g. This is calculated from the distance travelled, given in equation 3.7. If the equation is rewritten and distance travelled (s) is replaced with the height (h) of equations 3.7 and 3.8, the maximum velocity can be found in equation 2.1.

$$s = v_0 \cdot t + \frac{1}{2} \cdot g \cdot t^2 \tag{3.7}$$

$$v = v_0 + g \cdot t \tag{3.8}$$

$$v_{max} = \sqrt{2 \cdot h_{drop} \cdot g} \tag{2.1}$$

For a drop from a height of $2.824m$ this means the maximum impact velocity will reach $7.444[m/s]$.

Light Gates

As mentioned earlier, the gates of light are triggered when something passes. Figure 3.19 shows the response of the light gates. The first two Figures show the upper and lower light gate respectively. Both light gates clearly show the moment and time when the block and wedge or plate pass. This can be used to determine the velocity near the light gates.

To determine a velocity, the time and length must be known. In equation 3.9 the average velocity over a length is given. The time before a single sensor is triggered and the time between the triggering of the first and the second sensor are known. This means that three velocities can be estimated. Note that the average

velocity is the velocity over two points. The time at which the average velocity is determined is not entirely correct.

The first velocity can be estimated from the time between the first triggering of the two sensors. By calculating the velocity for all experiments at all three locations, the velocity for this method can be estimated.

$$v_{avg} = \frac{s}{t} \tag{3.9}$$

When the velocities between the two sensors are plotted in a box plot, a few things can be noticed. In the experiment with the flat plate and the 15° wedge, one of the experiments has a much smaller effect than the other velocities. Also, the velocities are in a much lower range than the $7.4[m/s]$ estimated by the maximum velocity.

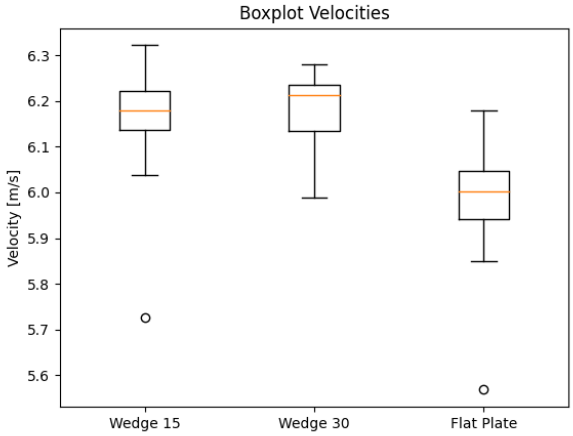

Figure 3.24: Box-plot of the velocities. Box contains the first to third quarter while the orange line gives the median. Spread is around $0.3[m/s]$ for each type of wedge, plate.

In addition to a box plot, it is also possible to display the velocities for the locations where they are registered. In Figure 3.25 the velocities for the drop height are shown. The blue line indicates the maximum achievable velocity for the respective drop height.

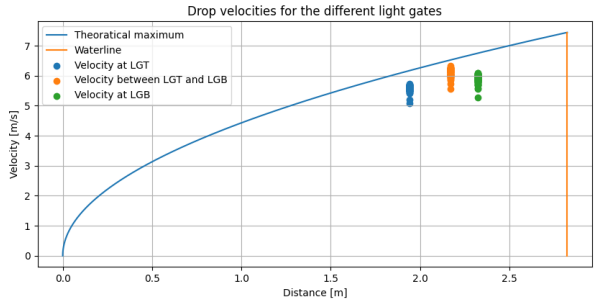

Figure 3.25: Velocities over the drop height. The Light Gate Top (LGT) and Light Gate Bottom (LGB) are shown on the location on the tower.

By Acceleration

In addition to the light barriers, the velocity can be estimated from the acceleration of the block as it falls. An accelerometer is attached to the block. By integrating the acceleration over time, the velocity can be estimated.

The acceleration is filtered with a butterwordth filter, as is the pressure. For each point, the velocity is calculated using the acceleration and the velocity of the previous point. Equation 3.10 gives the general equation for velocity. The velocity is determined by calculating the acceleration over the time step, which is added to the last velocity. In equation 3.11, the acceleration is replaced by the voltage of the sensor, the sensitivity and the gravitational constant.

$$v_i = a_i \cdot t + v_{i-1} \tag{3.10}$$

$$v_i = V_i / sens \cdot \Delta t \cdot g + v_{i-1} \tag{3.11}$$

However, if we consider the velocity as a function of time, as shown in Figures3.27 and 3.26, the velocity is lower than the expected velocity determined by the light gates. It is decided that the velocity determined by the light gates is more reliable. Nevertheless, the data obtained from the accelerometers can be used for the acceleration between the light gates and the waterline. In the Figures 3.27 and 3.26, the acceleration is constant for the first 0.4 seconds, after which it decelerates. After deceleration, the acceleration is constant again, resulting in an almost linear increase. To determine the velocity, the acceleration of the accelerometer is used together with the light gates.

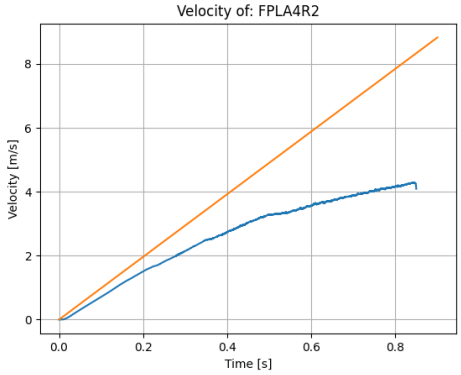

Figure 3.26: The theoretical maximum possible velocity and the data retrieved from the sensor for a flat plate.

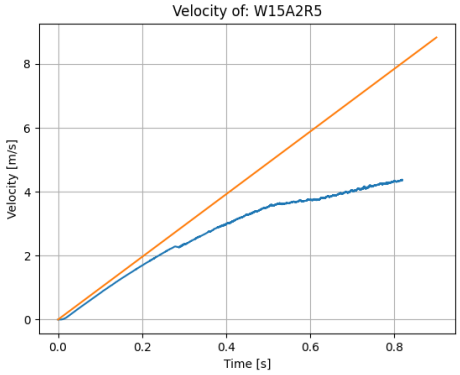

Figure 3.27: The theoretical maximum possible velocity and the data retrieved from the sensor for a wedge with a deadrise angle of 15°.

When examining Figure 3.28 it can be seen that the velocity is estimated to be $6.5[m/s]$. This corresponds to the expected loss of velocity due to friction. When examining the other accelerations, they all reach about $6.5[m/s]$.

3.5.2. Sensitivity Tower and Block

Because of the inevitable tolerances in the tower and the block, the case will not be entirely vertical. Even if the tolerances are kept to a minimum and extreme precision was taken into account in the construction of the experiment, tolerances in the range of $0.5[mm]$ to $1[mm]$ were measured. This subsection attempts to translate these tolerances into uncertainties during impact.

In Figures 3.3 to 3.8 the positions of the pressure sensors are shown. It can be seen that the sensors are in the same position across the width on both sides. The sensors are also offset in height. In Figure 3.29 the arrangement of the sensors is shown. It can be seen that the arrangement is different for the flat plate and the wedges for the inner sensors. This is because the sensors do not fit in the node due to reinforcement in the node. The distance between the sensors in height is $70[mm]$ for both the wedges and the flat plate.

In addition to the height, the width across the horizontal plane is also known. This is different for each wedge. Below are the distances between the sensors.

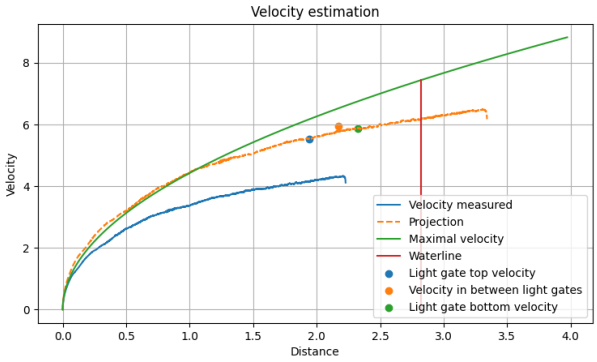

Figure 3.28: Estimated velocity by using the light gates and the accelerometers. The expected velocity by this plot is around 6.5$[m/s]$

- Distance inner sensors wedge 15° is 15.94 mm
- Distance between inner and outer sensors wedge 15° is 75.83 mm
- Distance inner sensors wedge 30° is 14.29 mm
- Distance between inner and outer sensors wedge 30° is 80.97 mm
- Distance between inner and outer sensors of the flat plate is 85 mm

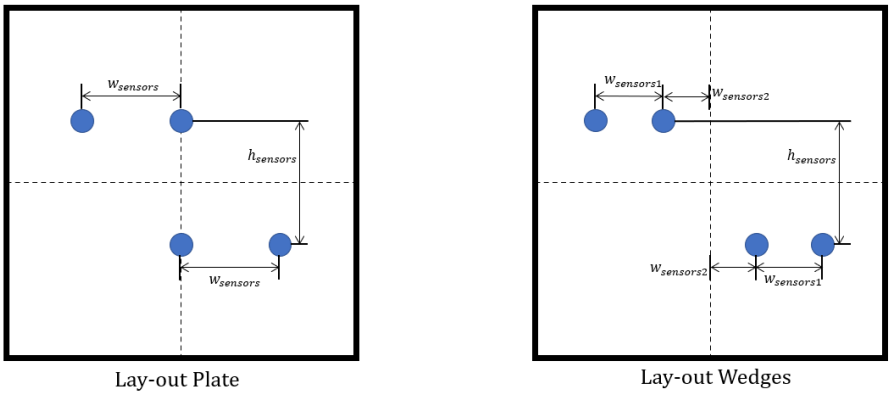

Figure 3.29: Lay-out of the sensors on the wedges and plate. The main requirement is to place the sensors as close tho the edge and nod as possible. This results in different distances for the sensors. For the flat pate the middle sensors are placed on the center-line with the outer sensors 85 mm to the edge. For the wedges the inner sensors are placed a bit of the the nod. ($w_{sensors1}$ for Wedge 15: 75.83mm, and for Wedge 30: 80.97) The distance between the sensors is also different ($w_{sensors2}$ for Wedge 15: 15.94mm, and for Wedge 30: 14.29). The distances between the sets of sensors is 70mm ($h_{sensors}$) for both wedges and plate.

The difference in the moment of impact on the wedge is used to calculate the angle. However, this is a rough estimate as the moment of impact is measured at the time of highest pressure. Some variation may result in an angle greater or less than the angle of impact. The angle at impact is given as ϕ. Two angles are assigned. The first is the angle between the sides of the wedge or plate and the second gives the angle across the height.

$$\phi = \tan^{-1}\left(\frac{\delta t \cdot v}{s}\right) \quad with \quad s = w_{sensors} \; or \; h_{sensors} \tag{3.12}$$

In equation 3.12, the angle is determined by the distance across the sensors and the distance travelled for the estimated velocity. Due to the tolerances between the wheels of the block and the tower, the

maximum possible angle would be about 0.24°. However, larger tolerances are expected in the experiment, which increase the maximum angle to about 0.72°.

For all experiments, the pressure difference between two sensors is calculated and plotted against the expected angle from equation 3.12. For height, the inner sensors are examined, and for width, the outer sensors. The data is plotted against length (red) and width (blue) in the same Figure for comparison. In addition to the colour, the shape determines whether the data can be assigned to a flat plate (square), a wedge with 30° (triangular) or a wedge with 15° (round). Looking at the Figure 3.30, it can be seen that most of the data cluster around the value zero, with no clear separation between wedges and the plate. No correlation between pressure and impact time can be derived from this. However, it can be said that the maximum angle will be around 0.5° and the pressures around 1$[bar]$.

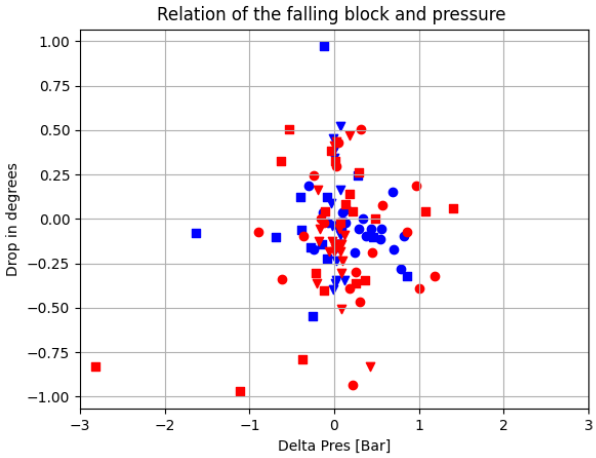

Figure 3.30: Comparison in drop angle and difference in pressure. Both over the length (red) and the width (blue). Next to the colour the shape determines if the data can be assinged to a flat plate (square), wedge with 30° (triangle) or wedge with 15° (round).

Figure 3.30 does not allow a conclusion on the relationship between angle and pressure difference, but it shows that distant points in depth should be examined. This can lead to distorted data that was not captured in earlier filters.

By examining the outliers, it is decided that the data from pressure sensor 3 is not valid for the shallow plate impact with 4% aeration. In Figure 3.30, this sensor can be seen at the leftmost point in the corner.

In post-processing the data, the sensitivity is also examined. The sensitivity of the velocity is investigated, which is related to the friction in the tower, and the sensitivity of the block and the tower, which is a relationship between the pressure shock and the tolerance between the tower and the block. By studying the sensitivities in the experiment, a better estimation of the maximum pressure can be achieved.

By post-processing the data obtained from the experiment, two things are eliminated. First, corrupted data is eliminated. If corrupted data is not eliminated, it can adversely affect the results of the experiment. Secondly, the data is filtered so that the remaining data is in the area of interest and the effects of noise are eliminated. This gives a better picture of the pressure rise, the maximum pressure and the evolution of the pressure over time.

3.6 Results

With the data sorted and examined the results of the experiment can be drawn up. The goal of this section is to show the results which can be used in chapter 5 as basis for the combined results.

In this section some notable findings are shown. However due to the large amount of data collected not all data is shown in this chapter. All data can be found in appendix D.

For the experiment more runs were done for the same type of shape and aeration. The repetitions of of the experiment should be comparable due to the same conditions in which they were executed.

In Figure 3.31 to 3.33 the experiment is shown. The results are shown for the non-aerated impact. In each corner a different sensor is shown. Although crowded, these Figures show a clear example of the differences in each run. As can be seen in Figure 3.31 and 3.32 one is clearly later than other impacts. Secondly the magnitude of the impacts is also different. However as given before in Figure 3.30 there is no clear relation between impact time and magnitude of the pressure impact.

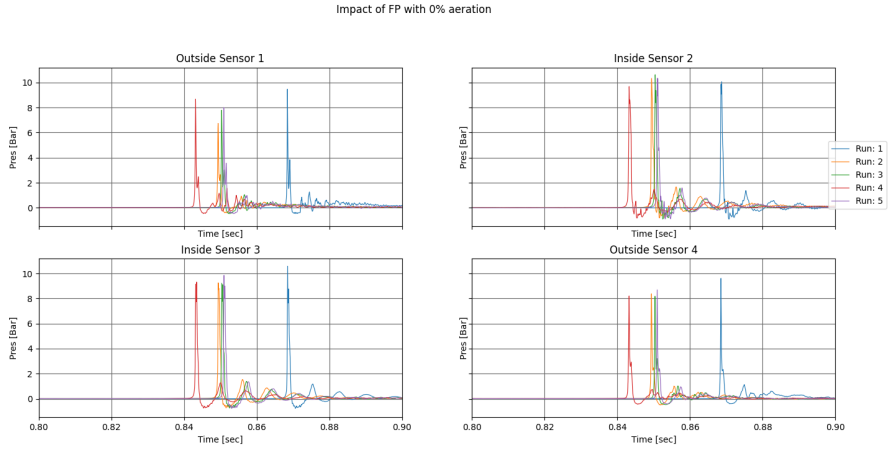

Figure 3.31: Flat plate impact for non-aerated water. Every Figure shows another sensor. In the Figures the time of impact can be seen and the magnitude of the pressure peak. Also after impact a frequency can be identified.

In Figure 3.31 the typical impact of a flat plate can be seen. It is clear that all sensors will hit the water at the same moment. Secondly the full width of the block is instantly immersed in the water. This means there is no spray along the sensor which can be seen with for instance wedge impact wedges. It is therefore that the impact is instantly for all four sensors and decreases fast. As given in section

the frequencies in the water can be identified after impact. In Figures 3.34 to 3.36 the snapshots of the impact are shown. The moment of impact shows the sharp impact. Secondly after impact the flow detaches from the side however there is no spray.

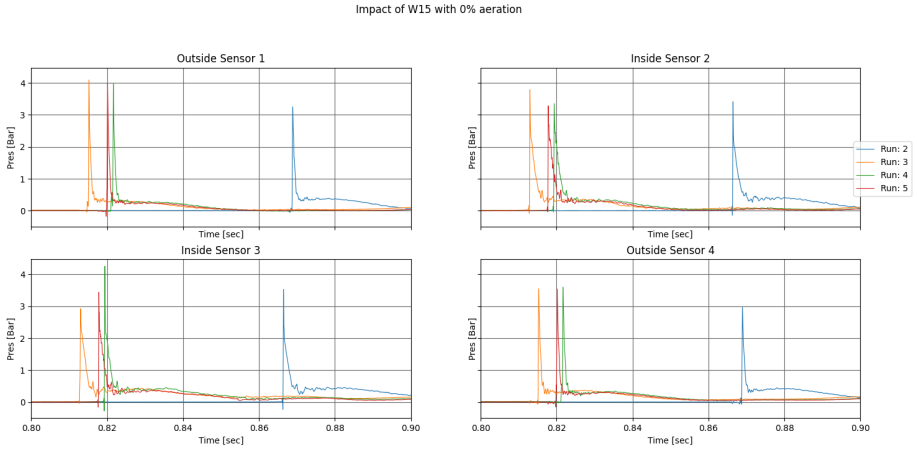

Figure 3.32: Wedge 15° impact for non-aerated water. Every Figure shows another sensor. In the Figures the time of impact can be seen and the magnitude of the pressure peak. Also after impact a frequency can be identified.

For the wedges this is different. Even the wedge with a deadrise angle of 15° has a small spray for instance. The snapshots can be seen in Figures 3.37 to 3.39. However the impact is still somewhat similar to the flat plate impact. Which can be seen in the high pressure peaks in Figure 3.32. A different impact can be seen for

the wedge with a deadrise angle of 30°. Due to the fact that there is a notable difference in height between the sensors, the inside pressure sensors will hit the water first, a spray will eject over the wedge after which the outside sensors make contact with the water. This can all be identified in Figures 3.33 and the snapshots of Figures 3.40 to 3.42. The pressure peak is nearly instant and decreases more slowly. The pressure peak for the outside sensors is lower and less instantaneous than for the inside sensors.

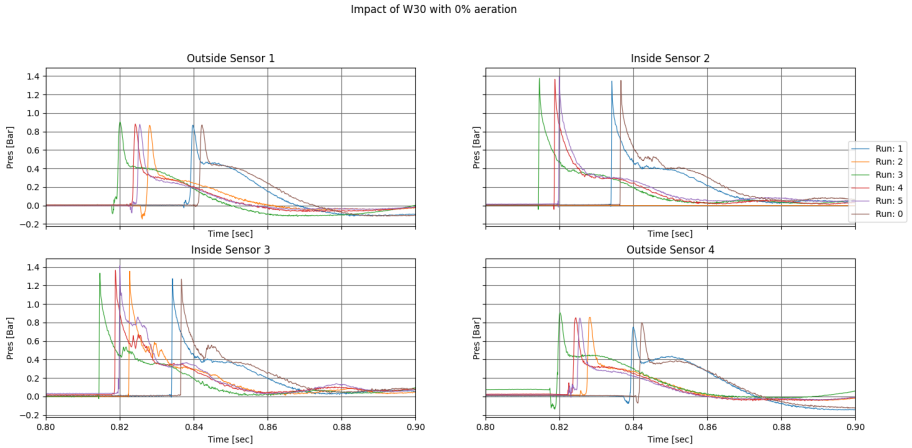

Figure 3.33: Wedge 30° impact for non-aerated water. Every Figure shows a different sensor. In the Figures the time of impact can be seen and the magnitude of the pressure peak. Also after impact a frequency can be identified.

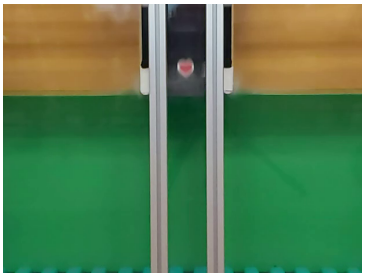

Figure 3.34: Snap shot of the flat plate impact at the moment of impact.

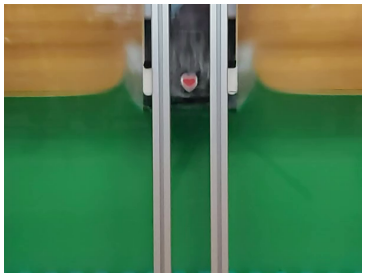

Figure 3.35: Snap shot of the flat plate impact just after impact. The flow can already be seen detached from the block at the edges.

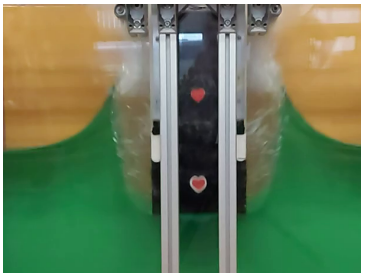

Figure 3.36: Snap shot of the flat plate impact where the flow is clearly detached. The detached flow forms a wave falling back onto the block.

When aeration is introduced the characteristics of the impact are similar. In the Figures 3.43 to 3.51 snapshots of the impact are shown for the flat plate and both wedges. The aeration for these impacts is 4%. The similarities in spray and detachment can still be seen and are similar for non aerated impact. However, a few things can be noticed. When examining the flat plate impact we can see that in one moment before impact and just after impact the bubbles in the proximity of the impact become fuzzy. This is expected to be the compressible effect of the aerated water due to the air. In appendix D an enlarged picture is enclosed in which the effect is more visible.

For the wedge impacts it is clear that spray does still exist. However it is more violent than for non aerated impact. For the wedge with 15° deadrise angle a second spray wave can be seen which moves with high speed across the waterline. In Figure 3.46 the creation of the wave can be seen and in Figure 3.47 the wave can be seen hitting the walls.

For the aerated impact the pressure sensor data is also known. In Figures 3.52, 3.53 and 3.54 the pressure data for the plate and wedges is shown.

In Figure 3.52 and 3.31 the flat plate impact is given for aerated and non aerated impact. It can be seen that when air is introduced to the system the pressure peak will be lower and more spread out. Where the impact was close to 10$[Bar]$ for non aerated impact it is closer to 4$[Bar]$ for aerated impact. This trend can

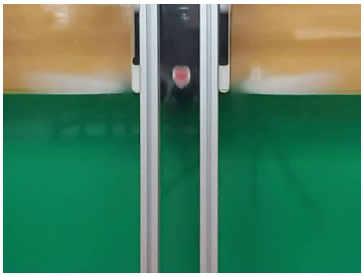

Figure 3.37: Snapshot of the Wedge with a deadrise angle of 15°. Some spray forms, however the spay is mostly horizontal.

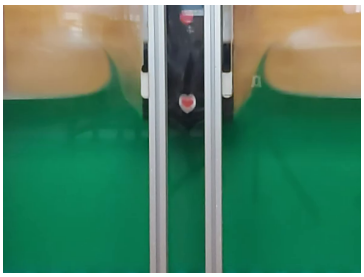

Figure 3.38: Snapshot of the Wedge with a deadrise angle of 15°. After impact the flow forms towards a more typical flat plate imact.

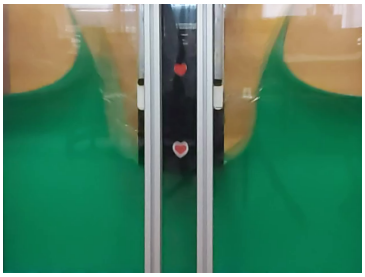

Figure 3.39: Snapshot of the Wedge with a deadrise angle of 15°. Flow fully detached, seems similar to a flat plate impact.

Figure 3.40: Snapshot of the Wedge with a deadrise angle of 30°. Spray forms around the edge. It can be seen the water rises above the nod.

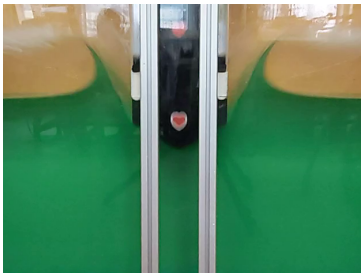

Figure 3.41: Snapshot of the Wedge with a deadrise angle of 30°. Flow is detached from the corners.

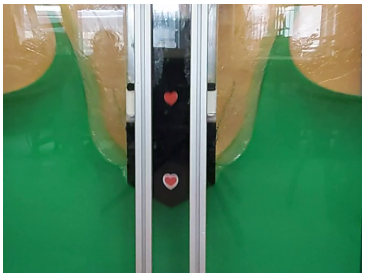

Figure 3.42: Snapshot of the Wedge with a deadrise angle of 30°. Flow is not fully detached.

also be seen for the wedge impact for the wedge with a deadrise angle of 15°. However when comparing the impact for a wedge with a deadrise angle 30° for aerated and non aerated impact, it can be seen that the magnitude of the impact is neglectable and in the range of uncertainty.

In table 3.3 the maximum pressure for all types of experiments is given. Next to the average of all experiments also the spread is given by the maximum and minimal found for the repetitions. It can be seen that the pressure decreases from 0% flat plate impact to 4% wedge 30 impact. Also the decrease in pressure for all wedges and the plate can be seen. As said before the decrease of the flat plate impact is significant larger than the decrease for the wedge 30 impact.

Table 3.3: Average maximum pressure for all experiments. Next to average, also the maximum and minimum are given. All data is in bar. The sensors compared are only the middle pressure sensors (Sensor 2 and sensor 3)

	Flat plate			Wedge 15			Wedge 30		
All data in Bar	min	average	max	min	average	max	min	average	max
0% aeration	9.217	9.925	10.622	2.924	3.497	4.251	1.269	1.349	1.414
1% aeration	6.705	6.961	7.337	2.637	3.059	4.028	1.109	1.219	1.399
2% aeration	4.522	5.253	5.707	2.08	2.522	2.989	1.063	1.18	1.269
4% aeration	0	3.682	4.421	1.772	2.283	3.3	0.884	1.125	1.306

When comparing the average for every experiment with the minimum and maximum the difference between the maximum and minimal is quite large for some experiments. Even reaching nearly one Bar for the Wedge 15 impact without aeration.

In chapter 5 these results of the experiment will be combined to an average with can be used to compare the results of the experiment with the results of the numerical simulations. The uncertainty and probable causes are known through the pressure time, velocity and impact height spread.

The maximum pressures of each run are also plotted as function of the aeration. This gives a clear visualisation of the impact pressure when the shape and level of aeration changes. This is given in Figure

Figure 3.43: Snapshot of the moment just for impact for aerated water.

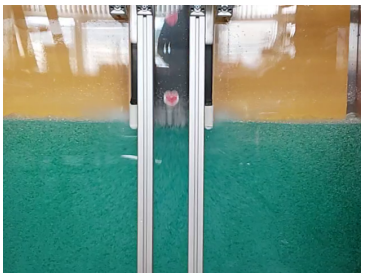

Figure 3.44: Snapshot of the moment just after impact. The spray can be seen. Also the flow can be seen compressed around the flat plate.

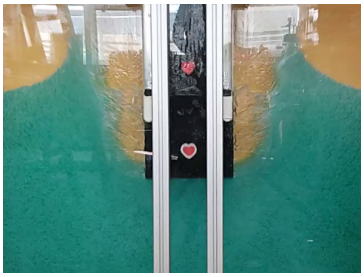

Figure 3.45: Snapshot of the plate after impact. The flow can be seen detached. A more disturbed flow can be seen between the flow and the block.

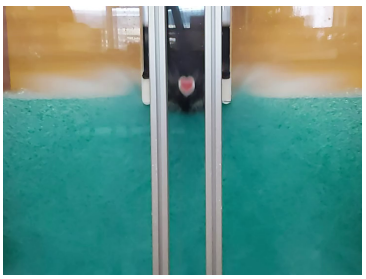

Figure 3.46: Wedge with deadrise angle of 15° just after impact. A violent spray can be seen which develops in a jet.

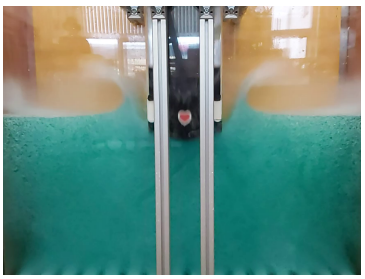

Figure 3.47: Wedge with deadrise angle of 15° after impact. The jet outwards can be identified.

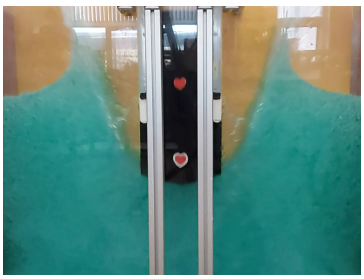

Figure 3.48: Wedge with deadrise angle of 15°. The detached flow can be seen moving outward.

3.55 and 3.56. What directly shows is the development of the impact pressure over the aeration. For a higher level of aeration the impact pressures develops closer to each other. What also shows is the effect of aeration on wedges and a plate. For the plate the impact deceases significantly more than the wedge impact.

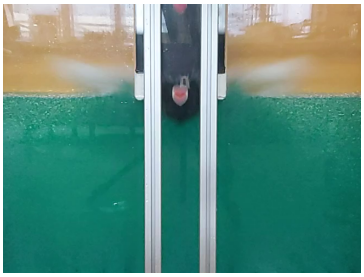

Figure 3.49: Wedge with deadrise angle of 30° just after impact the jet can be seen developing even wider than the wedge with a deadrise angel of 30°.

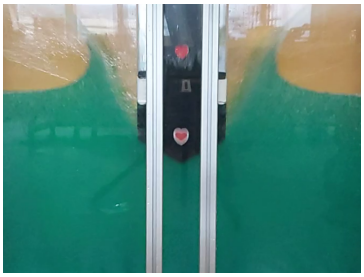

Figure 3.50: Wedge with deadrise angle of 30°. A jet forms moving outward.

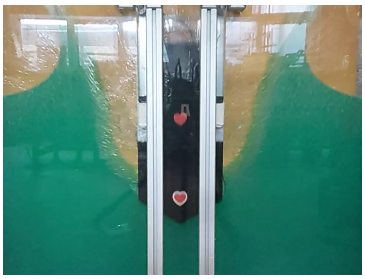

Figure 3.51: Wedge with deadrise angle of 30°. The flow can be seen detaching.

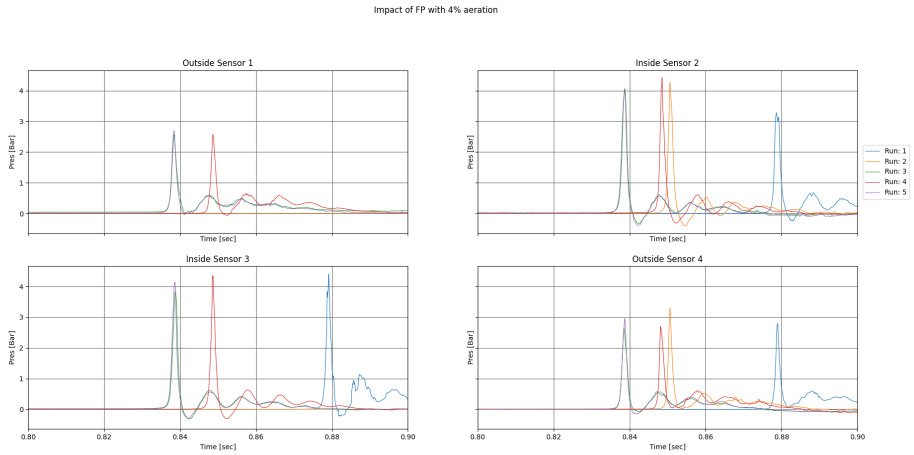

Figure 3.52: Flat Plate impact for aerated water. In the Figures a single pressure sensor is shown. The tests are done with water which was aerated with 4% air.

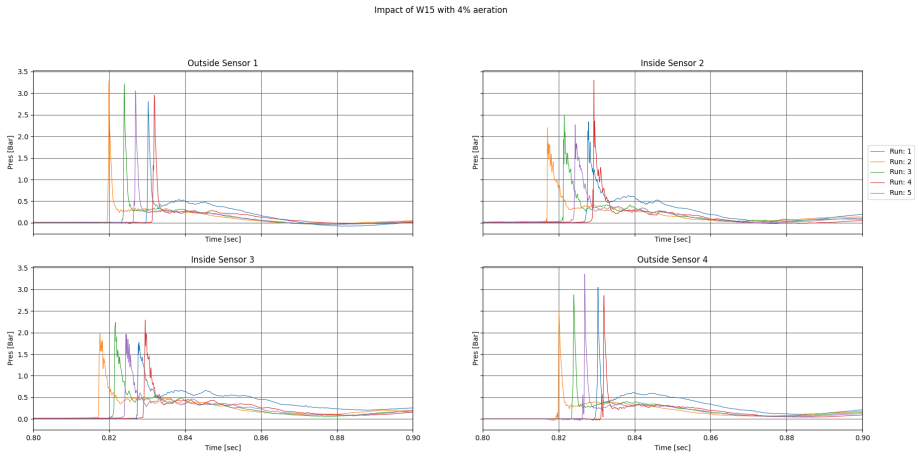

Figure 3.53: Wedge impact in aerated water with a wedge with a deadrise angle of 15°. In the Figures a single pressure sensor is shown. The tests are done with water which was aerated with 4% air.

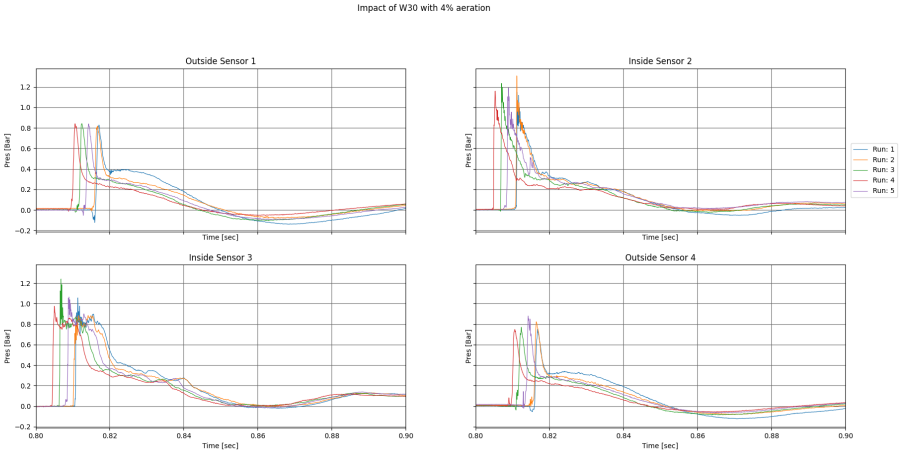

Figure 3.54: Wedge impact in aerated water with a wedge with a deadrise angle of 30°. In the Figures a single pressure sensor is shown. The tests are done with water which was aerated with 4% air.

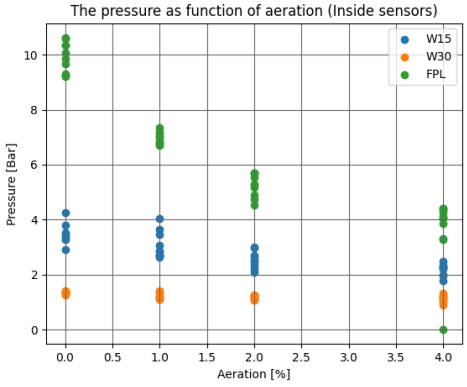

Figure 3.55: Development of the pressure over the level of aeration. Maximum pressure of the inside sensors as function of the level of air in the water.

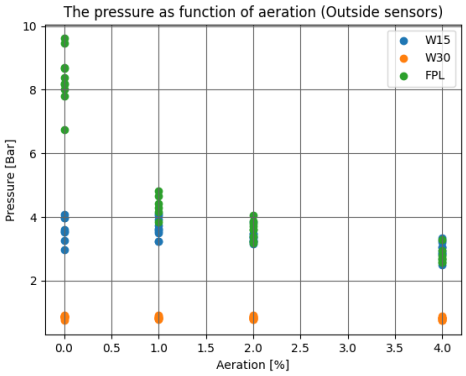

Figure 3.56: Development of the pressure over the level of aeration. Maximum pressure of the outside sensors as function of the level of air in the water.

4

Numerical Simulations

The used numerical method is a proprietary development of TU Delft. Similar to the experiment, the numerical method focuses on the simulation of a falling wedge. The pressure-based numerical solver uses the Navier-Stokes equations and the continuity equation for incompressible two-phase flows of immersible Newtonian fluids. The solver can also be used for aerated water. By using a three-phase flow model, a mixture of air and water can be simulated. If air is added to the system, the simulation can solve flows which are both compressible and viscous. The three-phase flow model can treat the fluid as a mixture air and water [25, 38].

In this chapter, the numerical simulations carried out with this software are shown. First, the numerical simulations are defined. Once these are established, the variables used for the simulations are explained. Finally, the results are given and some investigations on the errors and the grid convergence are carried out.

4.1 Set Up Numerical Simulations

Numerical simulations should be prepared in advance. Not only should all cases be evaluated, but also the grid size and input values should be considered. More inputs are needed for the numerical simulations than for the experiment.

As described in section 2, the shapes and levels of aeration are fixed for the experiment. While it is possible to change the aeration for the numerical simulations quite easily, we have chosen to keep it the same as for the experiment. The same applies to the different shapes.

In table 4.1, the initial schedule for the numerical experiments is given. A simulation is carried out for each shape and each aeration level. Later, a grid convergence study is performed to determine what grid size is required for reliable results. In table 4.1, the name of the simulations is also given. Each simulation is divided into three parts with three digits. The first part specifies the shape used, for wedges: W30 and W15 is used for the wedge with a deadrise angle of 30° and 15° respectively. The designation FPL is used for the flat plate. The second part indicates the degree of aeration in tenths of a percent. For 0%, 1%, 2% and 4%: A00, A01, A02 and A04 are used respectively.

In addition, the input conditions for the numerical simulations have remained the same. The complete input file can be found in appendix B. The area in which the experiment takes place is 1.1 x 0.9 (m), which corresponds to the dimensions of the tank in the experiment. Furthermore, the dimensions of the block correspond to the dimensions of the experiment.

The shapes are relieved about $20cm$ above the waterline with an initial velocity. This is chosen so that start-up effects do not affect the results. The somewhat high starting point of the simulation is chosen so that there are no pressure effects between the water and the sample. The sample is expected to hit the water at

Table 4.1: Schedule of the numerical simulations. The name of every simulation is divided in three parts, the first part gives the shape, the second the level of aeration and the third the grid size. The grid size is not jet determined.

	Wedge 30 degrees	Wedge 15 degrees	Flat plate
0% Aeration	W30_A00_Gxx	W15_A00_Gxx	FPl_A00_Gxx
1% Aeration	W30_A01_Gxx	W15_A01_Gxx	FPI_A01_Gxx
2% Aeration	W30_A02_Gxx	W15_A02_Gxx	FPI_A02_Gxx
4% Aeration	W30_A04_Gxx	W15_A04_Gxx	FPI_A04_Gxx

a velocity of almost $7m/s$, so the starting velocity of the simulation is $6.9m/s$. Lastly, the weight of the block used in the experiment is considered. In the experiment, the weight of the sample will be about $7.5kg$, a 3D value. For the numerical simulation, the weight per metre for all samples is $7.5kg/0.236m = 31.78kg/m$. Where $0.236m$ is the width of the tank for the experiment.

Since all objects start at the same height and have the same weight, the impact moment is the same for all objects.

The above input values can be compared with similar experimental values. However, there are also values that are typical for numerical input. First of all, the grid size. The grid size indicates the size of the cells used in the numerical simulation. One of the grid sizes used is 220x180 (for a tank size of 1.1x0.9m). This is the largest grid size and uses cells of $5mm$. For ease of identification, the number of cells across the width of the sample is used. This is shown in table 4.2.

Table 4.2: Grid dimensions of the numerical simulations.

Grid size	Dimensions tanks	Dimension cell	Width sample	Cells over sample
220 x 180	$1.1m$ x $0.9m$	$5mm$ x $5mm$	$0.218m$	41

Next, the time criteria are being discussed. The time criteria are given in table 4.3. A few time criteria can be varied in the code. For the time criteria, a optimum should be found between computation time and accuracy. The most straight forward values are the input values for the duration, the initial time step, the minimum time step and the maximum time step. These are chosen so that the calculation does not take too long, but also no time steps are used that are too large, which can lead to interesting points in the simulation being skipped.

Finally, the condition Courant-Friedrichs-Lewy (CFL) is set to 0.2. The 2D CFL conditions are given in equation 4.1. The CFL-condition is used to limit the displacement of mass per time step. If the CFL is higher, then the velocity per time step is higher than the length of the cell.

$$CFL = \frac{u_x \Delta t}{\Delta x} + \frac{u_y \Delta t}{\Delta y} \tag{4.1}$$

Table 4.3: Time dependent conditions of the numerical simulation

Duration	Initial Time-step	Minimal time-step	Maximum Time-step	CFL max
$5 * 10^{-2}$	$5 * 10^{-5}$	0.0	$2.5 * 10^{-2}$	0.2

4.1.1. Boundary Conditions

Two kinds of boundary conditions are imposed. Boundary conditions are imposed to mimic the boundary conditions of the experiment. It should be noted that these boundary conditions will not mimic a true Green Water wave. Therefore, a far-field boundary condition should be more appropriate. However, a non-penetration boundary condition ($\vec{u} \cdot \vec{n} = 0$) and a free-slip boundary condition are introduced at the walls and bottom of the domain.

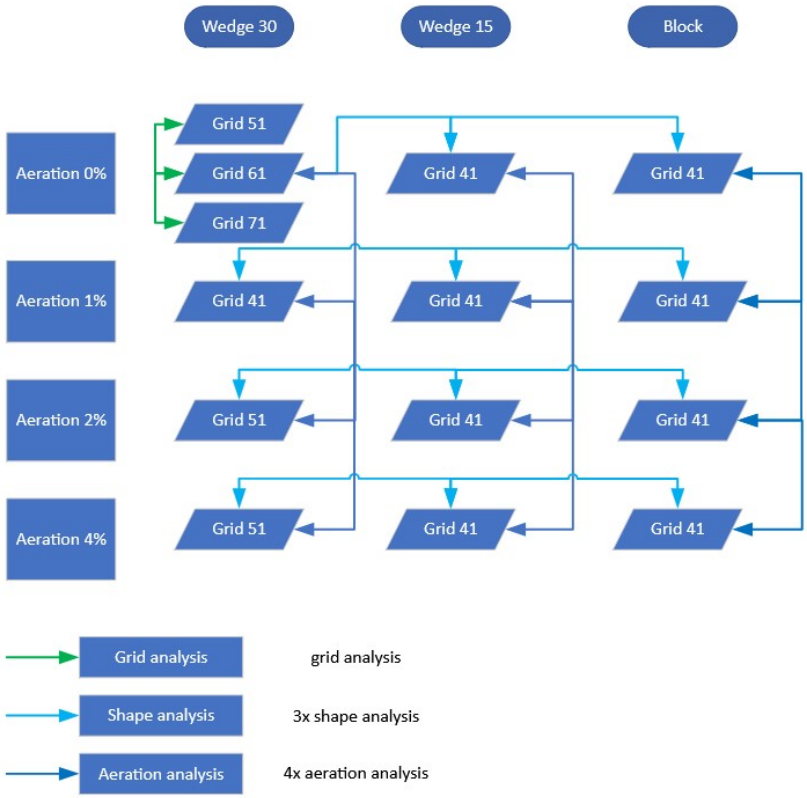

Figure 4.1: Schematic overview of the numerical simulations and the different comparisons. For every level of aeration and type of structure the number of numerical simulations can be seen. With lines the use of full comparisons are given. These give insight in the change of the shape and the influence of aeration on an impact.

4.1.2. Grid Convergence

The numerical simulation use a mesh. The mesh is based on the number of cells across the width of the wedge. The width of the wedge is $0.218m$ and is the same for all experiments. When talking about grids, the grid number is always the number of cells across the width in the horizontal direction. Initially, three grid sizes are chosen. For each increase in grid size, about 12 of cells are added across the width of the wedge.

Table 4.4: Used grid sizes and parameters. Width wedge is the number of cells over the wedge. The width and height of the tank are also given in amount of cells.

Grid [-]	Width wedge [-]	Width tank [-]	Height tank [-]
51	54.50	275	225
61	65.39	330	270
71	76.30	385	315

Increasing the size of the grid increases the computation time. However, using a larger grid size is expected to reduce the discretisation error.

To investigate the effects of grid sizes, two simulations are performed. The effect of a wedge with a deadrise angle of 30° is investigated. For this effect, the simulation is performed with the three different grid sizes. In table 4.4, the different grids are shown. The first column contains the grid labels used for the numerical simulations. The second column gives the actual number of cells across the width of the wedge. The last two columns give the number of cells across the width and height of the tank. An increased grid size is supposed to give better results.

Figure 4.2 shows the results for the pressure at the node of the wedge. It is immediately apparent that some

fluctuations can be seen in the region immediately after impact. These fluctuations decrease by 0.023sec. Before impact and after the wedge is fully submerged the maximum pressure seems converged. At the end of the wedge, the pressure fluctuations decrease and in Figure 4.2 it can be seen that the solution for the last part of the impact can be considered as converged. In Figures 4.3 and 4.4 the moment between the two can be seen.

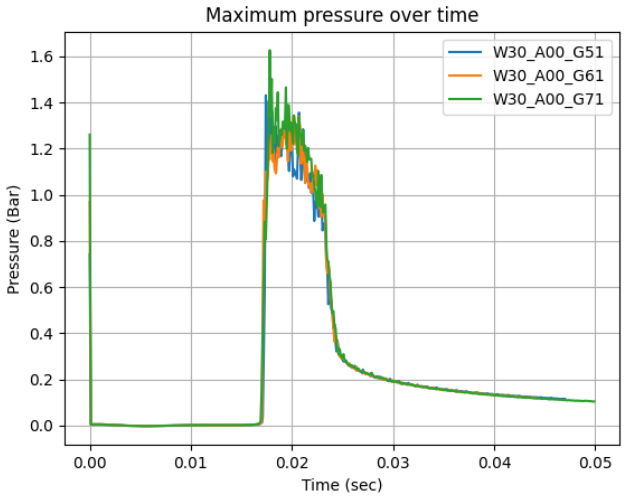

Figure 4.2: Maximum pressure for the different grids. Convergence can be seen up to the impact and after the wedge is fully submerged.

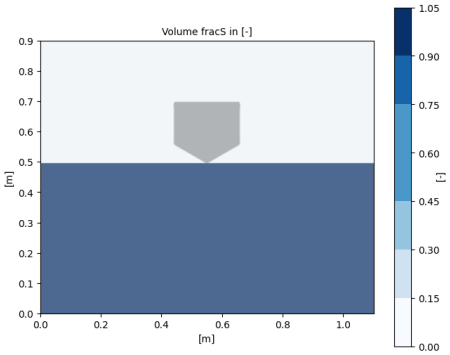

Figure 4.3: The position of the wedge at 0.01735sec.

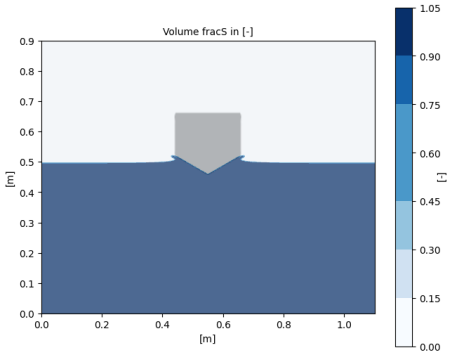

Figure 4.4: The position of the wedge at 0.02304sec.

To obtain a more reliable solution, the pressures are filtered by a kernel filter. A kernel filter examines the values around each value and changes that value according to the average of its neighbours. By filtering the results, individual value peaks are significantly reduced.

The results of the filtered peaks are shown in Figure 4.5. It can be seen that the peaks are slightly lower. However, the same trend can still be seen. In Figure 4.6 it can be seen how the pressure evolves over time between 0.0175sec and 0.02sec. A scatter plot and a line are given in the plot for the three different grid sizes. The scatter represents the numerical values found from the simulation. The line indicates the filtered values. It can be seen that filtering the pressure reduces some individual value peaks that represent unexpected low or high values. It can also be seen that filtering the pressure reduces the maximum pressure at the moment of impact. However, if the number of cells is increased, the peak value is also reduced. In Figure 4.5, the increase and decrease in pressure can be seen and the estimates converge. However, there are some convergence problems in the upper region. Immediately after the impact, pressure fluctuations can be seen. It is to be expected that these can lead to an estimate of the pressure that is not entirely trustworthy.

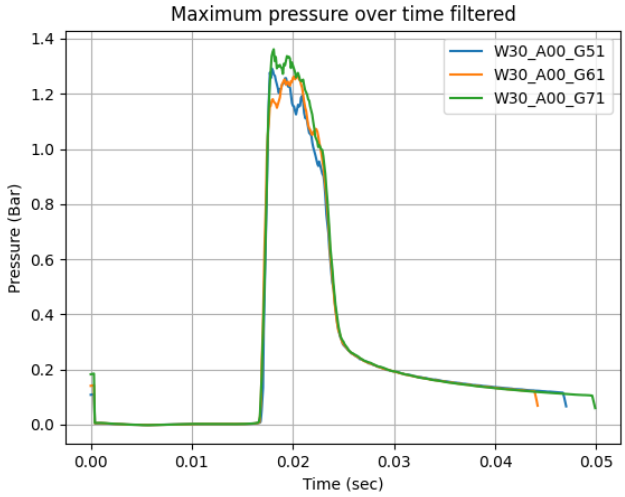

Figure 4.5: The filtered grid comparison. It can be seen that in comparison with Figure 4.2 the peaks especially just after impact are lower. While no convergence is present a trend can be identified.

With these results, it cannot be fully confirmed that the solution converges on a larger number of cells. However, it can be said with some confidence that the peak immediately after impact is an error likely due to high pressure in a single cell. It is to be expected that the filtered values, which reduce the rapid fluctuations of the pressure, will improve the result of the pressure. With this combination for no ventilated impact, a grid size of 61 should be sufficient to produce valuable results.

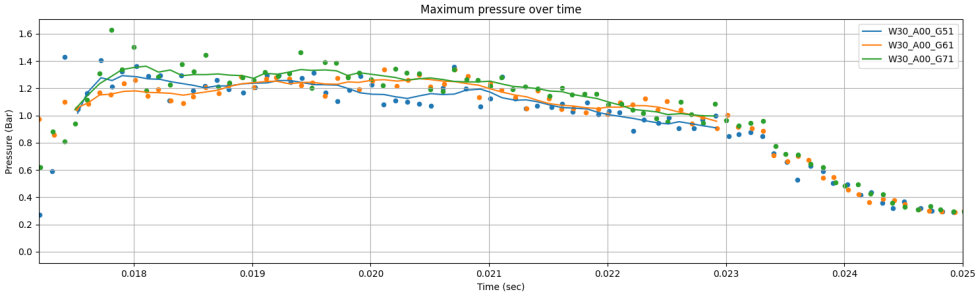

Figure 4.6: Pressure distribution after impact. It can be seen that an error exist for the maximum impact. For every grid there are still fluctuations in the pressure. In general the average pressure can be seen.

4.2 Sensitivity

Two different cases were examined to test the sensitivity of the simulations. First, the effect of changing the impact location is investigated. For two flat plate impact tests, a second simulation is performed where the starting point of the block is $1[mm]$ higher. The waterline is also $1[mm]$ higher, so that the distance between start and impact remains the same. The bottom of the tank does not matter for the impact. Both impacts should therefore be comparable. The second sensitivity study is performed to investigate the effect of small changes in the deadrise angle. For the flat plate, simulations with $0.25°$ deadrise angle and $5°$ were also performed. For the wedge with $30°$, simulations were also performed for $29°$ and $30°$. By investigating for all these cases what impact they have on the results, we can provide more confidence in the numerical results.

4.2.1. Sensitivity for different impact locations

To investigate the effects of the grid on the impact of the flat plate, two simulations are repeated with a higher waterline and a higher starting position of the block. The aim of this simulation is to determine the effects of

the position of the impact in the grid. If the block and the waterline are moved the same distance, the impact should be similar. The simulations are considered for two aerated flat plate impacts, the impact with 1% and 2% aeration.

The flat plate spans more than 60 cells in width and is completely flat. The water surface is also flat. When the plate arrives at the water surface, the air between the plate and the water surface is compressed. Because of the flat plate, which spans several cells, there is no easy way out for the air. It is to be expected that the simulation may give incorrect results. The position of the impact in relation to the cells is expected to influence the results.

In Figure 4.7 and 4.8 the maximum pressure is plotted against time. For both plots, the simulation and the simulation with an offset are shown. For the aerated impact with 2% aeration, the impact is similar and the difference could be explained by the later increase in pressure, which could be due to the cell size at the moment the plate hits the water. However, for the impact with 1% aeration, the results are significantly different. The exact pressure rise seems to be related to the location of the impact. The pressure rise for both simulations and for both simulations with offset follows a similar path.

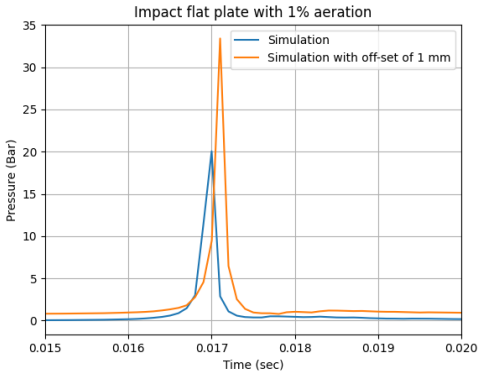

Figure 4.7: Maximum pressure for a flat plate with 1% aeration. The different lines give the initial simulation and the simulation with an off-set in the waterline and drop height of one millimetre.

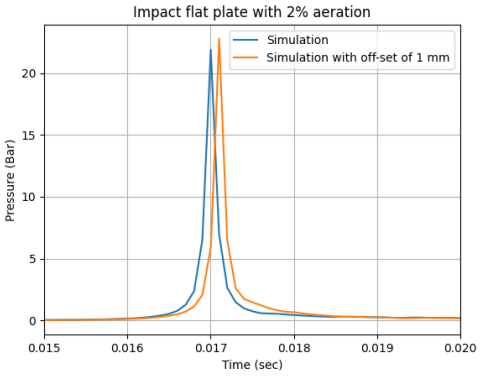

Figure 4.8: Maximum pressure for a flat plate with 2% aeration. The different lines give the initial simulation and the simulation with an off-set in the waterline and drop height of one millimetre.

To investigate the flat plate impact even further a plot with only the maximum pressure at every time-step is given in Figure 4.9 and 4.10. In these Figures the number of time steps which capture the pressure peak can be identified. It becomes clear that the peak is captured by a single point. Due to the single pressure point it is difficult to decide if this is the maximum pressure or an error exist due to some overshoot. This becomes especially clear for the impact with one percent aeration where the difference is significant. For the impact with two percent aeration it is less apparent.

It can be concluded from this that the results of the flat plate impact should be treated with caution.

4.2.2. Sensitivity in deadrise angles

In addition to the location of impact, the deadrise angle is considered for both the flat plate and the wedges with a deadrise angle of 30°. Taking into account the tolerances in the experiment, a deviation of about 0.25° at impact can be expected. The robustness of the simulation can also be tested by running similar simulations and comparing the results. In addition to the flat plate, a simulation with a wedge of 0.25° and 5° deadrise angle is performed. The wedge with a deadrise angle of 30° is compared to an impact with a deadrise angle of 29.75° and 30.25°.

Figure 4.11 and 4.12 show the cells of the flat plates and the wedges. These representations consist of all the nodes enclosing the shape. For the flat plate, it is immediately apparent that a wedge of 0.25° gives a strange shape in the corners of the wedge. Also, with a deadrise angle of 5°, the wedge appears to be more stepped than a clear wedge. From these shapes, it can be concluded that the shape should be studied when

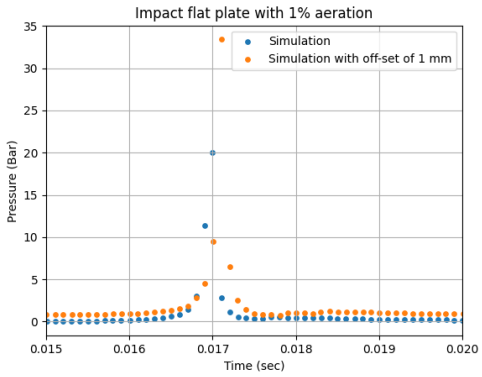

Figure 4.9: Maximum impact pressure of every time step for a flat plate impact with 1% aeration. It can be seen that the pressure peak is captured by just a few points

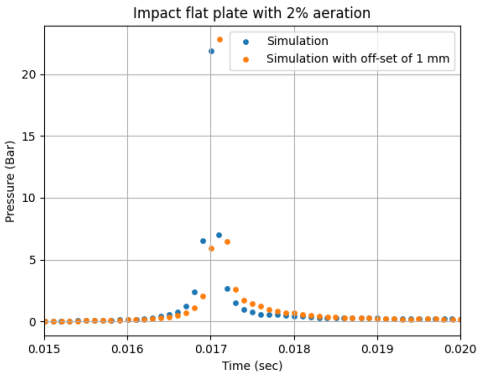

Figure 4.10: Maximum impact pressure of every time step for a flat plate impact with 2% aeration. It can be seen that the pressure peak is captured by just a few points

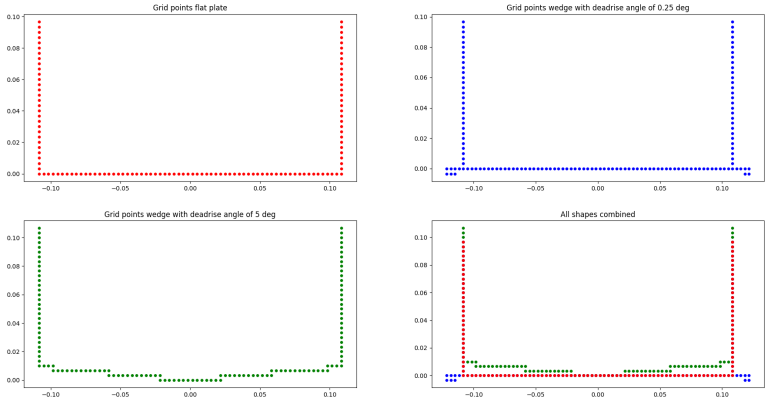

Figure 4.11: The flat plate used for the simulations alongside other shapes used to test the sensitivity in the simulations.

conducting these experiments to explore remarkable facts. For the wedges around 30° deadrise angle, it can be seen that changing the deadrise angle by 0.25° does not produce different wedges. To produce significantly different wedges for 0.25°, the grid size would also have to be significantly increased.

In the case of the flat plate, it can be seen that the different wedges give different results. In Figure 4.13 the maximum pressures for the impact can be seen. It is immediately apparent that the wedge with a deadrise angle of 0.25° produces unusual results for a flat plate impact. This is probably due to the strange arrangement of the wedge. These results highlight the importance of examining the shape before running simulations. The wedge with a deadrise angle of 5° shows a typical impact for a flat plate. However, the tents show small features that are also found in a wedge impact, such as the longer pressure decay after impact. The maximum pressure is also lower, which could be due to the wedge shape, which allows the air to escape to the side more easily compared to flat plates.

The results for the wedge impact at 30° deadrise angles are shown in Figure 4.14. It can be seen that the maximum pressure immediately after impact is slightly different, even though the wedges are comparable. It can be seen that the increase in pressure is comparable for all three wedges. After impact, the pressure fluctuates for all wedges and converges by $0.010[sec]$ only after the wedge is submerged. However, it can be seen that the pressures follow a similar trend. It is expected that by filtering the pressures a clear pressure distribution can be found. Figure 4.15 shows the filtered results. These filtered results give a clear development of the maximum pressure for the impact of the wedge.

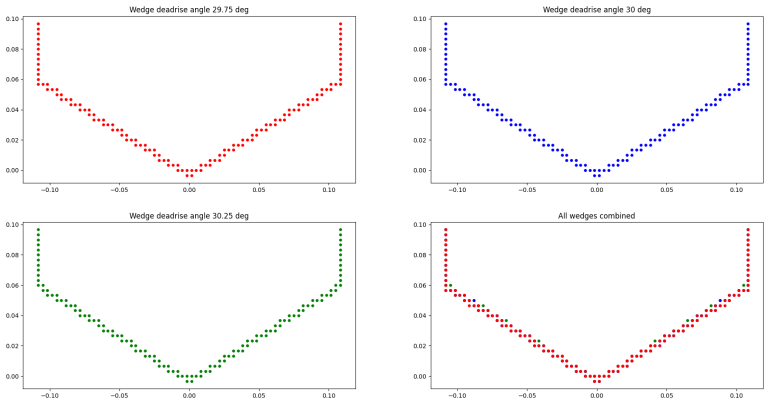

Figure 4.12: The wedge 30° alongside similar wedges with a larger and smaller deadrise angel of 0.25°. It can be seen that the change in angle is too small to create a significant different shape.

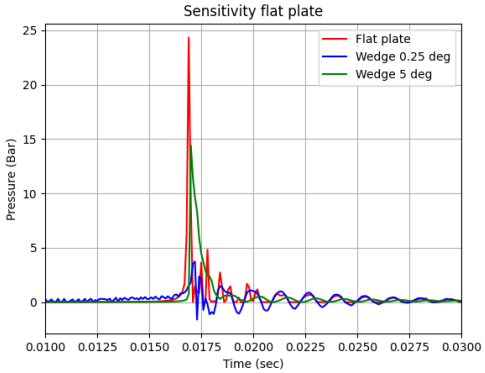

Figure 4.13: Maximum pressure of the flat plate and the wedges with deadrise angles 0.25° and 5°. The lay out of the shapes can be seen in Figure 4.11.

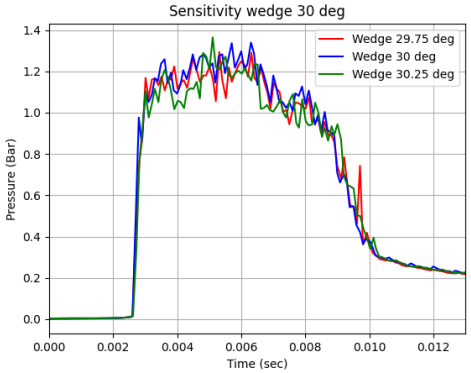

Figure 4.14: Maximum pressure for the wedge with a deadrise angle of 30° and deviations of 0.25°. Lay-out of the shapes can be seen in Figure 4.12

4.3 Results Simulations

One of the advantages of a numerical simulation is the possibility to determine the values for the pressures in each cell. Just as in the experiment, the pressure can be determined over time. However, in the simulations this can be done over the width of the wedge or plate. This pressure across the width can also be used to create a pressure distribution across the width.

Figure 4.16 shows three snapshots from the numerical simulation for a non-aerated impact with a 15° deadrise angle wedge. In these snapshots, the maximum pressure can be seen in yellow propagating across the wedge to the edges. This local pressure is around the local entrance of the wedge. This phenomenon can be seen with any shape and any degree of aeration. The pressures are given in the top row. To show the position of the wedge for each moment, the bottom row is added, combining the wedge and pressure distributions.

Figure 4.16 gives a clear overview of the pressure for these specific moments in time. However, for impact, the pressure on the wedge and the plate should be determined. In Figure 4.17 the pressure rise and fall can be seen. This graph shows the maximum pressures for each time step. The pressure rise is measured from zero to the maximum pressure for the impact. For the pressure drop, the evolution of the pressure after the maximum pressure is used. By including some moments in the simulation, the pressure across the width can be plotted over time.

In Figures 4.18 and 4.19 the pressure across the wedge is shown for different time steps. In Figure 4.17, the larger blue dots indicate the time steps used for Figures 4.18 and 4.19. In Figure 4.18 pressure rises very

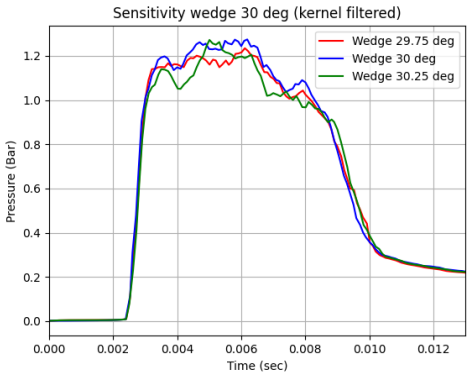

Figure 4.15: Filtered maximum pressure for the wedge with a deadrise angle of 30° and deviations of 0.25°. Lay-out of the shapes can be seen in Figure 4.12

slightly and then moves outwards. The peaks of the pressure can be seen at the local impact of the wedge. So it seems that the maximum of the pressure is not at the top of the wedge, but right next to it. With the pressure directed downwards, it can be seen that the pressure decreases and moves further outwards. This is an expected result. The pressure still moves across the wedge, which is flush with the intersection of the waterline. A similar trend can be seen for the wedge with a deadrise angle of 30°.

With a flat plate, the typical impact is different. While the waterline of a wedge changes gradually, the waterline of an impact on a flat plate changes from zero to full width in an instant. Especially in numerical simulations, where there are no small variations in the impact, the instantaneous change of the waterline leads to a different kind of impact, which can also see for example in Figure 2.17. The same Figures as for the wedge with a deadrise angle of 15° (Figures 4.17, 4.18 and 4.19) are given for a flat plate impact in Figure 4.20, 4.21 and 4.22. As can be seen in the Figure 4.20, the pressure rise and fall are steeper than for a wedge. This is due to the interaction of the entire surface with the water. The pressure is higher in the centre of the plate because air accumulates there and cannot escape as easily as with the air on the sides of the plate. From Figure 4.21 it can be seen that the pressure is somewhat parabolic and then widens to an almost flat pressure distribution. The same can be seen in Figure 4.22, which is similar to the build. However, the pressure is higher at the set-down than in the middle.

To compare the results of the numerical simulation with the results of the experiment, the pressure at the same point should be used. By using the pressure at the same location, the maximum pressure found in the experiment should match the pressure in the simulation used. Figure 4.23 shows the pressure for the locations of pressure sensors 1 and 2. The locations of the sensors are given in Figure 4.25. The pressure right at the nudge is also given. As already noted, the maximum pressure on the wedge is not exactly at the pressure point, but slightly to the side of it. By comparing the measured pressure with the maximum pressure determined in the simulation, an estimate of the maximum pressure can be determined.

With the flat plate, the maximum impact is expected to be in the middle of the plate. This can be seen in the Figure 4.21. The maximum pressure for the flat plate is expected to be found exactly in the middle. Figure 4.24 shows the pressures for the flat plate. The corresponding locations are given in Figure 4.26. In addition to the difference in height, it can be seen that the impact occurs at the same time for all sensors.

When examining the development of the pressure across the width, it becomes clear that the maximum pressure for the wedges is not at the point of the projected sensor. Nevertheless, the maximum pressure is found. This difference can be used to qualify the difference between the measured pressure and the pressure determined by the simulation. For the flat plate, the difference between the maximum pressure and the pressure at the inner sensor ($x = 0[m]$) is 0%. This is to be expected as the maximum pressure and the position of the sensor are in the same place. For the wedges, the difference between the maximum pressure at the sensor and the maximum pressure over the whole simulation is higher. For the wedge with a deadrise angle of 15°, the pressure differs by 5.38% on average at $0.016[m]$ from the centre. For the wedge with a deadrise angle of 30°, the pressure difference is on average 8.12% at $0.014[m]$ from the centre.

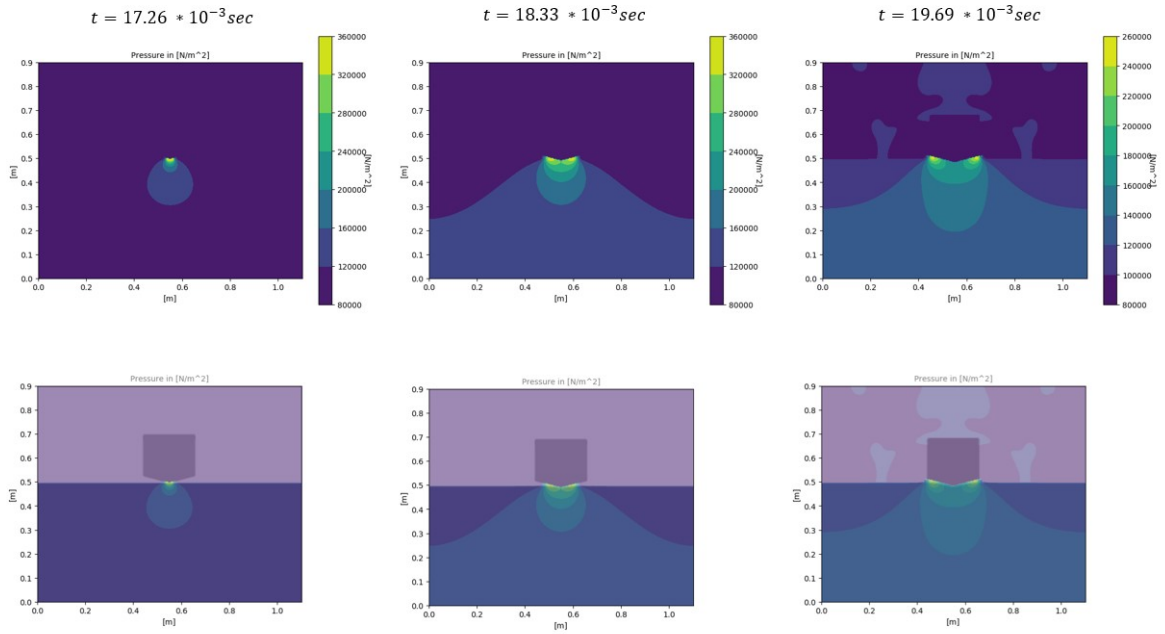

Figure 4.16: The development of the pressure over the wedge. The top row shows the pressures and how these develop over time. In the bottom row the wedge is also shown for clarification. It can be seen that the pressure travels over the wedge. In between these pressure peaks the pressure is lower. Also the start of a pressure wave through the water can be seen.

It is expected that the pressure distribution would be similar for the experiments. Therefore, the maximum effect of pressure in the experiment would be slightly higher than measured in the simulations.

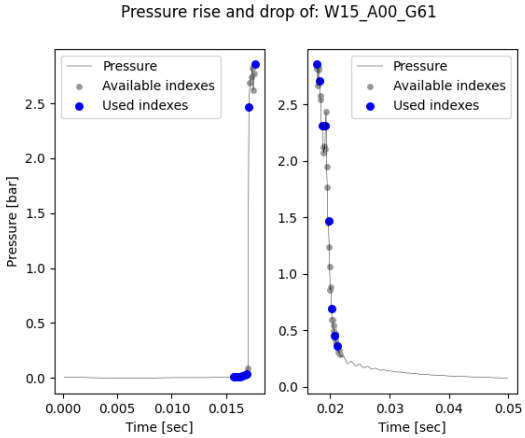

Figure 4.17: Pressure rise and drop for a wedge with a deadrise angle of 15°. In figures 4.18 and 4.19 the pressure over the wedge is given for the blue points. It can be seen that only a few time steps capture the pressure rise.

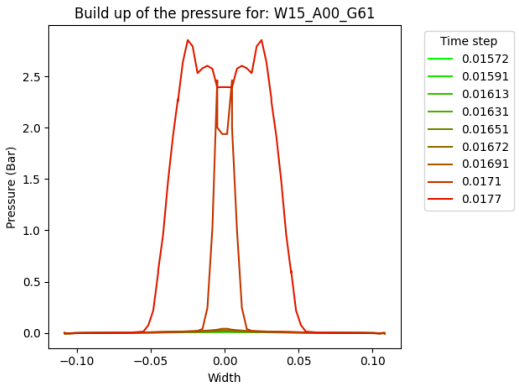

Figure 4.18: Pressure over the wedge for different time steps given in figure 4.17.

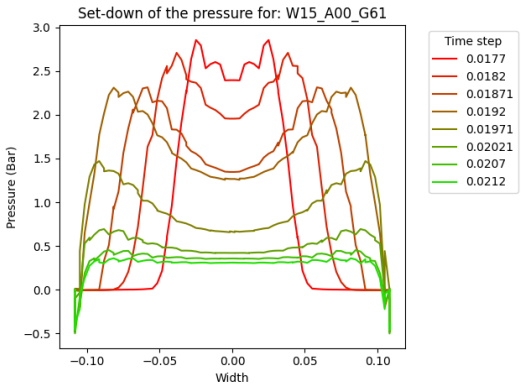

Figure 4.19: Pressure over the wedge for different time steps given in figure 4.17

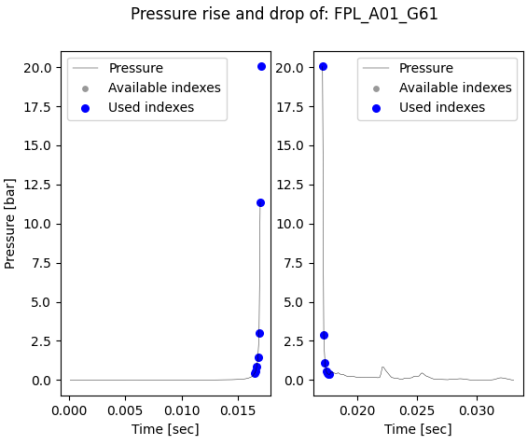

Figure 4.20: Pressure rise and drop for a wedge with a deadrise angle of 15°. In figures 4.21 and 4.22 the pressure over the wedge is given for the blue points. It can be seen that only a few time steps capture the pressure rise.

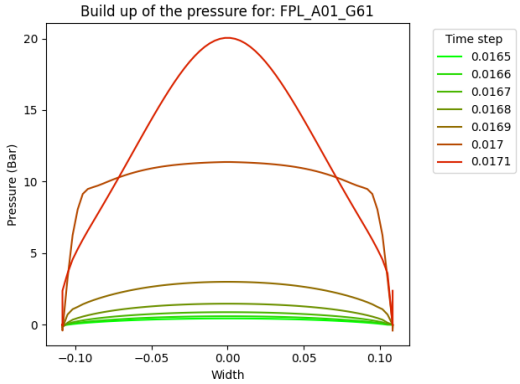

Figure 4.21: Pressure over the flat plate for different time steps given in figure 4.20

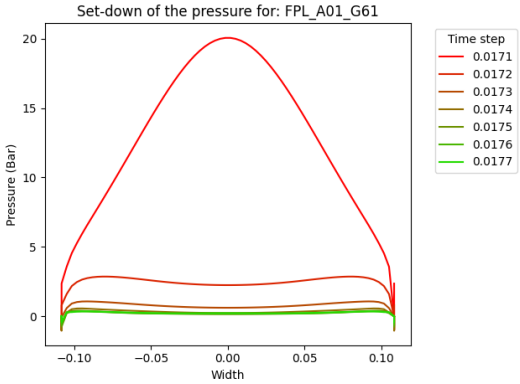

Figure 4.22: Pressure over the flat plate for different time steps given in figure 4.20

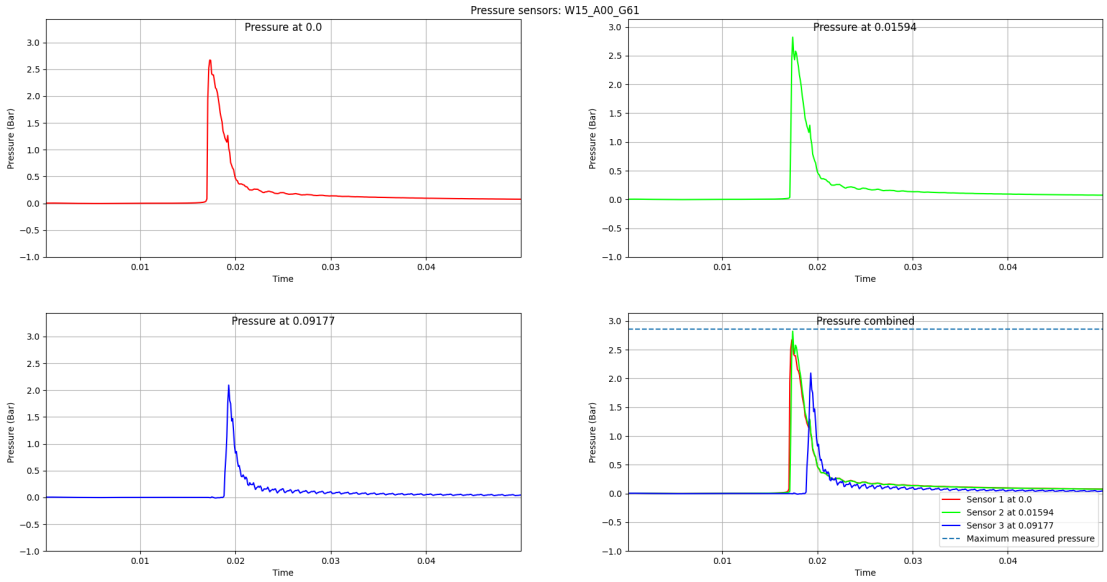

Figure 4.23: Maximum pressures for the different sensor of a wedge 15° impact. Next to the two sensors the expected pressure at the nodge is given.

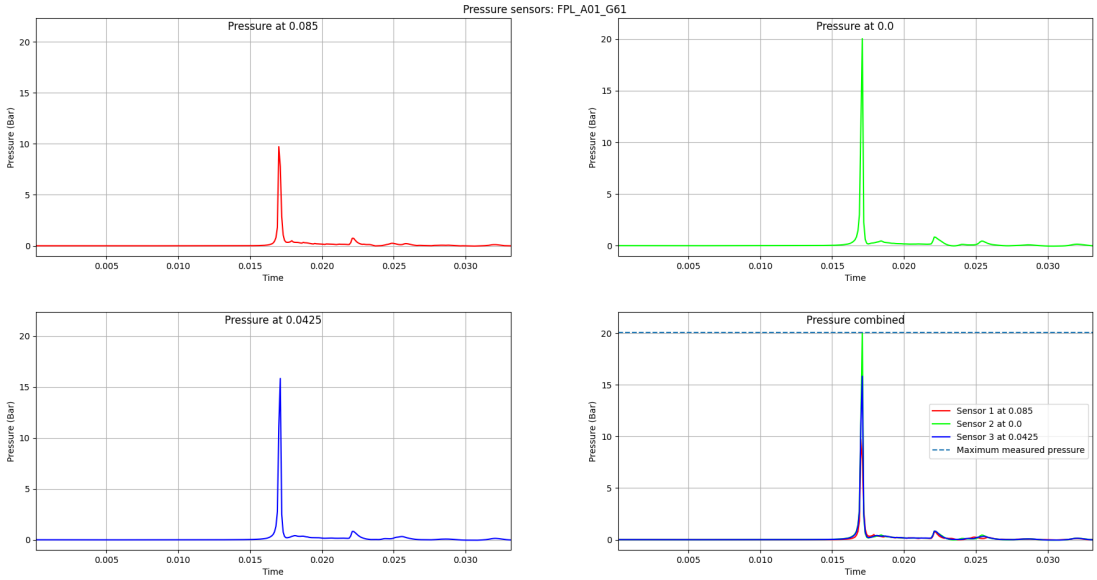

Figure 4.24: Maximum pressures for the different sensor of a flat plate impact. Next to the two sensors the expected pressure in between is also given.

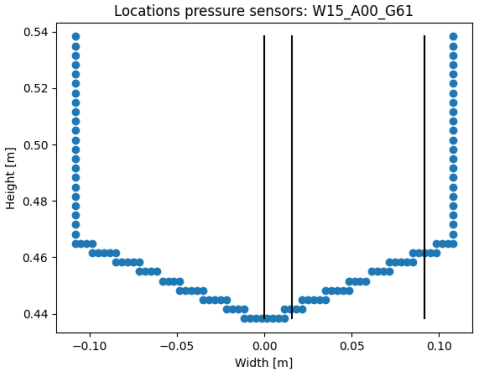

Figure 4.25: Sensor locations in the numerical simulation for a wedge with deadrise angel of 15°.

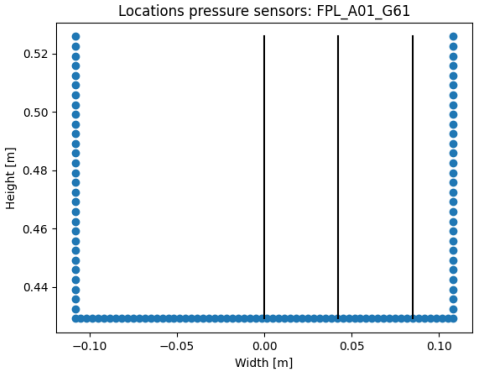

Figure 4.26: Sensor locations in the numerical simulation for a flat plate.

5

Results

The experiment and the simulations are carried out in such a way that they can be compared with each other. In this chapter, the results for both the experiment and the simulations are presented together. For the experiment, the results of the repetitions are combined to obtain an average result that is used to compare the maximum pressure of the impact with the simulation. At the end of this investigation, the results are presented in such a way that the influence of the deadrise angle and the degree of aeration on the maximum pressure can be studied. Finally, the objective of this work is presented: The maximum impact pressure when both the deadrise angle and the aeration are taken into account.

5.1 Combined Experimental results

For each experiment, repetitions are carried out. To present a result that can be compared with the simulations, the average is taken over the runs. To obtain a single result for the pressure on the inside and outside, two steps are taken. First, the impact moment should be at the same time. By shifting the pressures so that the impact moment overlaps, a better overview of the pressure is shown. Secondly, add up the pressures and divide by the number of runs. By taking the average, a pressure distribution that captures the general pressure development, which captures the characteristics of the typical pressure.

To adjust the moment of impact, the shape of the maximum pressure is adjusted to the zero point. The total time before the moment of impact is the rise and the time after is the fall. The advantage is that all pressures can be compared regardless of speed. In Figure 5.1 the pressures for the different runs can be seen and are considered similar. Just before the pressure increases, a disturbance can be seen. This could be related to the spray flowing over the wedge and the sensors. In the aerated impact, the disturbance is greater before and during the impact. This could be related to the air bubbles rising to the surface and creating a disturbed surface that is not as flat as in a non-aerated impact and therefore more disturbed.

When comparing the impacts, the impact moment of the inner sensors is used to adjust the impact moment. This is also used for the outer sensor to show the time difference between the inner sensors and the outer sensors. Secondly, the average is taken over the entire sensor data. The results can be clearly seen in the Figure 5.3.

This Figure is used to compare the numerical data with the experimental data. There are some discrepancies in the experimental results. After the comparison, these are taken into account.

5.2 Combined Results

When comparing the results of the experiment and the numerical impacts, differences become apparent. When comparing the impacts, two different sensors are recorded for both the experiment and the

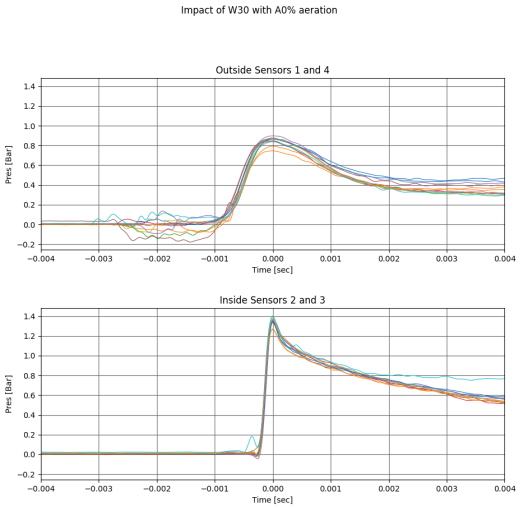

Figure 5.1: The pressures from the inside and outside sensors are shifted so that the maximum pressure is in the same place. It can be seen that there is some disturbance before the pressure rises. It can be seen that the development and maximum pressure of all runs and sides of the wedge are similar. The Figure is from an impact with a deadrise angle of 30° for a non-aerated impact.

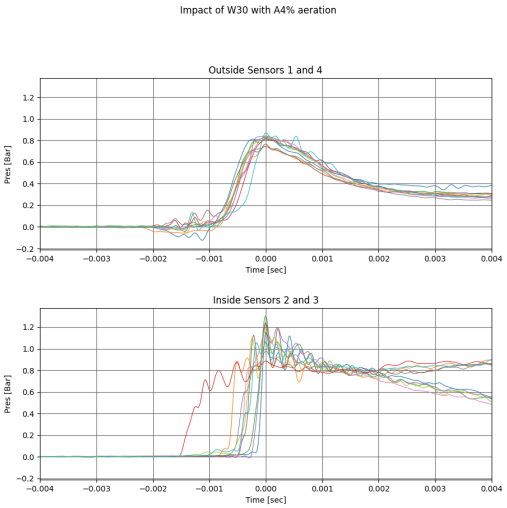

Figure 5.2: The pressures from the inside and outside sensors are shifted so that they overlap at the pressure peak. Compared to the non-ventilated impact, this impact is more disturbed and leads to fluctuations. Nevertheless, the pressure rise and the maximum pressure are comparable.

simulations. The positions of the wedges are determined by the sensors. In the numerical simulations, the pressure can be determined for each position of the wedge. However, for a better comparison, the pressure is recorded at the same locations as the pressure sensors for the wedges and the flat plate. The locations can be found in 3.10 and Figure 3.29. In Figures 5.6 to 5.9 give the combined results. For these results, the non aerated impact is given and the highest level of aeration is given around 4%.

When examining Figures 5.4 and 5.5, the pressure evolution of both the experiment and the simulation is similar for the first pressure peak. For the second pressure peak, it can be seen that the moment of impact occurs slightly earlier than in the experiment, which is due to the higher velocity of the simulation compared to the experiment. It can be seen that the magnitude of the maximum impact pressure in the simulation is somewhat low, but still acceptable.

The pressure evolution of the wedge with a deadrise angle of 15° can be seen in Figures5.6 and 5.7. Different from the wedge with a deadrise angle of 30° is the evolution of the pressure. When examining the pressure evolution for the wedge with a deadrise angle of 15°, some aspects are different. The typical pressure is more comparable to that of a flat plate for both the aerated and non-aerated impacts. However, the pressure decreases more gradually after impact than for a flat plate. Also, the difference between the maximum impact pressure is greater and for both cases.

The last thing that can be examined is the impact of the flat plate. When comparing the impacts of the flat plate, it can be seen that the differences are significant. For the non aerated impact, the maximum pressure in the simulation is more than twice as high as the maximum pressure determined in the experiment. In addition to the high pressure, the lowest pressures are also below $5[bar]$. Pressures below $-1[bar]$ are not to be expected in an impact. When the pressure drops below $-1[bar]$, cavitation occurs. In the aerated impact, the pressure rise in the simulation is even higher. It is expected that the small number of time steps in the peak leads to an overshoot of the pressure.

It can be concluded that the numerical simulations provide a reasonably valid estimate for the pressure of the wedges. For the flat plate, the results are questionable, probably due to the small number of time steps used to record the peak.

By comparing all the results, Figure 5.10 shows the evolution of the pressure for the experiment and the

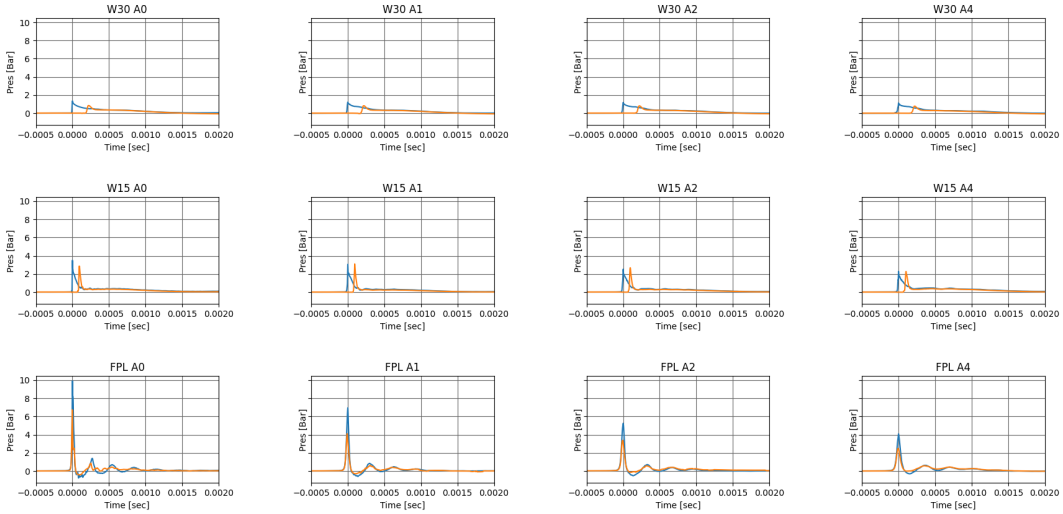

Figure 5.3: Pressure distributions over time. All axes are identical so that all sub-images can be compared. In addition to the height of the pressure peak, the time between the first and second peak can also be seen. The blue line indicates the pressures for the inner sensors, the orange line shows the pressure at the outer sensors. It can be seen that the maximum pressure occurs at the impact of a non-aerated flat plate. While a wedge with a deadrise angle of 30° caused the lowest impact.

simulations. The evolution can be seen both by the degree of aeration (for each row) and by the type of shape (for each column). The conclusions drawn above can also be seen here. The pressure development and magnitude are well comparable for the first impact on the wedges. The second impact is slightly different, which is due to the different velocities. The maximum pressures for the flat plates exceed the pressures determined in the experiment.

Figure 5.11 shows the maximum pressures for each shape and aeration. The evolution of the pressure can be seen as the shape or aeration changes. A trend can be seen. It is clear that even a 15° significantly reduces the maximum impact pressure for non-ventilated impacts. However, increasing the aeration has a greater effect on the impact and reduces it even more. It can be said that both factors have a large impact on the impact pressure.

The Figures 5.12 and 5.13 are the same as Figures 5.11 and 5.10. However, in Figures 5.12 and 5.13 the numerical data for the flat plate are omitted. By omitting the flat plate data, the overall maximum of the data is lower, which better shows the evolution of the pressures for the wedges as shown in Figure 5.12 and the difference in the maximum pressure as shown in Figure 5.13. The data show that the numerical simulations somewhat underestimate the impact. However, most of the numerical simulations are within the error range of the experiment.

The values from 5.11 are also given in the table 5.1. It can be seen that the maximum pressure decreases with increasing degree of aeration. The decrease is greatest for flat plates, while it is minimal for a wedge with a deadrise angle of 30°. The decrease with an increasing deadrise angle is greater for low aeration numbers. With a second order polynomial for all shapes, an interpolation can be made for different aeration levels.

When comparing the flat plate impact with both aerated impact and a different deadrise angel it can be seen that the effect of deadrise angel is greater than the effect of aeration. When 4% aeration is added in the system the impact decreases by nearly 59%. In contrast, when the angel is changed to 30° the impact decreases 86%. It should be noted that most of the decrease in impact is already achieved by a smaller angle or lower aeration. For the wedge with a deadrise angle of 15° the impact decreases by 65%. And the same applies to the level of aeration, 30% of the impact is decreased by only adding 1% of air in the system.

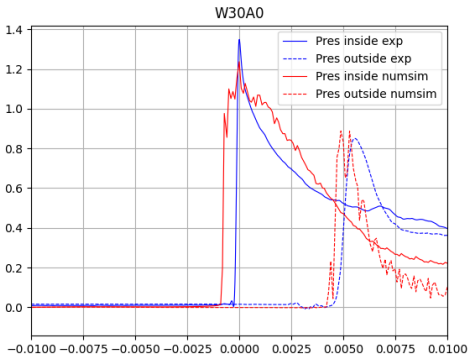

Figure 5.4: Wedge impact results for 30°. The inside and outside sensors are represented by the solid and dotted lines. The red line represents the simulations, while the blue line represents the results of the experiment. It can be seen that the simulation underestimates the pressure rise. Based on the later second peak, it is clear that the simulation overestimates the deceleration and the maximum pressure.

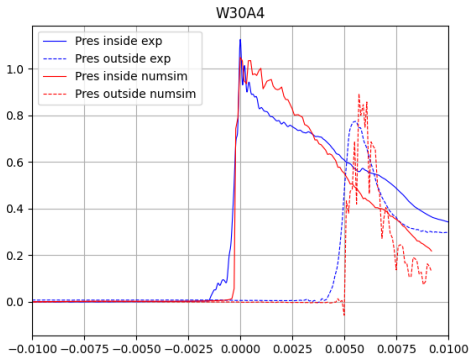

Figure 5.5: Wedge impact results for 30° with 4% aeration. The inside and outside sensors are represented by the solid and dotted lines. The red line represents the simulations, while the blue line represents the results of the experiment. It can be seen that the simulation underestimates the pressure rise. Based on the later second peak, it is clear that the simulation overestimates the deceleration and the maximum pressure.

Table 5.1: The maximum pressures for every shape and level of aeration for the experiment. The values plotted in Figure 5.11 can be found here.

	No aeration	1% aeration	2% aeration	4% aeration
Flat Plate	9.93[Bar]	6.96[Bar]	5.25[Bar]	4.09[Bar]
Wedge 15°	3.50[Bar]	3.06[Bar]	2.52[Bar]	2.28[Bar]
Wedge 30°	1.35[Bar]	1.22[Bar]	1.18[Bar]	1.13[Bar]

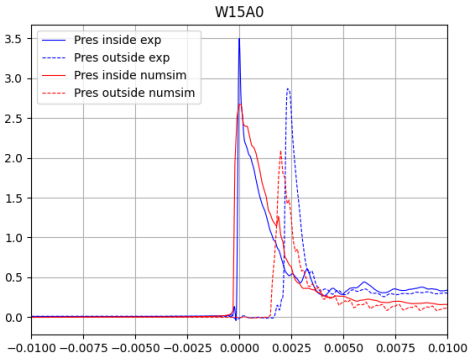

Figure 5.6: Results of the wedge impact for 15°. The inner and outer sensors are represented by the solid and dotted lines. The differences between the numerical calculation and the experiment are indicated by the colour. The red line represents the simulations, while the blue line represents the results of the experiment. It can be seen that the simulation underestimates the pressure rise and the maximum pressure. Based on the later second peak, it is clear that the simulation overestimates the deceleration.

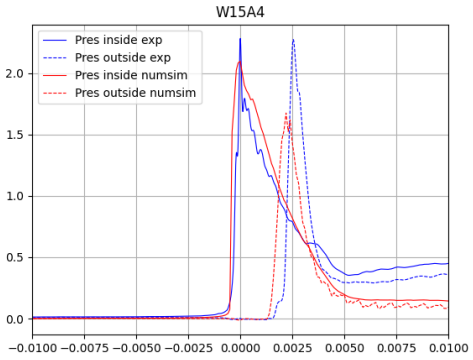

Figure 5.7: Results of the wedge impact for 15° with 4% aeration. The inner and outer sensors are represented by the solid and dotted lines. The differences between the numerical calculation and the experiment are indicated by the colour. The red line represents the simulations, while the blue line represents the results of the experiment. It can be seen that the simulation underestimates the pressure rise and the maximum pressure. Based on the later second peak, it is clear that the simulation overestimates the deceleration.

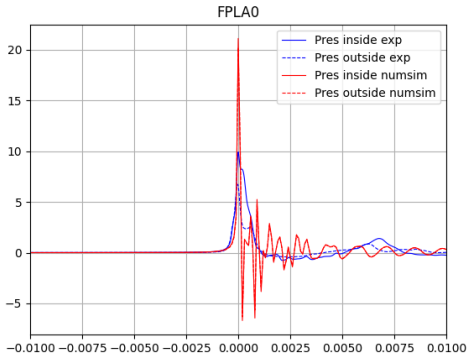

Figure 5.8: Results of an impact on a non-aerated flat plate. The inner and outer sensors are shown as solid and dotted lines. The difference between the simulation and the experiment is indicated by the colour. In the simulation, the maximum pressure is underestimated, while the pressure rise is similar. After the impact, a difference in the frequency of the pressure can be seen. It could be that this is due to the frequency of the tank.

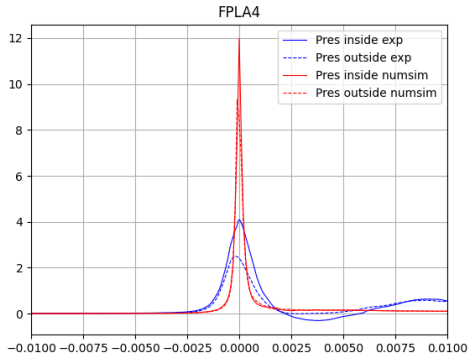

Figure 5.9: Results of an 4% aerated flat plate impact. The inner and outer sensors are shown as solid and dotted lines. The difference between the simulation and the experiment is indicated by the colour. In the simulation, the maximum pressure is underestimated, while the pressure rise is similar. After the impact, a difference in the frequency of the pressure can be seen. It could be that this is due to the frequency of the tank.

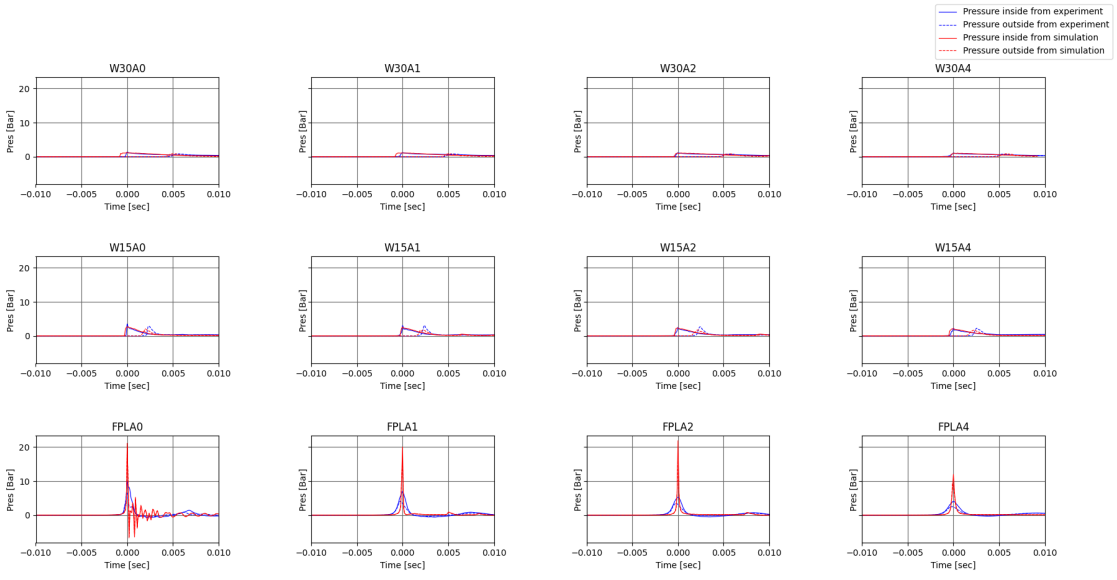

Figure 5.10: All numerical and experimental results combined. For each type of aeration and shape, the pressure on the sensors is given. In general, the pressures in the experiments and simulations are comparable. From this Figure the evolution of the pressure and the pressure increase can be seen. The maximum that can be identified are also given in the Figure 5.11.

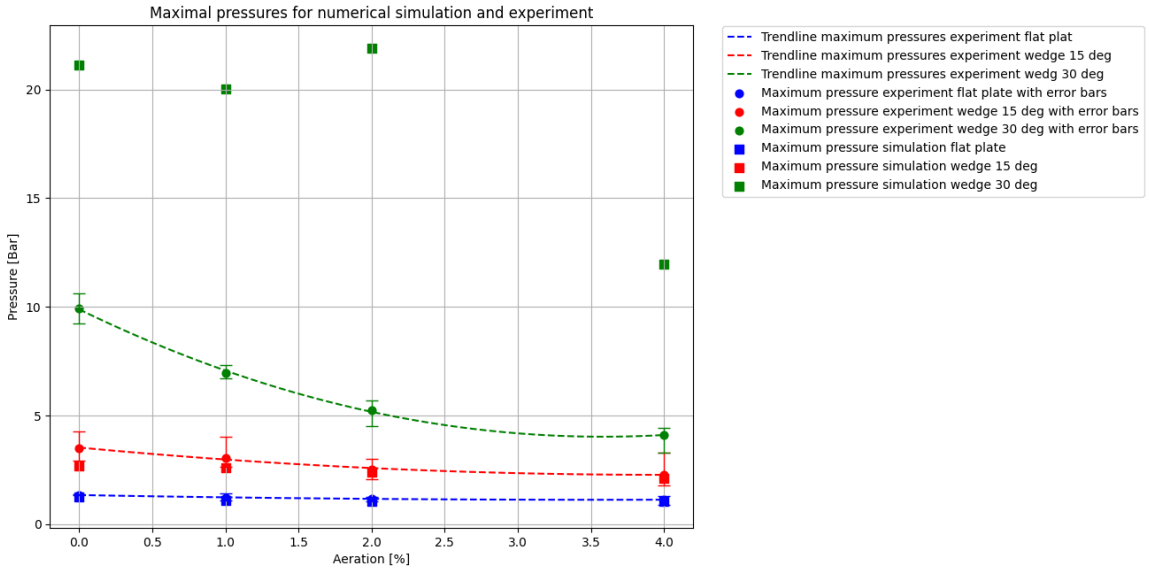

Figure 5.11: The influence of aeration and shape on the maximum impact pressure of the experimental results (round) and the numerical results (square) can be seen for the flat plate (green), wedge 30 (blue) and wedge 15 (red). The underestimation of the pressures can be seen in the Figure. However, the accuracy increases with higher deadrise angles.

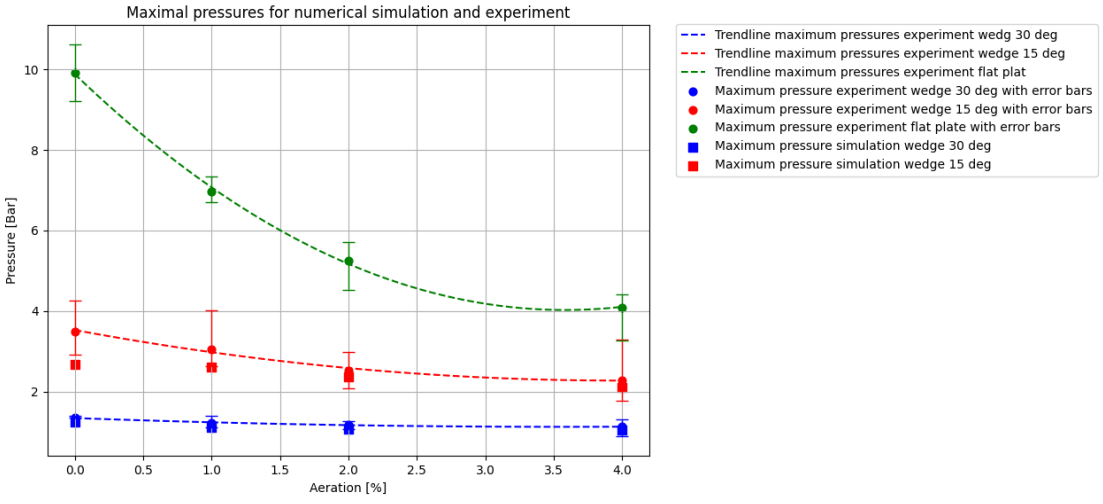

Figure 5.12: Similar Figure to Figure 5.11, only the results of the simulations for the flat plate are omitted. The influence of aeration and shape on the maximum impact pressure of the experimental results (round) and the numerical results (square) can be seen for the flat plate (green), wedge 30 (blue) and wedge 15 (red). The underestimation of the pressures can be seen in the Figure. However, the accuracy increases with higher deadrise angles.

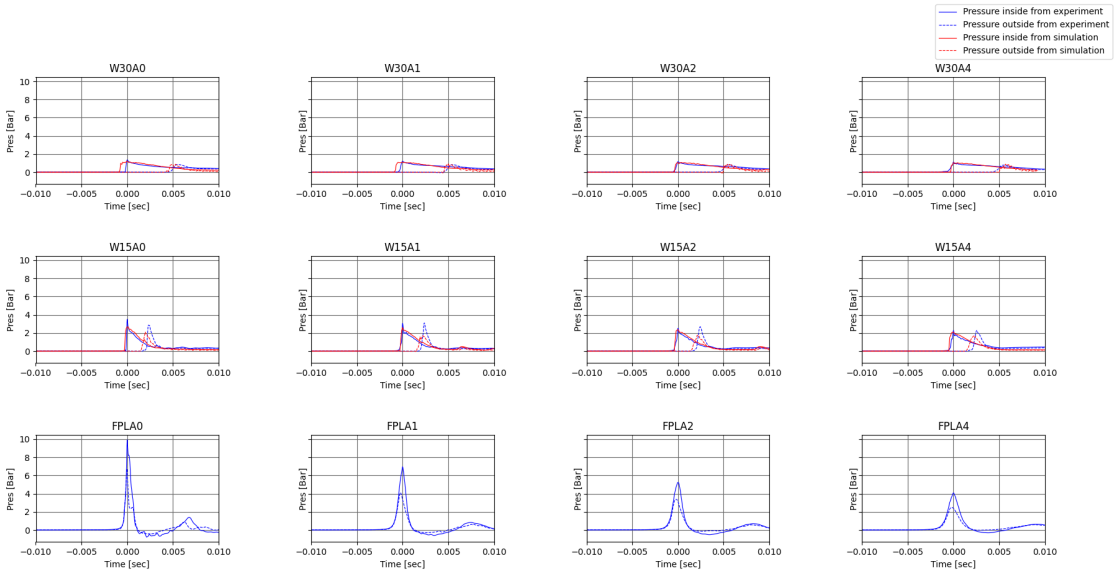

Figure 5.13: All numerical and experimental results combined. For each type of aeration and shape, the pressure on the sensors is given. In general, the pressures in the experiments and simulations are comparable. From this Figure the evolution of the pressure and the pressure increase can be seen. The maximum that can be identified are also given in the Figure 5.11.

6

Conclusion and Recommendations

After the experiment and simulations are done some final remarks can be made. This chapter will conclude the thesis and reflect on the objectives set in chapter 1.1. After the conclusion is given in the next section the recommendations for future research are given. These are split in practical recommendations which focus more on the way the experiment is constructed and the theoretical recommendations which are can lead to a better understanding of the GW impact.

6.1 Conclusion

In chapter 1.1 the objectives that lead to the aim of this thesis are given. The aim of this work is to investigate the GW impact on structures on deck by examining the maximum impact pressure when the deadrise angle and aeration of the impact are taken into account. To evaluate the maximum impact pressure a literature study on GW is done after which experiments and simulations are conducted to examine the impact. For different shapes and levels of aeration the maximum impact pressure is found and compared.

The properties of a GW wave should be examined. When the properties are not variable an estimation should be found

The first objective is to determine and examine the properties of a GW wave. When trying to determine a GW wave as a 2D problem which captures the fundamentals of the impact, the impact can be reduced to a velocity as the main input variable. This velocity is however dependant on a wide range of variables such as deck length, roughness, and shape, bow shape and type of impact (DB, PDB, HF). When a wave is arrived at deck the impact is dependant on the deadrise angle. Next the the angle of the impact the water can be assumed aerated both due to the sea state in which GW occurs and due to trapped air which occurs when the wave enters the deck. To create a fundamental GW impact the velocity is fixed on a velocity which is common for GW when travelling over a longer deck. The different levels of aeration are chosen increasingly (0%, 1%, 2%, 4%). Next to this the deadrise angles ($0°$, $15°$, $30°$) are chosen in such a way that the development of the pressure can be found and different compressible effects will take place (non-compressible, linear compressible, highly non-linear compressible effects).

A type of experiment in which water wave can be simulation should be created

The impact will be examined by an experiment and a simulation. For common GW waves, generally a DB experiment is used. However, a DB approach will not connect to the requirements which should be found by the experiment. It is therefor that a drop tower experiment will be more appropriate to test the wedge impact.

Drop impacts should be examined to achieve a first estimation of the GW impact.

By examining literature in which drop impacts are investigated, the first estimation of the maximum pressure can be found. At first the acoustic pressure is used. The acoustic pressure is dependant on the

sound of speed through a mixture, impact velocity and density of the mixture. For non-aerated impact the maximum acoustic pressure is 103[bar].

Next to the acoustic pressure different experiments are considered for both wedges and flat plate. For the wedges with 15° and 30° an experiment is found. This experiment uses the same wedges for a different velocity. For a flat plate a comparable experiment is found in both shape and velocity. To estimate the maximum pressure expected in the experiment the pressure found by Ma et al is used [24]. It is expected that the pressure will reach a maximum of 38[bar]. This value is also used to determine the range of the pressure sensors.

Construct an experiment which recreates the green water impact as close as possible

One of the objectives is to create an experiment which recreates the GW experiment as closely as possible. In chapter 3 the construction of the experiment is explained. The drop tower experiment consists of a block which can be dropped in the water. By attaching different shapes under the block the effect of the deadrise angle can be examined. The block is dropped from a height along the tower where it reaches a speed of around 6.5[m/s] where 7[m/s] was expected. The wedge or flat plate will fall on the water surface. The tank consists of different air diffusers which are able to add air to the system. This creates an aerated body of water which recreates the water in a GW wave. The velocity of the block recreates the wave front velocity.

Conduct experiments with systematically changing deadrise angles and levels of aeration

By conducting systematical tests the different deadrise angles and levels of aeration. For the twelve cases five repetitions are done. The results obtained are examined and post-processed. The corrupted data and incorrect runs are eliminated to retain usable data. The data is filtered over the time where-after it can be compared. From these results a maximum pressure is found of 9.925[bar] for a non aerated impact and a minimum pressure is found of 1.125[bar] for a deadrise angle of 30° and 4% aeration. All pressures found are in the range of ±0.429[bar].

Conduct numerical simulations which are comparable with the experiment

Next to the experiments, simulations are done. The simulations are done in such a way that they should be comparable to the experiment. However, simulations can also provide insight in the impact where an experiment lacks. For a simulation the pressure can be solved for every cell. With more than 60 cells over the width, the pressure can be visualised over the surface of the plate and wedge. This gives an insight over the development of the pressure over time. For the experiments three shapes and four levels of aeration are tested, the simulations are tested in the same way. To compare the simulations with the experiment the input conditions like velocity on impact and weight are similar.

Compare the experiments and simulations in such a way that an estimation can be made on the maximum impact pressure

Three characteristics of the impact can be found by both experiments and simulations. At first the maximum pressure can be found at the location of the pressure sensor. Secondly the time in between the impact on the first and second sensor can be found. Thirdly the development of the pressure can be seen: rise, drop and possible secondary peaks. To compare these characteristics the differences and similarities can be seen.

Provide results of the maximum pressure for impacts for different angles and levels of aeration

When examining the impact pressures the effect of both deadrise angle and aeration can be seen. The maximum impact for a non aerated flat plate impact measured is 9.93[bar] and is decreased by 8.8[bar] for a wedge impact with a deadrise angle of 30° which drops in water that is 4% aerated. The influence of both shape and aeration can be reviewed independently which leads to an reduction of impact pressure for a flat plate of 59 percent when 4% air is added to the system. When only changing the deadrise angle to 30° a reduction of 86% is found.

6.2 Recommendations

To improve the experiment and the results, a few recommendations should be made. The recommendations are divided into two types. The practical recommendations are more concerned on the construction of the experiment. The theoretical recommendations deal with the assumptions made and the measures that should be taken for more reliable results.

Practical recommendations:

- The velocity is estimated by two light barriers and an acceleration sensor. However, the accelerometer has a wide range and is less accurate at the lower accelerations. However, a smaller accelerometer can be damaged by the heavy impact. If more light barriers are installed, the speed over the tower can be better estimated. A second option is to measure the passage closer to the waterline to get a better estimate of the final velocity.
- The pressure sensors were overqualified for the required pressure. An improvement would be to use sensors with a higher sample frequency. This will increase the number of data points on the peak. More data points can give a better visualisation of the development of the pressure on the peak.
- The aeration is measured in different ways. Due to some technical difficulties, a suitable flow metre was not used. This resulted in the aeration being different in the different tests. Also, the results of the different test methods did not agree. A better estimation of the level of aeration will lead to more reliable results and eliminate some variations in the results.
- Examining the acceleration during the fall, it is clear that there is still some friction in the guidance system. Even after the impact, the block rolls over the connection between the tank and the tower. The guidance of the block to the water could still be improved.

Theoretical recommendations:

- The numerical simulation for the flat plate shows a maximum pressure much higher than the pressure found by the experiment. It is expected that the low number of data points capturing the peak result in this error. Simulations with an lower time step or combining simulations can lead to a better estimation of the pressure.
- The data for the impact will be studied. However, a better study of the peak should improve the knowledge of pressure development. When examining the development of pressure, a different filter could lead to better visualise the results.
- The velocity is fixed for all experiments and simulations and would therefore not affect the results. By investigating other velocities and weights a better understanding of the influence of these can be found.
- Further testing will improve the results. In testing, some data was disregarded due to errors in testing the sensors. More repetitions could lead to more confidence in the results. In addition to more repetitions, different forms and levels of aeration can make the results more reliable. By filling gaps that were previously only estimated.

A

Supporting Background

Supporting notes for the chapter 2.

A.1 Derivation Air in a mixture

The bulk modulus can be established for a mixture of water and air. When the volume fraction β is used for a fraction air in water. The volume aerated water (V_{aw}) is a combination of the volume water (V_w) and volume air (V_a). When equation A.1 is taken into account the volume fraction can be calculated by equation A.2

$$V_{aw} = V_a + V_w \tag{A.1}$$

$$\beta = \frac{V_a}{V_a + V_w} \tag{A.2}$$

The compressibility of a fluid is characterised by the bulk modulus of elasticity (K). The bulk modulus of elasticity is the increase (dV) of the original volume (V) by a small increase of pressure (dp).

$$K = -\frac{dp}{dV/V} \tag{A.3}$$

When using the definition for the bulk modulus (equation A.3) and equation A.1, the combined bulk modulus can be established. For the combined bulk modulus it is assumed that the bulk modulus for both the air and water are established by equation A.3.

$$\frac{1}{K_{aw}} = \frac{-1}{(V_a + V_b)} \frac{d-(V_a + V_w)}{dp} = \frac{-1}{(V_a + V_w)} \left[\frac{dV_a}{dp} + \frac{dV_w}{dp} \right] \tag{A.4}$$

$$\frac{1}{K_{aw}} = \frac{K_w V_a + K_a V_w}{K_a K_w (V_a + V_w)} = \frac{\beta}{K_a} + \frac{(1-\beta)}{K_w} \tag{A.5}$$

When examining the impact of waves the bulk modulus for water (K_w) can be regarded as constant. However both the bulk modulus for air (K_a) as the density of air (ρ) are varied with pressure due to the highly compressible properties of air. The bulk modulus of air is difficult to asses. The bulk modulus will change whether the process is adiabatic or isothermal. At an impact both processes will take place. Furthermore the values of K_{aw} can be sensitive to the volume fraction in the water. The relation between the

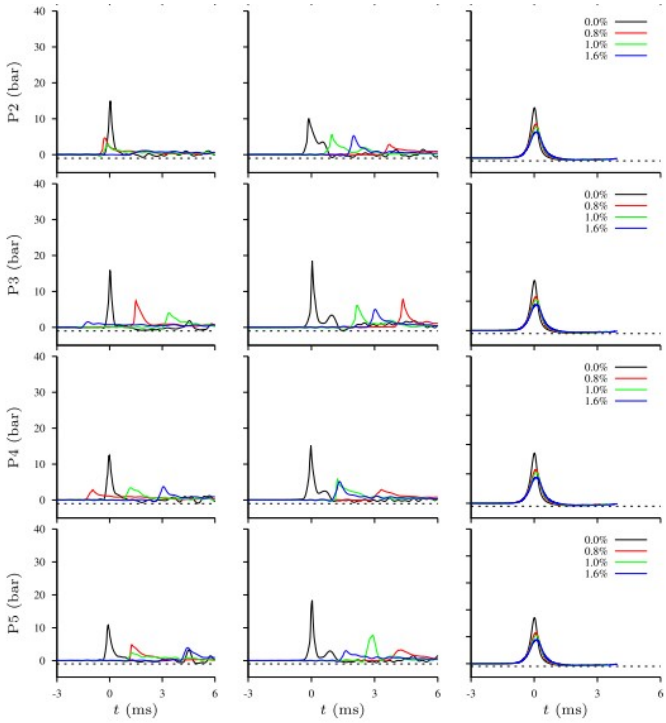

Figure A.1: Impact for the different blocks for the sensor out of the middle of plate which can be seen in figure 2.14. It can be seen that 3D effects are present. It can also be seen that aeration reduces the impact [24].

bulk modulus and volume fraction is highly non-linear. In Bullock [7] a table is provided for the expected values of the bulk modulus for different volume fractions, impact pressures and types of water.

A.2 Results Impact Aerated Impact Literature

In figure A.1 the impact of the flat plate for the pressure sensors $P2$ to $P5$ of figure 2.14 is given. Pressure sensor P1 can be found in figure 2.17.

B

Input File Numerical Simulation

The input file of the numerical simulations:

SIMULATION TYPE
Second order upwind (1) | First order upwind (0) (second-order does not work for one-phase)
0
Adam-Bashforth (1) | Forward Euler (0) (both for the convective as well as diffusive term)
0
Height function (1) | Height function original (2) | None (0)
0
Quarter-cell based (2) | Gravity-consistent interpolation (1) | Central-weighted averaging (0) (not needed for one-phase)
2
PLIC Youngs (1) | SLIC Hirt Nichols (0) | PLIC HF (2) | PLIC HF/Youngs (3) / Coeff (values/ALL = -1) (BODY AND FLUID)
1 -1
Stamping (1) | None (0)
0
Incompressible (0) | Air compressible (1) | Compressible (2) | One-phase (3) (AERATION: 2)
2
Correcting divergence term transport (2) | Correcting divergence term transport with pressure (1) | None (0) (AERATION: 1)
1
Scheme fluid flux: Macho scheme (1) | Cosmic (0) | EMFPA (2) | Unsplit (3)
2
No-slip at wall (-1) | Free-slip (1)
1
Weighted (1) | Baraldi (0)
0
Labelling Kleefsman (1) | Labelling alternative (0) (Recommended in case of using Body (Same labelling))
0
SE velocities constant extrapolation (1) | divergence free (0)
1
Conservative (1) (CFL < 0.5) | Non-conservative (0)
1
Scheme body flux: Macho scheme (1) (only when same labelling) | Cosmic (0) (only when same labelling) | EMFPA (2) | Unsplit (3)
3
Body coupling: [none (0), 1way (1), 2way (2)] | Time integration of force: [BEuler (0), Crank Nicolson (1)]

2 1
Curvature based on 5x5 (1) | 3x3 (0)
0
Cell merging: yes(1) no(0) | Value
1 0.03
Angle body [deg] (0 works)
90.0
Filter sharp corners: yes (1) no (0) | size of filter (default = 8)
0 0

C

Discussion Thickness and Structure Flat Plate

For the flat plate impact a wooden plate with 1 mm carbon on both sides to reinforce the structure is used. In this appendix the substantiation is given for this choice.

The flat plate is examined as a 2D beam with an effective length of half the width. This is a quite save assumption because the plate should be better considered as a plate fixed in four sides. As impact pressure 50 Bar is chosen. These conditions are chosen to be on the save side of the impact.

For the maximum force the formulas of Roark are used [39]. For the the maximum pressure is the maximum pressure time 0.5 of the width.

With the shear stress of different types of wood the minimal thickness can be determined with equation C.1. The plate should be thicker than the minimal thickness to withstand the impact.

$$t_{min} = \sqrt{\frac{0.3078 \cdot P_{max} \cdot b^2}{\sigma_{wood}}} \tag{C.1}$$

Next to the minimal thickness another factor is important. For a numerical simulation the flat plate will not deform. While deflection will change the impact in some way. To create an impact as flat as possible the deflection is examined for the different impacts. The deflection (y_{max}) also also calculated with one of Roarks formulas for a fixed plate. And given in equation C.2. In figure C.1 the deflection is given for the different types of wood. Next to the deflection (solid lines) the minimal thickness is given (dotted lines) which is a first condition for the plate thickness. Next to the deflection the 0.1% deflection over the width and height of the plate is given. The goal is to reach this condition provided that the weight will not increase significant. From figure C.1 it can be established that all types of hardwood will suffice if the thickness is higher than 2.25 cm. However, the weight should also be considered.

$$y_{max} = \frac{\alpha \cdot P_{max} \cdot b^4}{E \cdot t_{des}^3} \tag{C.2}$$

What can be seen from figure C.2 is that the types of wood with the least deflection are also some of the heaviest. It is therefor that carbon fiber reinforced plates are considered. When examining the weights of carbon reinforced wood it becomes clear that these are even heavier than hardwood counterparts for the same thickness. However the deflections are different. A carbon layer will create a sandwich structure with though plates on the outer ends. This leads to an even stiffer total material while keeping it relatively light

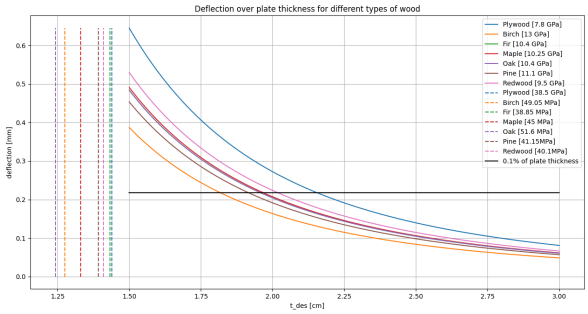

Figure C.1: Deflection for the different types of wood. The dotted lines give the minimal thickness to withstand the impact. The solid lines give the deflection. Every type of wood is strong enough for the impact if the design thickness is higher than 1.5 cm. The black solid line is a condition for the deflection as function of the plate width and height.

and inexpensive in comparison with pure carbon. It is assumed the wood used in between the carbon layers is the highly available plywood.

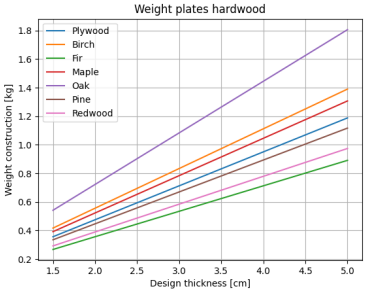

Figure C.2

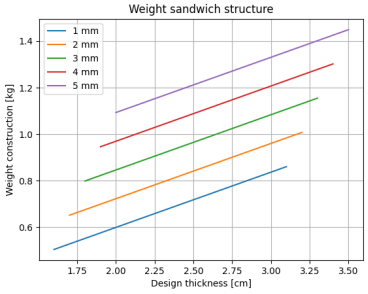

Figure C.3

In figure C.4, it can be seen that the carbon adds way more stiffness to the structure. However, 1 mm adds most of the stiffness which increases less significant after. By comparing C.1 and C.4 it can be concluded that while on the heavy side a thinner plywood plate reinforced with carbon fiber on both sides will lead to a stiff structure while keeping the weight to a minimum. For the experiment a plate is used of 18 mm with 1 mm carbon on both sides. This will result in a maximum deflection of 0.075 or 0.034% of the plates width of height.

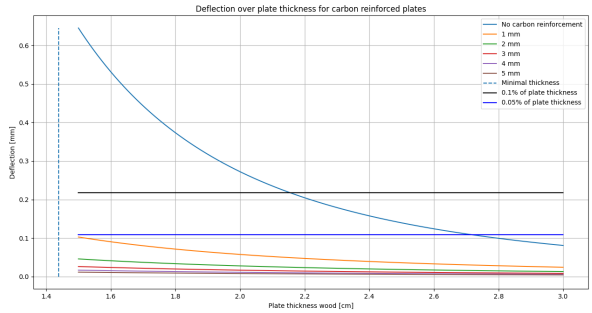

Figure C.4: Deflection of plywood reinforced with carbon. The dotted line is the minimal thickness for plywood to withstand the impact. The solid lines give the deflection for different thickness of carbon fiber layers. Even 1 mm adds significant stiffness for the plate. The black and blue line give the percentage of deflection over the width or height of the plate. For the experiment plywood of 18 mm is chosen with 1 mm carbon fiber.

D

Support Experiment

This appendix will support chapter 3 and in particular 3.6.

D.1 Pictures DAQ and Experiment

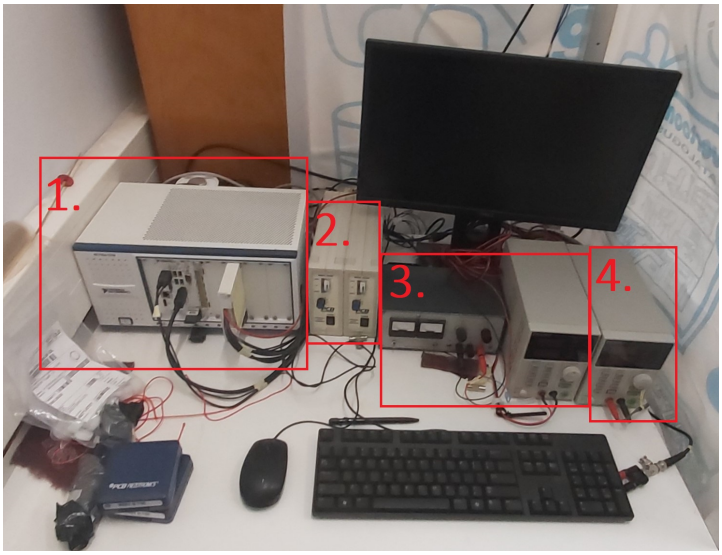

Figure D.1: Set up of the DAQ system with all the components: 1 PXI system. 2 Signal conditioner for the accelerometers and the pressure sensors. 3 Signal and power for the electromagnet connected to the PXI system. 4 Power for the flow meter.

D.2 Aerated Impact Flat Plate

When the flat plate hits the water when aeration is present the air bubbles can be identified to move towards the plate. In figure D.3 the moment before impact and just after impact can be seen. On the right side, just before impact the bubbles can be seen homogeneous divided over the volume. On the right side however the bubbles become fuzzy towards the plate and er more clear the further away. It is expected that this is the water air mixture which is compressed after impact.

Figure D.2: The set up of the experiment as shown in chapter 3. This is an enlarged picture of the experiment.

D.3 Data Experiment

In this appendix all data from the pressure sensors is given. The figures are ordered by shape and aeration. The firs figures are the flat plate followed by the wedge with a deadrise angle of 15° which is followed by the wedge with a deadrise angle of 30°. The aeration is ordered by ascending levels of air in the water. The figures used in the text. The figures used in the text are also given in this appendix for the sake of completeness. The reference back to the text is given in the caption off the figure.

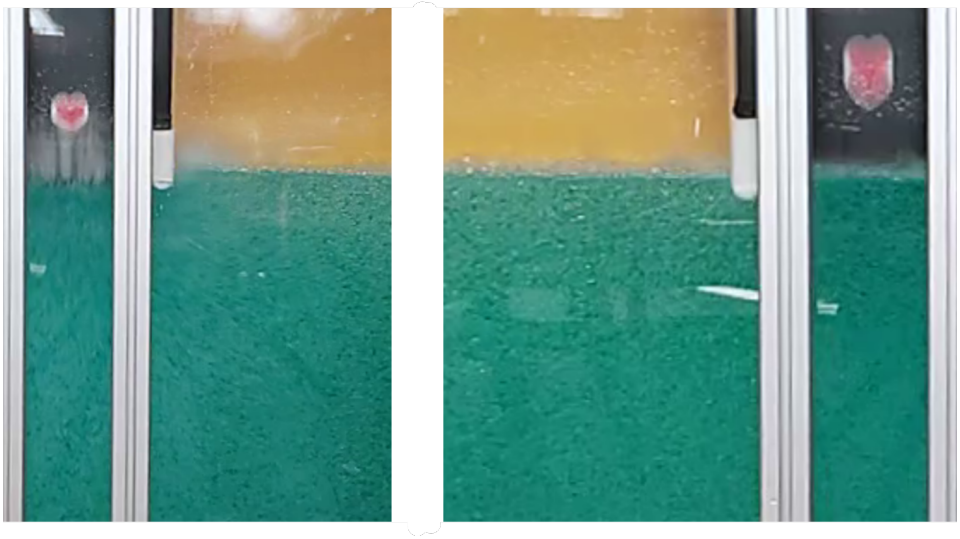

Figure D.3

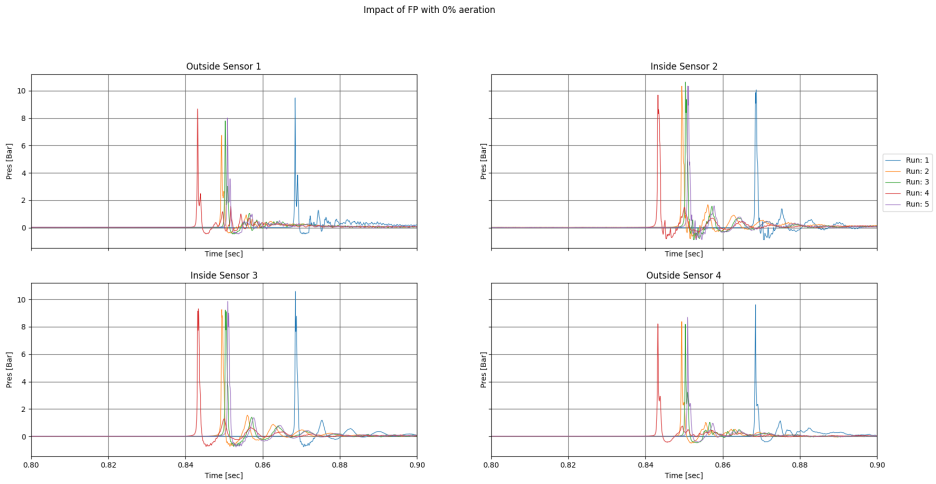

Figure D.4: Data for all sensors for non aerated impact of a flat plate (3.31)

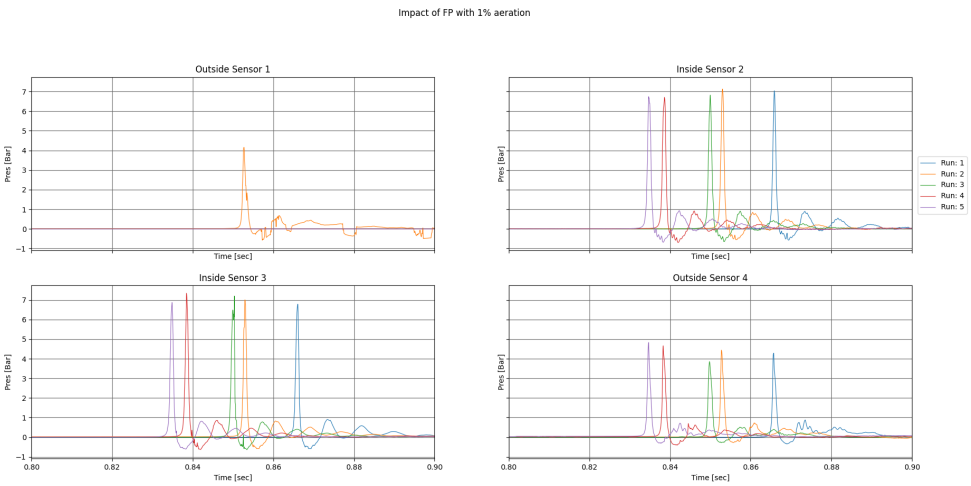

Figure D.5: Data for all sensors for aerated impact of 1% of a flat plate

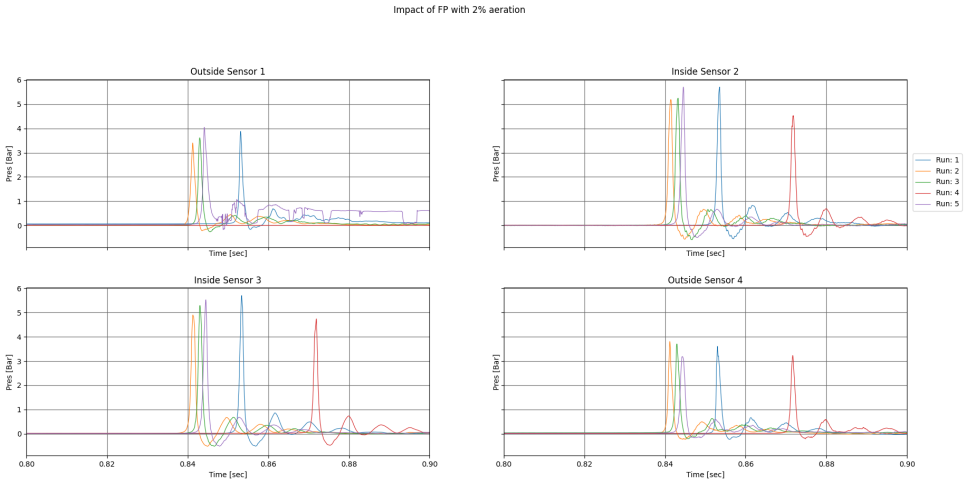

Figure D.6: Data for all sensors for aerated impact of 2% of a flat plate

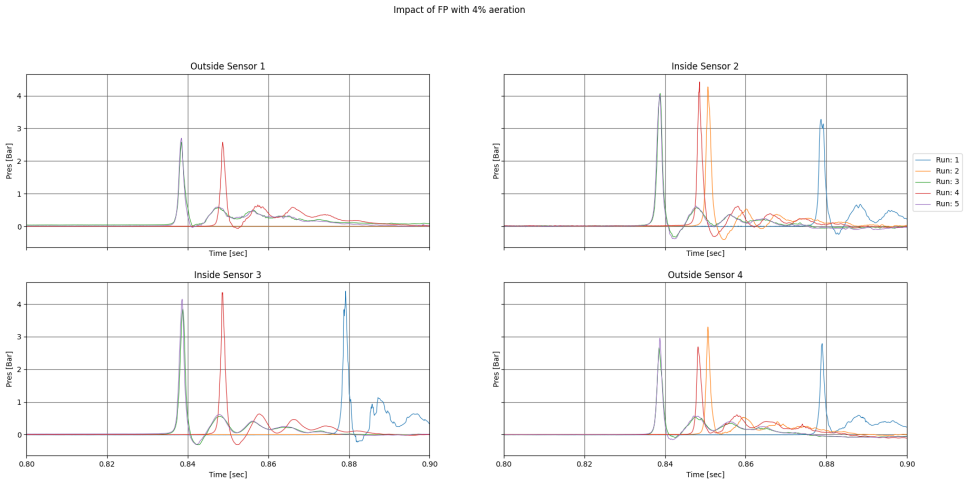

Figure D.7: Data for all sensors for aerated impact of 4% of a flat plate (3.52)

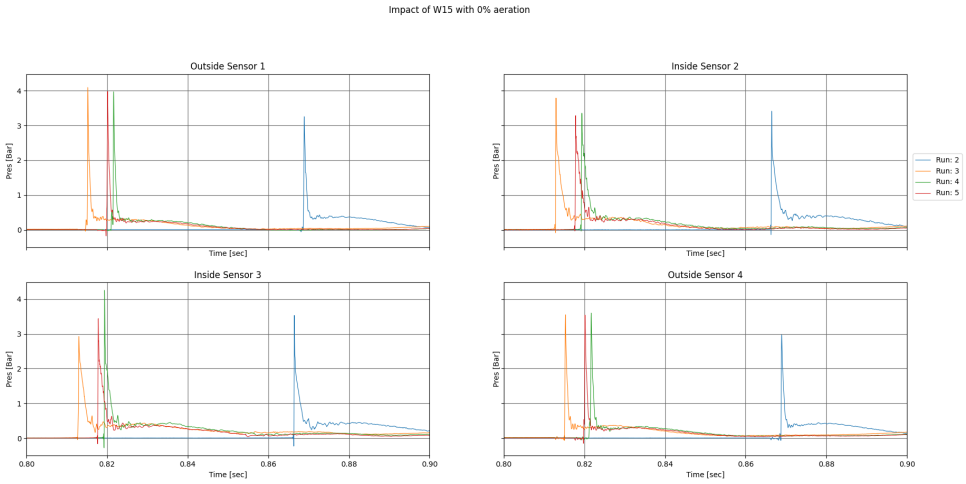

Figure D.8: Data for all sensors for non aerated impact of a wedge with a deadrise angle of 15°

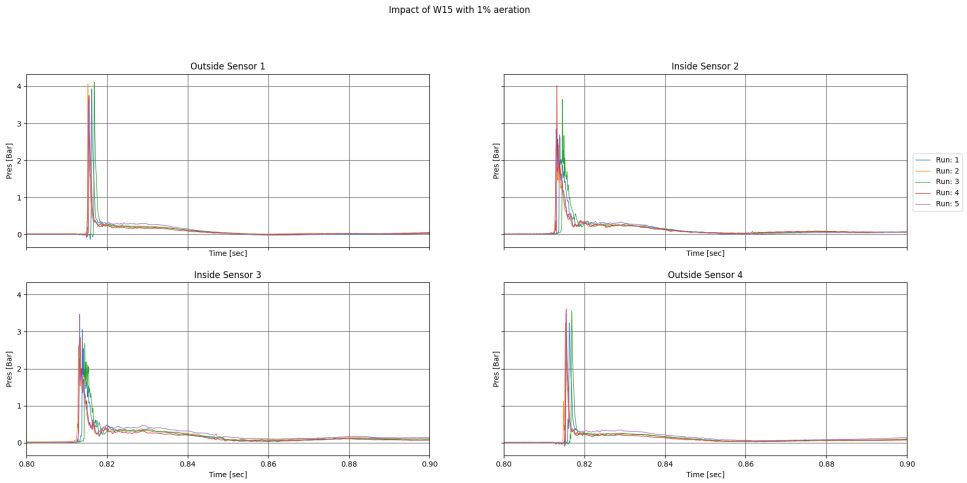

Figure D.9: Data for all sensors for aerated impact of 1% of a wedge with a deadrise angle of 15° (3.32)

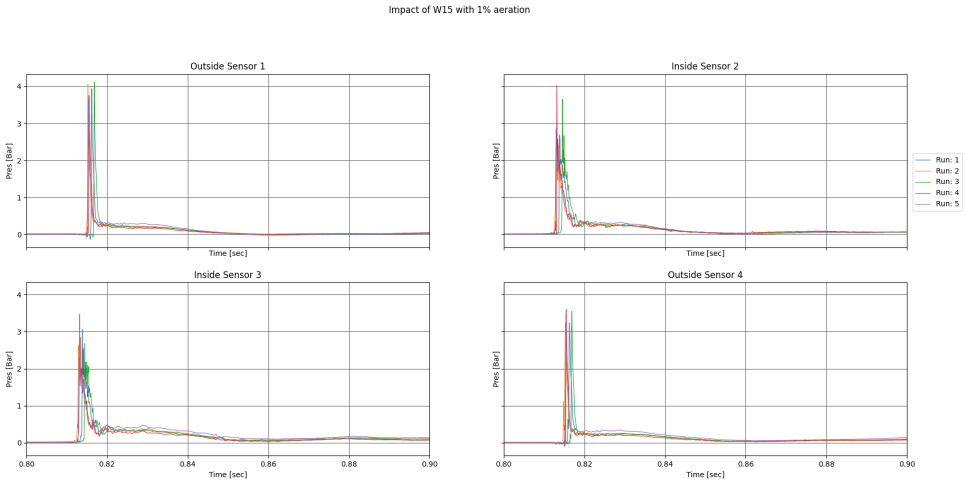

Figure D.10: Data for all sensors for aerated impact of 2% of a wedge with a deadrise angle of 15°

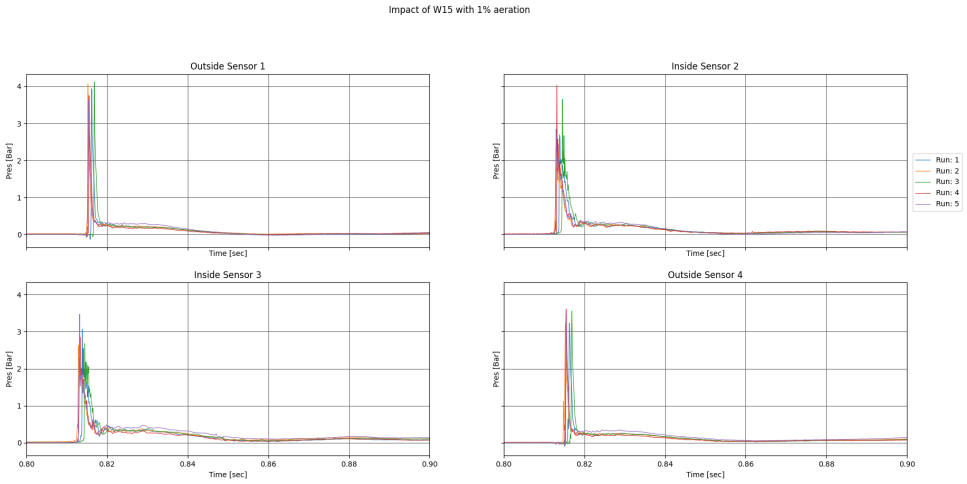

Figure D.11: Data for all sensors for aerated impact of 4% of a wedge with a deadrise angle of 15° (3.53)

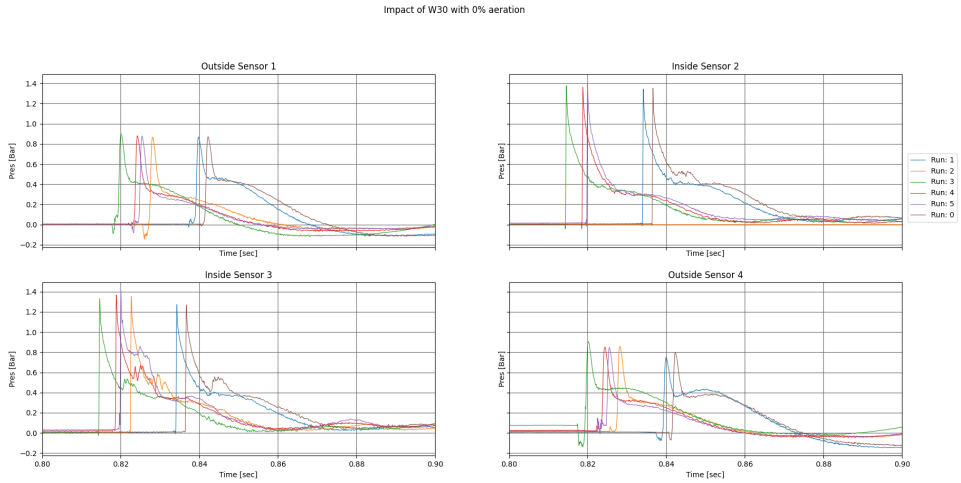

Figure D.12: Data for all sensors for non aerated impact of a wedge with a deadrise angle of 30° (3.33)

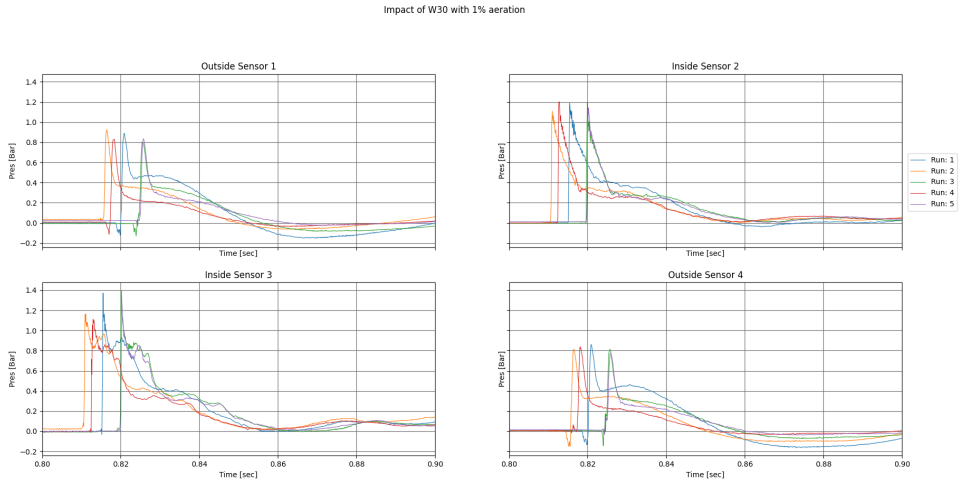

Figure D.13: Data for all sensors for aerated impact of 1% of a wedge with a deadrise angle of 30°

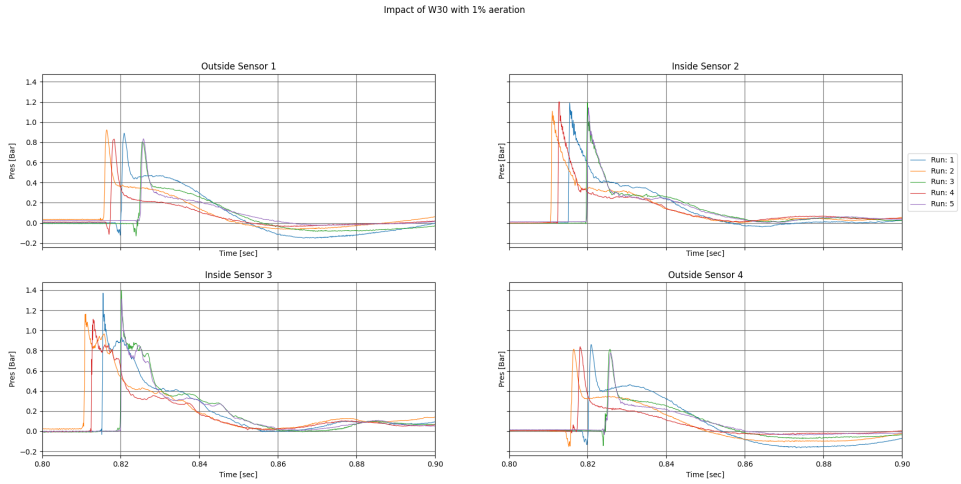

Figure D.14: Data for all sensors for aerated impact of 2% of a wedge with a deadrise angle of 30°

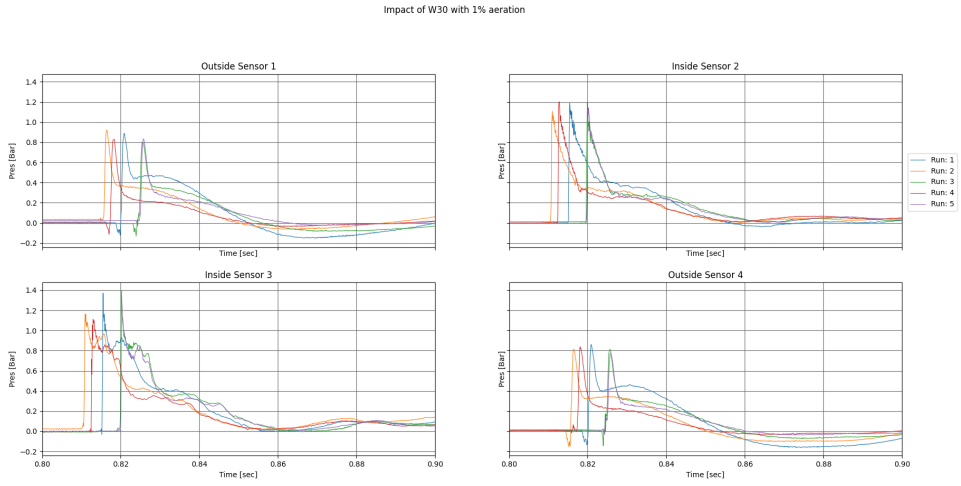

Figure D.15: Data for all sensors for aerated impact of 4% of a wedge with a deadrise angle of 30° (3.54)

Bibliography

[1] Omar S. Areu-Rangel, Jassiel V. Hernández-Fontes, Rodolfo Silva, Paulo T.T. Esperança, and Jaime Klapp. Green water loads using the wet dam-break method and SPH. *Ocean Engineering*, 219, 1 2021. doi: 10.1016/J.OCEANENG.2020.108392.

[2] Marco Barcellona, Maurizio Landrini, Marilena Greco, and O. M. Faltinsen. An Experimental Investigation on Bow Water Shipping. *Journal of Ship Research*, 47(04):327–346, 12 2003. ISSN 0022-4502. doi: 10.5957/JSR.2003.47.4.327.

[3] Josip Bašić, Nastia Degiuli, Šime Malenica, and Dario Ban. Lagrangian finite-difference method for predicting green water loadings. *Ocean Engineering*, 209:107533, 8 2020. ISSN 00298018. doi: 10.1016/j.oceaneng.2020.107533. URL https://linkinghub.elsevier.com/retrieve/pii/S0029801820305448.

[4] B. Buchner. The impact of green water on FPSO design. Technical report, 1995. URL https://repository.tudelft.nl/islandora/object/uuid%3Ac6803e78-4e52-480f-a8c9-ec72fe2da86a.

[5] B Buchner and Bas Buchner. ON THE IMPACT OF GREEN WATER LOADING ON SHIP AND OFFSHORE UNIT DESIGN ON THE IMPACT OF GREEN WATER LOADING ON SHIP AND OFFSHORE UNIT DESIGN. Technical report, TU Delft, 1995. URL https://repository.tudelft.nl/islandora/object/uuid%3A75e64fc8-02b9-4bcc-ac7c-45f6f3ce13e8.

[6] Bas Buchner. *Green Water on Ship-type Offshore Structures*. PhD thesis, Delft University of Technology, 2002. URL https://repository.tudelft.nl/islandora/object/uuid%3Ae383a7ef-43b5-4137-93d1-d5ab8fc75568.

[7] G. N. Bullock, A. R. Crawford, P. J. Hewson, M. J.A. Walkden, and P. A.D. Bird. The influence of air and scale on wave impact pressures. *Coastal Engineering*, 42(4):291–312, 4 2001. ISSN 03783839. doi: 10.1016/S0378-3839(00)00065-X. URL https://linkinghub.elsevier.com/retrieve/pii/S037838390000065X.

[8] Linfeng Chen, Yitao Wang, Xueliang Wang, and Xueshen Cao. 3D numerical simulations of greenwater impact on forward-speed wigley hull using open source codes. *Journal of Marine Science and Engineering*, 8(5), 5 2020. doi: 10.3390/JMSE8050327.

[9] CoastalWiki. Dam Break Force, Accessed in 2022. URL http://www.coastalwiki.org/wiki/Dam_break_flow.

[10] Electronics-tutorials. Butterworth Filter Design, Accessed in 2022. URL https://www.electronics-tutorials.ws/filter/filter_8.html.

[11] M. Elhimer, N. Jacques, A. El Malki Alaoui, and C. Gabillet. The influence of aeration and compressibility on slamming loads during cone water entry. *Journal of Fluids and Structures*, 70:24–46, 4 2017. doi: 10.1016/J.JFLUIDSTRUCTS.2016.12.012. URL http://dx.doi.org/10.1016/j.jfluidstructs.2016.12.012.

[12] ESA. Drop tower experiments, Accessed in 2022. URL https://www.esa.int/Science_Exploration/Human_and_Robotic_Exploration/Research/Drop_towers.

[13] Jassiel V.H. Fontes, Irving D. Hernández, Edgar Mendoza, Rodolfo Silva, Eliana Brandão da Silva, Matheus Rocha de Sousa, José Gonzaga, Raíssa S.F. Kamezaki, Lizeth Torres, and Paulo T.T. Esperança. On the evolution of different types of green water events. *Water (Switzerland)*, 13(9), 5 2021. doi: 10.3390/W13091148.

[14] M. Greco, O. M. Faltinsen, and M. Landrini. Shipping of water on a two-dimensional structure. *Journal of Fluid Mechanics*, 525:309–332, 2 2005. doi: 10.1017/S0022112004002691.

[15] M. GRECO, G. COLICCHIO, and O. M. FALTINSEN. Shipping of water on a two-dimensional structure. Part 2. *Journal of Fluid Mechanics*, 581:371–399, 6 2007. ISSN 0022-1120. doi: 10.1017/S002211200700568X. URL https://www.cambridge.org/core/product/identifier/S002211200700568X/type/journal_article.

[16] M. Greco, B. Bouscasse, and C. Lugni. 3-D seakeeping analysis with water on deck and slamming. Part 2: Experiments and physical investigation. *Journal of Fluids and Structures*, 33:148–179, 8 2012. doi: 10.1016/J.JFLUIDSTRUCTS.2012.05.009.

[17] Jassiel V. Hernández-Fontes, Marcelo A. Vitola, Monica C. Silva, Paulo De Tarso T. Esperança, and Sergio H. Sphaier. Use of wet DAM-break to study green water problem. In *Proceedings of the International Conference on Offshore Mechanics and Arctic Engineering - OMAE*, volume 7A-2017. American Society of Mechanical Engineers (ASME), 2017. ISBN 9780791857731. doi: 10.1115/OMAE2017-62113.

[18] Jassiel V. Hernández-Fontes, Marcelo A. Vitola, Monica C. Silva, Paulo de Tarso T. Esperança, and Sergio H. Sphaier. On the generation of isolated green water events using wet dam-break. *Journal of Offshore Mechanics and Arctic Engineering*, 140(5), 10 2018. doi: 10.1115/1.4040050.

[19] Jassiel V. Hernández-Fontes, Paulo T.T. Esperança, Rodolfo Silva, Edgar Mendoza, and Sergio H. Sphaier. Violent water-structure interaction: Overtopping features and vertical loads on a fixed structure due to broken incident flows. *Marine Structures*, 74:102816, 11 2020. ISSN 09518339. doi: 10.1016/j.marstruc.2020.102816. URL https://linkinghub.elsevier.com/retrieve/pii/S0951833920301106.

[20] Jassiel V. Hernández-Fontes, Edgar Mendoza, Irving D. Hernández, and Rodolfo Silva. A detailed description of flow-deck interaction in consecutive green water events. *Journal of Offshore Mechanics and Arctic Engineering*, 143(4), 8 2021. doi: 10.1115/1.4049121.

[21] F. J. Huera-Huarte, D. Jeon, and M. Gharib. Experimental investigation of water slamming loads on panels. *Ocean Engineering*, 38(11-12):1347–1355, 8 2011. ISSN 00298018. doi: 10.1016/J.OCEANENG.2011.06.004.

[22] Kouki Kawamura, Hirotada Hashimoto, Akihiko Matsuda, and Daisuke Terada. SPH simulation of ship behaviour in severe water-shipping situations. *Ocean Engineering*, 120:220–229, 7 2016. doi: 10.1016/J.OCEANENG.2016.04.026.

[23] Sang-Yeob Kim and Yonghwan Kim. *Comparison of Impact Pressure on 2D and 3D Tanks under Harmonic Excitation*. 2017. ISBN 9781880653975. URL www.isope.org.

[24] Z. H. Ma, D. M. Causon, L. Qian, C. G. Mingham, T. Mai, D. Greaves, and A. Raby. Pure and aerated water entry of a flat plate. *Physics of Fluids*, 28(1), 1 2016. doi: 10.1063/1.4940043.

[25] Peter Wellens Martin van der Eijk. Experimental and numerical comparison of 2D buoyant falling wedges. *Journal of Fluids and Structures*, 2022.

[26] Shafiul Mintu, David Molyneux, and Bruce Colbourne. Full-scale SPH simulations of ship-wave impact generated sea spray. *Ocean Engineering*, 241, 12 2021. ISSN 00298018. doi: 10.1016/J.OCEANENG.2021.110077.

[27] M. Nikfarjam, O.B. Yaakob, M.S. Seif, and J. Koto. Investigation of Wedge Water-Entry Under Symmetric Impact Loads by Experimental Tests. *Latin American Journal of Solids and Structures*, 2017(14):861–873, 2017. doi: 10.1590/1679-78253315. URL http://dx.doi.org/10.1590/1679-78253315.

[28] Shinzo Okada and Yoichi Sumi. On the water impact and elastic response of a flat plate at small impact angles. *Journal of Marine Science and Technology*, 5(1):31–39, 2000. ISSN 09484280. doi: 10.1007/S007730070019.

[29] Sung Hoon Park, Changhwan Park, Jin Yong Lee, and Byungchul Lee. A Simple Parameterization for the Rising Velocity of Bubbles in a Liquid Pool. *Nuclear Engineering and Technology*, 49(4):692–699, 6 2017. ISSN 2234358X. doi: 10.1016/J.NET.2016.12.006.

[30] Pentair. Pentair Aquatic Eco-Systems Sweetwater Air Diffusers, Accessed in 2022. URL https://pentairaes.com/sweetwater-air-diffusers.html.

[31] X. P. Pham and K. S. Varyani. Evaluation of green water loads on high-speed containership using CFD. *Ocean Engineering*, 32(5-6):571–585, 4 2005. doi: 10.1016/J.OCEANENG.2004.10.009.

[32] PCB Piezotronics. Dynamic pressure sensors for high frequency measurements, Accessed in 2022. URL https://www.pcb.com/contentstore/MktgContent/LinkedDocuments/Pressure/TM-PRS-113B-102B_lowres.pdf.

[33] Suresh Rajendran, Nuno Fonseca, and C. Guedes Soares. Prediction of extreme motions and vertical bending moments on a cruise ship and comparison with experimental data. *Ocean Engineering*, 127: 368–386, 11 2016. ISSN 0029-8018. doi: 10.1016/J.OCEANENG.2016.10.021.

[34] Reddit.com. Royal Navy Type 42 destroyer HMS Nottingham (D91) buries her bow., Accessed in 2022. URL https://www.reddit.com/r/HeavySeas/comments/6ek12j/royal_navy_type_42_destroyer_hms_nottingham_d91/l.

[35] Paola E Rodríguez-Ocampo, Jassiel V H Fontes, Michael Ring, Edgar Mendoza, and Rodolfo Silva. A CFD Numerical Study to Evaluate the Effect of Deck Roughness and Length on Shipping Water Loading. 2021. doi: 10.3390/w13152063. URL https://doi.org/10.3390/w13152063.

[36] R. Skalak and D. Feit. Impact on the surface of a compressible fluid. *Journal of Manufacturing Science and Engineering, Transactions of the ASME*, 88(3):325–331, 1966. ISSN 15288935. doi: 10.1115/1.3670955.

[37] The Engineering Toolbox. Impact Force, Accessed in 2022. URL https://www.engineeringtoolbox.com/impact-force-d_1780.html.

[38] B.J.H. Vendeloo. Development of an experimental setup for the validation of numerical 2D wedge water entry forces in aerated water. 2021.

[39] Warren C Young, Richard G Budynas, and Ali M Sadegh. *Roark ' s Formulas for Stress and Strain*. ISBN 9780071742481.